Complex behavior of colloidal suspensions undershear: dynamics investigation through light scatteringtechniques.

Francesca Ianni

THESIS OF JOINT RESEARCH DOCTORATE

between

UNIVERSITÀ "LA SAPIENZA" DI ROMA

and

UNIVERSITÉ PARIS VI

Subject

Materials Science

Presented by

Francesca Ianni

To obtain the degree of

Doctor Philosophiæ in Materials Science

Title

Complex behavior of colloidal suspensions under shear: dynamics investigation through light scattering techniques.

Discussed on the 16th March 2007
in front of the commission composed of:

Prof. **Giancarlo Ruocco** Thesis director
Dr. **Pascal Hébraud** Thesis director
Prof. **Umberto Marini Bettolo** Examiner
Prof. **Patrick Perrin** Examiner

Acknowledgements

First of all, I want to thank Giancarlo Ruocco and Francois Lequeux, who let me develop my work in a very pleasant and fruitful context. In particular, I thank Giancarlo for his availability in discussing and advising.

I am very grateful to Roberto Di Leonardo and Pascal Hebraud, who have followed and driven my work with great intelligence. The ideas of Roberto have often been fundamental to proceed in the work. The great availability and zeal of Pascal have really amazed me and have contributed to make me enthusiastic of my French stay.

I thank Gianni Bolle, Mario Pallagrossi and Md Islam Deen, who has provided technical assistance, for their great kindness. And now it's up to my room mates, whose gay and pleasant presence have accompanied me everyday during the writing of this thesis: Stefano, Neda, Simone, Silvia, Emanuele and Laura, who, in particular, has always answered patiently to my questions and demands.

Contents

Introduction

Colloidal systems are suspensions of nanoscopic particles in a liquid medium. They are widespread in everyday life and in many industrial domains, but the physical behavior of these materials is still poorly understood. When subject to a shear flow, such systems may exhibit a wide and complex phenomenology: appearance of a yield stress, decrease of the viscosity as the external drive is enhanced (shear thinning), growth of the viscosity (shear thickening) which may even lead to cessation of the flow (jamming transition) for strong external drives, formation of bands along the flow (shear banding). Though several experimental works have well characterized this complex rheology (*i.e.* flow behavior), a microscopic description of the observed behavior is still not exhaustive. One possible route to go further a phenomenological description is to recognize a strong similarity between the dynamics of concentrated colloidal suspensions and the dynamics of glassy systems. Glasses are liquids whose molecules are so tightly packed that the time relaxation to reach thermodynamic equilibrium becomes experimentally infinite, while, macroscopically, their viscosity diverges. Some of the tools which resulted successful for the investigation of glassy dynamics have thus been extended to account for the presence of driving forces. This idea, exploited for more than one decade, has highly contributed to a better understanding of the microscopic behavior of colloidal materials. At the same time, the topic of the glass transition is one of the more challenging in modern statistical mechanics, and the phase behavior and fluctuation dynamics in out of equilibrium systems is still an open issue. The virtuous relation among the physics of colloidal materials and the physics of glassy systems can thus be exploited the other way round: colloidal suspensions can be used as prototypic systems for testing experimentally the theories developed for glassy systems. A part of the work that we will present enhances this relation, by showing that the dynamical behavior of a colloidal suspension under shear can be interpreted

through the microscopic models describing glassy systems. The general aim of this experimental work is the investigation of the microscopic dynamics which underlies the complex rheological behavior exhibited by many colloidal systems under a steady external drive. In particular, we will focus on three different phenomenon: shear thinning and shear banding in a glassy system (a Laponite clay suspension), and shear thickening in a concentrated suspension of charged silica particles. In both cases, the samples used represent model systems for the observed phenomenology.

As suggested by many theoretical approaches to the study of glassy systems, a good variable capable of describing the dynamics of colloidal suspensions is the particle density time correlation function $F(t, t')$, which encodes information about the microscopic relaxation timescales in the material. Typically, a two step decay is observed in the correlation function of concentrated colloidal suspensions. A fast relaxation accounts for local rearrangements of the particles, while a slow decay represents a structural relaxation process. The timescale of these collective rearrangements represents the microscopic counterpart of the viscosity of the system and is found to be strongly influenced by a shear flow. In concentrated suspensions, the shear thickening regime is believed to be induced by the formation of macroscopic clusters of particles, which hinder the flow and may even lead to a jamming transition. An increase of the slow relaxation timescale is thus expected as the external drive is enhanced. A more complex behavior is observed in glassy colloids. These are out of equilibrium systems and their correlation function F explicitly depends on the age of the system since sample preparation, called waiting time t_w: $F = F(t_w, t_w + t)$. In particular, the slow relaxation time is found to increase with t_w when the system is at rest, thus driving to dynamical arrest. Such a behavior is called aging. When subject to shear flow, a new relevant timescale in the dynamics of the system is represented by the inverse shear rate $\dot{\gamma}^{-1}$ (the shear rate $\dot{\gamma}$ is the parameter used to quantify the external drive inducing the flow). The competition between the timescale introduced by the flow and the natural timescale of particle rearrangements may drive to a shear thinning behavior, with the slow relaxation time τ_s decreasing as the shear rate $\dot{\gamma}$ increases (shear rejuvenation). A power law behavior $\tau_s \sim \dot{\gamma}^{-m}$ with $m < 1$ is observed in various theoretical models for glassy systems. When low shear rates are applied to glassy suspensions, another interesting behavior is predicted by theoretical models: the system splits into two bands, one flowing as a solid body at a constant velocity and the other flowing at a finite local shear rate

(shear localization). The difference among the two bands is believed to be of dynamical nature, with an arrested phase in the solid band and a liquid phase is the other.

Light scattering techniques are a perfect tool to follow the dynamics of colloidal suspensions, as the scattered intensity signal gives direct information on the timescales characterizing the motion of the colloidal particles. In the single scattering regime, the drag motion of the particles under shear flow can be monitored through the interference of the scattered beam with a reference laser beam. Such a technique (heterodyne dynamic light scattering) allows direct access to the velocity profile of the system under shear and represents a local probe for the detection of shear bands. The scattered intensity correlation function in the single scattering regime (homodyne dynamic light scattering) is instead directly related to the particle density correlation function. In concentrated suspensions, where multiple scattering occurs, diffusive wave spectroscopy can be used instead of dynamic light scattering. However, in both techniques, a great limit to the investigation of the dynamics under shear is represented by decorrelating effects of geometrical nature on the scattered intensity, which prevents from accessing the slow relaxation time of the system. Actually, following the system dynamics under a steady external drive is prohibitive with any experimental technique, but information on these dynamics can be deduced by the measurements performed soon after shear cessation.

Despite the large amount of numerical and theoretical works investigating the influence of a steady shear flow on the slow dynamics of glassy colloids, an experimental microscopic counterpart is still relatively poor. No attempt has been made up to now to investigate shear influenced dynamics through a direct probe of the particle density correlation function. Using dynamic light scattering, the rejuvenating effect of a steady shear flow on the aging dynamics of a Laponite suspension is investigated through various protocols. A phenomenological model accounting for the competition of timescales between the inverse shear rate and the structural relaxation time is proposed to interpret the results. The same system is also investigated when low shear rates are applied. The shear localization phenomenon is observed, with an interesting phenomenology consisting in an oscillating velocity profile. In glassy suspensions, distinct dynamics among of the two bands forming under shear have never been observed experimentally and an attempt to detect such difference is made.

The last part of the experimental work is devoted to the study of the

jamming regime in a concentrated suspension. The scenario depicted by the experimental works proposed in the literature is still not exhaustive in describing the particle microstructure responsible for shear-thickening. In particular, investigation on the dynamics of the shear induced aggregates is still lacking. Through speckle visibility spectroscopy, a technique based on diffusive wave spectroscopy, we monitor the dynamics of the system during the flow and we follow the relaxation of the shear induced aggregates after shear cessation.

The thesis is divided into three parts:

1. The first, split into two chapters, introduces the scientific problem, describing the phenomenology and the theories reported in the literature. In particular, in the first chapter, the complex phenomenology observed in colloidal systems under a steady external drive is presented and the principal results obtained up to now at the experimental level are discussed. Particular attention is devoted to glassy systems. In the second chapter, some of the most interesting microscopic theories and phenomenological models developed for the microscopic description of these systems are reviewed. Most of them take inspiration from the models thought for glassy systems, which have been extended to account for the presence of a shear flow.

2. The second part, also divided into two chapters, presents the techniques and the materials used in the experiments. In the first chapter, the basic theories for dynamic light scattering and diffusive wave spectroscopy are briefly presented, with particular attention to the effect of a drift velocity in the scattering particles. The second chapter is dedicated to the description of the samples and the techniques used in the experiments.

3. In the last part, divided into three chapters, the experimental results are presented and discussed on the light of the theoretical models reported in the first part. In the first chapter, we report an experiment investigating, through dynamic light scattering, the influence of a steady shear flow on the dynamics of an aging Laponite suspension. In the second chapter, the shear localization phenomenon is studied in the same system through heterodyne and homodyne dynamic light scattering. Finally, in the third chapter, we report the experiment investigating,

through speckle visibility spectroscopy, the dynamics of shear induced heterogeneities in a shear jamming, concentrated silica suspension.

Part I

Rheology of colloidal systems

CHAPTER 1

Colloidal suspensions under shear: phenomenology and experimental facts

Suspensions of small solid particles in a liquid medium are usually called colloids, a term derived from the Greek work $\kappa o \lambda \lambda \alpha$ for "glue". The colloidal particles in suspension may have a dimension between 1 nm and 10 μm. Examples of colloidal suspensions are ubiquitous: blood, paint, ink and cement may represent a hint at their diversity and technological importance. Colloids include foodstuff, pharmaceutical products, cosmetics and are precursors of many manufactured goods, such as composites and ceramics. Stable suspensions of inorganic particles had been obtained by alchemists already in the seventeenth century. But it was only in the 1950s that suspensions of highly monodisperse polymeric particles first became available, encouraging the development of quantitative theories for the dynamics and flow properties of colloidal suspensions.

The static and dynamic properties of colloidal suspensions can be very diverse, reflecting different kind of interactions between the colloidal particles. For instance, spherical charged particles may form a crystalline structure at even low volume fractions giving rise to a colloidal crystal, while charged anisotropic particles at low concentrations or hard spheres at high concentra-

tions may form a rigid phase with a disordered structure, typical of a glass. Part of this thesis is devoted to the investigation of these amorphous colloidal systems. Some of their mechanical features can be better understood if they are considered as glasses. Glasses are liquids whose molecules are so tightly packed that they cannot relax to the thermodynamic equilibrium (*i.e.* the crystal phase) even over periods of months or years. They are characterized by an aging behavior consisting in a dynamics slowing down with the age of the system since its quench. Glassy colloids could represent ideal systems to understand fundamental aspects of glassy systems. Indeed, they may be tunable equivalents of atomic or molecular glasses which form in supercooled liquids, with controllable interactions. Moreover, the spatial and temporal scales are advantageously much larger than in atomic systems, allowing for easier experimental study.

Investigating the structure and dynamics of colloidal suspensions is thus interesting both for industrial application and for fundamental research. In particular, the flow behavior of such suspensions and the corresponding microscopic dynamics are not trivial: this thesis is devoted to the investigation of this aspect. Colloidal suspensions, like other condensed-phase materials such as foams, emulsions and polymer melts are neither simple liquids nor simple crystalline solids and do not fall into the classical scheme of phase classification: solid, liquid or gas. These "complex fluids" possess mechanical properties that are intermediate between ordinary liquids and ordinary solids, for this reason they are called viscoelastic. For instance, they may maintain their shape like a solid for a while and eventually flow like a liquid. An example from everyday life is the toothpaste, which flows out of the tube only when squeezed and stops flowing immediately after it has been applied to the brush and so doesn't sink into the bristles. In general, these complex fluids typically behave as solids at short times and as liquids at long times and the characteristic time required to pass to the "liquid-like" behavior may vary from fractions of a second to days or even years, depending on the fluid. Glassy colloids are among those complex fluids characterized by long structural relaxation timescales.

In this work, we are interested in the investigation of the dynamics underlying the complex flow behavior of colloidal suspensions. In this chapter, we will first introduce (section 1.1) the basic principles of rheology (which deals with the measurement and prediction of flow behavior). A hint to the phenomenology of glassy colloidal systems is reported in 1.2. In 1.3, we will then present the diverse behaviors encountered in colloidal suspensions un-

der shear, together with some experimental results obtained up to now, with particular attention to glassy colloidal systems.

1.1 Introduction to rheology

Rheology is the study of the deformation and flow of matter under the influence of an applied stress. The term was inspired by Heraclitus's famous expression "panta rei" (everything flows). In practice, rheology extends the study of elasticity and Newtonian fluid mechanics to materials whose mechanical behavior is intermediate between ordinary liquids and ordinary solids. The basic tool of this subject is the rheometer, a device for applying a controlled stress to a sample and measuring its deformation, or viceversa. Two different types of experiment may be performed with a rheometer: steady shearing experiments or oscillatory shearing experiments. The former is the type of experiment we will focus on in this work and will be explained in this section. The latter consists in imposing a small amplitude oscillatory shearing at a certain frequency ω, that does not significantly deform the fluid microstructure and allow to explore the rates of structural rearrangement. Two quantities capable of describing the "solid-like" or "liquid-like" behavior of the fluid can be measured through an oscillatory shearing experiment: the storage modulus $G'(\omega)$, representing storage of elastic energy by the fluid and the loss modulus $G''(\omega)$, representing the viscous dissipation of this energy. Oscillatory shearing experiments are beyond the scope of this work, thus we address the reader to Ref. [1] for a formal definition of these quantities.

In the following, we will first define the variables used in rheology (1.1.1). The flow behaviors that are typically observed in colloidal systems are introduced in 1.1.2, while the solid-like behavior characterizing these systems is presented in 1.1.3.

1.1.1 Rheometer geometry and rheological variables

We now introduce the basic tools used to describe a system under flow, focusing in particular on steady shearing experiments. In general, there are many different geometries for common flow cells used in rheometers. An example is the cone-plate cell, where a rotating cone contacts a stationary plate at its apex with a small opening angle. Another is the Couette cell, consisting in two concentric cylinders, with the internal one rotating, which

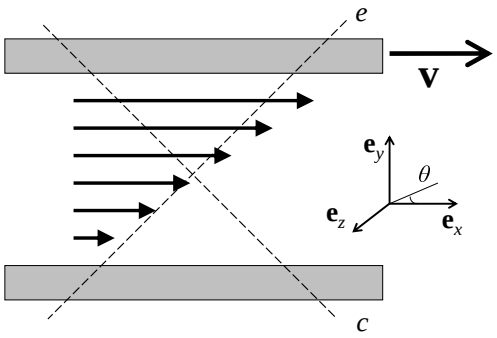

Figure 1.1: *Simple shear geometry as in a plane Couette flow. The upper plate slides at velocity* $\boldsymbol{v}$*, while the bottom one is fixed. The arrows represent the flux lines, while the directions* c *and* e *correspond, respectively, to the compressional axis* ($\theta = 3/4\pi$) *and the extensional axis* ($\theta = 1/2\pi$).

induces a "circular Couette flow". Other classical geometries are also sliding plates generating a "plane Couette flow", or parallel disks inducing torsional flow. Usually, the cartesian coordinates in a simple flow geometry are chosen in order to orientate the x axis along the flow direction and the y axis along the velocity gradient direction (Fig. 1.1).

The deformation rate of a fluid is defined by the velocity gradient tensor field $\boldsymbol{\nabla v}(\boldsymbol{r}, t)$, which describes the steepness of the velocity variation as one moves from point to point in any direction at time t ($\boldsymbol{r}$ is the position vector relatively to an arbitrary origin). If $\boldsymbol{v} = (v_x, v_y, v_z) \equiv \boldsymbol{v}(\boldsymbol{r}, t)$ is the velocity vector, $\boldsymbol{\nabla v}$ will be a matrix of dimensions 3×3. In a plane Couette geometry (Fig. 1.1), there is only one non zero component of the velocity, namely v_x and it varies only in the y direction, so that the velocity gradient tensor can be reconstructed from the scalar $\dot{\gamma} = \partial v_x / \partial y$, which is called shear rate. Also for other shearing flows generated by the geometries usually chosen in a rheological experiment, like the ones named above, there is for each fluid element a frame in which the velocity gradient tensor has only one nonzero element. This element is the so called shear rate and represents the derivative of the velocity along the flow direction with respect to the coordinate along the direction where the flow velocity varies, which is contained in the plane orthogonal to the flow direction. In steady shearing experiments, in each geometry the shear rate imposed on the fluid depends on a driving velocity and on the dimensions of the geometry. For the sliding plate device, the

shear rate is simply the velocity V of the moving plate (the other plate being held stationary), divided by the gap H between the two plates: $\dot{\gamma} = V/H$. In the cone and plate geometry, the shear rate is independent on the radial distance from the rotating axis (differently to the parallel disks geometry): $\dot{\gamma} = \Omega/\tan\alpha$, where Ω is the steady angular speed of the rotating cone and α is the opening angle between the plate and the cone.

Let's now define the stress tensor field $\boldsymbol{\sigma}(\boldsymbol{r}, t)$ (in the following, we will drop the dependence on $\boldsymbol{r}$ and t to simplify the formalism). If dS_i is a vectorial area element normal to the vector n_i and dF_i is the force acting on this surface element, then we have

$$dF_i = \sigma_{ij} dS_j$$

which defines the stress tensor σ_{ij}. A pure hydrostatic pressure corresponds to a diagonal stress tensor $\sigma_{ij} = -p\delta_{ij}$ (where δ_{ij} is the Kronecker symbol). Two particular combinations of the diagonal elements, which are independent on p, are defined as the first and second stress differences:

$$N_1 = \sigma_{xx} - \sigma_{yy} \quad N_2 = \sigma_{yy} - \sigma_{zz}$$

As may be shown from the equilibrium of moments acting on an infinitely small cubic volume, whatever the nature of the flow, the stress tensor is a symmetric tensor. In a shearing flow of an incompressible isotropic liquid, it contains at least two nonzero components, $\sigma_{xy} = \sigma_{yx}$, as well as an isotropic pressure term. In a simple liquid, these are the only non-zero components and the normal stress differences are null. However, a complex fluid in general has other nonzero components of the stress tensor, namely the normal stresses σ_{xx}, σ_{yy} and σ_{zz}. Since the stress tensor is only determined to within the additive isotropic tensor of the hydrostatic pressure, only the normal stress differences can be measured. The cone and plate geometry and the parallel disks geometry allow such measurement: for positive N_1 ($\sigma_{xx} > \sigma_{yy}$), the plates tend to be pushed apart; on the contrary, for negative N_1 ($\sigma_{xx} < \sigma_{yy}$), they tend to be pulled together.

In a plane Couette geometry, as the one depicted in Fig. 1.1, the only off-diagonal nonzero elements of the stress tensor are $\sigma_{xy} = \sigma_{yx}$ (the pressure term $-p\delta_{ij} = 0$), which we will call shear stress σ. In such geometry, the motion of a fluid of mass density ρ is described by the Navier-Stokes relation:

$$\rho \partial v(y,t)/\partial t = \partial \sigma(y,t)/\partial y$$

In a steady shearing experiment, the flow in such geometry is thus characterized by a local shear stress σ that is constant across the gap. Instead, for a laminar flow in a circular Couette geometry, the shear stress scales as r^{-2}, where r is the radial distance from the rotational axis of the cylinders. If C is the torque applied to the fluid and h is the fluid height, the shear stress results indeed as $\sigma(r) = C/(2\pi h r^2)$. Also the velocity gradient tensor reduces to a scalar in these simple geometries. The shear viscosity for steady shearing experiments in simple geometries can be defined by the constitutive relation:

$$\sigma = \eta\dot{\gamma}$$

and represents the resistance opposed by the system to the flow. The curve describing the shear stress behavior as a function of the shear rate applied to the fluid is the so called flow curve $\sigma(\dot{\gamma})$.

1.1.2 Flow behavior

The flow curve characterizes the mechanical properties of fluids under an external drive. Here, some of the complex flow behavior typical of colloidal suspensions will be presented. In simple liquids, also called Newtonian liquids, the viscosity is constant by varying the shear rate, thus the shear stress increases linearly with shear rate (linear rheology). On the contrary, complex fluids are characterized by a viscosity depending on the shear rate: $\eta = \eta(\dot{\gamma})$ (non-linear rheology). In solid-like behaving fluids, the shear stress is independent on shear rate when the steady state is reached, the shear viscosity then scales as $\eta(\dot{\gamma}) \sim \dot{\gamma}^{-1}$. The flow thus induces a fluidization effect in the system, consisting in a shear viscosity that decreases with increasing shear rate: this behavior is referred to as shear thinning. Real complex fluids often show an intermediate behavior between the solid-like and liquid-like prototypes. Therefore, a shear thinning behavior characterized by the power law $\eta(\dot{\gamma}) \sim \dot{\gamma}^{-m}$, where $m < 1$, is usually observed. The opposite behavior, with a viscosity increasing with the shear rate or with the shear stress, can also be observed at high stress and is called shear thickening.

The viscosity value for $\dot{\gamma} \to 0^+$ (*i.e.* $\lim_{\dot{\gamma}\to 0^+} \sigma/\dot{\gamma}$) is called the zero shear viscosity η_0. For some fluids, η_0 is not defined, as the flow curve exhibits a non zero stress value when $\dot{\gamma} \to 0^+$. This stress value is called yield stress σ_y. At small shear stresses, the system thus only deforms elastically, while when σ_y is reached, it starts flowing. If yielding corresponds to the onset of

a shear thinning regime, the flow curve can usually be fitted by the so called Herschel-Bulkley relation $\sigma(\dot{\gamma}) - \sigma_y \sim \dot{\gamma}^p$, where $0 < p < 1$. When $\sigma_y = 0$, one obtains a so called power-law fluid (with $p = 1 - m$).

In the above description of the flow, we assumed that the shear rate is constant across the gap of the cell. This is not always valid. An interesting phenomenon which may show in some complex fluids at low applied shear rates is shear banding, consisting in a flow subdivided into different bands, parallel to the flow direction, characterized by different local shear rates: $\dot{\gamma} = \dot{\gamma}(y)$ (in the coordinates system sketched in Fig.1.1). Though it is not directly observable through mechanical measurements, the shear banding phenomenon exhibits when the flow curve shows an instable region represented by a decreasing branch.

Finally, we want to hint at the wall slip problem, which may emerge in experiments on complex fluids under flow. In a rheometer cell, the fluid is supposed to adheres against the solid boundaries. For molecular liquids like water, wall slip is usually negligible, while a complex fluid with a solid-like behavior is expected to slip on the bounding surface of the cell, as a solid body would do. Glassy colloidal suspensions may behave as elastic materials and wall slip may be induced by the formation of lubricating layers of pure solvent next to the bounding surface of the rheometer cell. Slip may represent a problem for accessing to the shear rate value, which is reduced by this effect. It can be counteracted by using roughened rheometer surfaces, but when it still persists, measuring the local velocity profile at the boundaries is necessary [1].

1.1.3 Colloidal systems as soft solids

A parameter characterizing the "solid-like" behavior of a complex fluid is the shear modulus G, which measures the free energy cost for shearing an elementary volume [49]. Actually, this variable can be measured through oscillating shear experiments, which are not performed in our work. However, introducing this variable is worthy for a better comprehension of complex fluids and will be useful when presenting some of the theoretical models developed for these systems (2). Let's consider a cube of material of size L subject to a small shear strain $\gamma = l/L$, where l is the displacement. This will cause a shear stress σ and the shear modulus G is defined by the relation $\sigma = G\gamma$. A compressive distortion, creating an excess pressure Δp at the same strain, induces instead a compression modulus K, defined by the

relation $\Delta p \simeq K\gamma$. The two quantities G and K are similar as shear and compression both change bond lengths by similar amounts. Most familiar solids such as metals have $G \simeq K \simeq 10^{11}$ Pa, so stresses beyond the elastic limit can't be attained under laboratory conditions.

In rheology, the solid-like behavior of a fluid is thus investigated through the relation $\sigma = G\gamma$, that is accessible in oscillating shear experiments. The liquid-like behavior is instead exemplified by the relation $\sigma = \eta\dot{\gamma}$, accessible through steady shear experiments, where the shear rate $\dot{\gamma}$ is the temporal derivative of the strain γ. A handy, though very crude rule links the zero shear viscosity η_0 to the shear modulus and the characteristic relaxation time of the system dynamics τ:

$$\eta_0 \sim G\tau \tag{1.1}$$

This formula traces back to Maxwell, who argued that a viscous fluid with viscosity η_0 can be thought as a relaxing solid with modulus G that relaxes with a unique timescale τ. A Newtonian fluid is recovered by taking $G \to \infty$ and $\tau \to 0$ at fixed η.

The high sensitivity of colloidal suspensions to a shear flow field is easily demonstrated by the magnitude of the shear modulus G of a colloidal crystal. The dimension of the shear modulus is energy per volume. With a simple dimensional argument, considering that the interaction energy scale in a colloidal system is k_BT and the length scale is the typical interparticle spacing a, the value of G can be evaluated as $G \sim k_BT/a^3$. In colloidal systems, as in many complex fluids where the particle volume is much larger than in molecular solids, one has $G \ll K$ and for this reason they are called "soft solids". Values of G of order $1 \div 100$ Pa are typical of soft materials, thus stresses well beyond the elastic limit can be attained experimentally. Since the solvent has no shear modulus, the system static resistance to shear originates from the mesoscopic degrees of freedom associated with the colloidal particle configurations. Instead, the compression modulus is still of order 10^{10} Pa as a colloidal suspension is mostly composed of the solvent, and resists compression similarly to a liquid. On the other hand, if one compresses osmotically a soft material (placing it within a semipermeable membrane through which only the solvent can pass and squeezing it), a much lower compression modulus results, typically similar in magnitude to G.

The origin of the low shear modulus is thus a matter of length scales, as is due to the presence of large objects. The distinction between hard and soft materials is also a matter of timescales. A solvent like water, for

instance, actually resists shear flow, but its stress response to a sudden strain relaxes on a timescale too fast to be measured with a common rheometer. On the contrary, having a stress relaxation time on laboratory scales, many soft materials can exhibit solid-like behavior at short times and then liquid-like behavior at longer times in the same experiment.

1.2 Phenomenology of glassy colloidal suspensions

By investigating a glassy colloidal system through a microscope, it is evident that particles can move only by cooperating with each other: if a particle slightly moves, then a neighbor particle may move into the place left free by the first and so may do a third particle. We can suppose that, the higher the particle volume fraction in the system, the more the particles have to cooperate to move and the slower will be their dynamics. At a critical volume fraction, when all the particles have to cooperate in order to move and the timescale of this cooperative motion diverges, the system reaches gelation (*i.e.* the glassy phase). Crowding of the constituent particles traps themselves kinetically, precluding further exploration of the phase space. In this sense, there are two extreme pictures that schematically characterize concentrated colloidal systems in the glassy phase, corresponding to very different underlying interactions. The first image consists in colloidal particles rigidly bound, that diffuse in solution and form fractal aggregates. If the concentration is large enough, these aggregates diffuse and aggregate further on and eventually form a network made of rigidly interconnected aggregates. Colloidal systems with such a structure, which may be reached even at weak volume fractions, are called gels. The second picture is that of particles that repel each other and, at high concentrations, are pushed into one another. Due to its energy, the system thus gets trapped in a metastable state of disorderly crowded particles. This is what is usually called a soft glass, because of its low shear modulus. We are interested in the microscopic dynamics emerging during the glassy phase and in the effects of a shear flow on these dynamics.

The dynamics of glassy systems is usually described by the autocorrelation function of a relevant variable, like density fluctuations $\delta\rho(\boldsymbol{q}, t)$ ($\boldsymbol{q}$ is the

wave vector):

$$F(\boldsymbol{q}, t_0, t) = \langle \delta\rho(\boldsymbol{q}, t_0)\delta\rho(-\boldsymbol{q}, t_0 + t)\rangle / \langle |\delta\rho(\boldsymbol{q})^2| \rangle \tag{1.2}$$

When the system is stationary, the correlator doesn't depend on time t_0. In general, for a fixed time t_0, the correlator typically exhibits two dynamical timescales: a fast decay of F results from the vibrational degrees of freedom characterizing the oscillation of the particles around their equilibrium position, while a slow decay results from the structural rearrangement of the system through particle diffusion. While the fast relaxation usually doesn't depend strongly on the volume fraction, the slow relaxation drastically slows down as soon as the glassy phase is approached. Moreover, after a quench in the glassy phase, an aging behavior is observed: the structural relaxation slows down with the time t_w elapsed since the quench and the system enters a non-ergodic state. In colloidal glassy systems, a quench into the glassy phase can be achieved by preparing the sample at a volume fraction above the critical one. In supercooled liquids instead, the quench consists in cooling the system below the liquid-glass transition temperature. In the aging regime, the system is out of equilibrium and the correlator explicitly depends on the waiting time t_w: $F = F(\boldsymbol{q}; t_w, t)$.

When such a system is put under shear, the thickening effect due to aging may be contrasted by a thinning effect induced by the flow. As a result, a shear thinning behavior may emerge in the structural relaxation time $\tau \propto \dot{\gamma}^{-m}$ with $m \leq 1$ (using the rough Maxwell relaxation 1.1 for the viscosity, the macroscopic counterpart for this behavior may result). This situation can therefore be used to probe the glassy phase, with the convenience of having the system in a stationary state and the shear rate $\dot{\gamma}$ rather than the waiting time t_w as a control parameter. Experimentally, the m exponent is system dependent, so there is no reason to expect an universal value for it.

The sudden arrest of the colloidal system dynamics as the density is increased and the fluidizing effect of an external drive can be classified in a more general phenomenological scheme. It is the jamming transition picture, accounting for a wide range of fluid-solid transitions and unifying apparently diverse behaviors in very different systems, including not only supercooled liquids and colloidal systems, but ranging from granular media to foams. The state of structural arrest is identified as the jamming phase. In order to unify the description of all routes to jamming, Liu and Nagel [25] use, as intrinsic parameter of the system, the density ρ. The jamming phase can be overcome

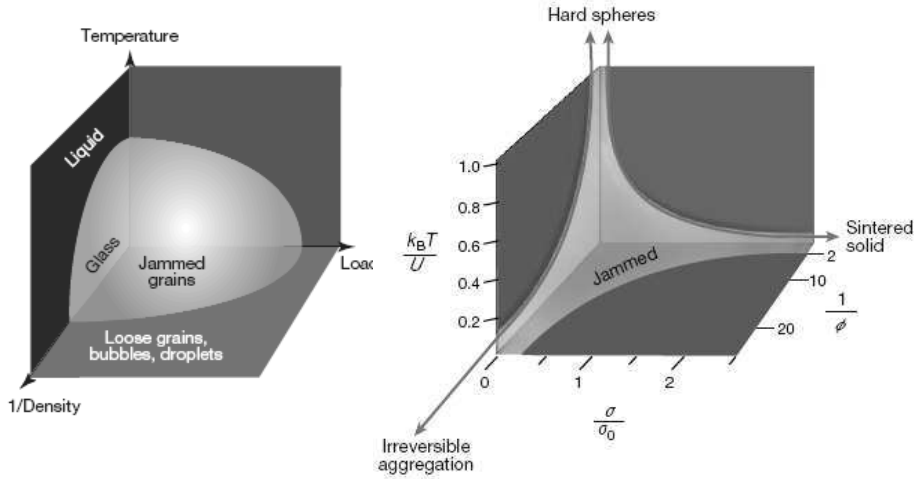

Figure 1.2: *Phase diagram for the jamming transition prosed by Liu and Nagel (left panel) and by Trappe et al. for weakly attractive colloids (right panel). The divergences in the second diagram correspond to irreversible aggregation, where the inverse critical volume fraction at which jamming occurs, Φ_c^{-1}, is large; to the limit of hard spheres, where T/U is large; and to high volume fractions of strongly attracting particles that form, for example, sintered solids, where the yield stress σ_y is large. The figures have been taken from Ref. [26].*

and the system fluidized by thermalization, through temperature or vibration, or by a unidirectional stress or load that exceeds the yield stress of the material σ_y. Thus, Liu and Nagel propose ρ^{-1}, temperature T and stress σ as the axes of a three dimensional jamming phase diagram (Fig. 4.8, left panel). In this context, the experimental work of Trappe et al. [26] on the fluid-solid transition of weakly attractive colloidal particles may be interesting. Stabilization against irreversible aggregation results in these systems in an attractive pair potential, like for sterically protected colloids. Like other colloids, they undergo gelation with increasing concentration and decreasing thermalization or stress. In colloidal systems, the degree of thermalization is primarily controlled by the interparticle energy U, which sets the scale of temperature. Besides, for weakly attractive colloidal system, the scale of the stress is set by $\sigma_0 = k_BT/a^3$, where a is the radius of the particles. Therefore, the axis of the phase diagram become the inverse volume fraction Φ^{-1}, k_BT/U and σ/σ_0. The schematic phase diagram that they obtain confirms the applicability of the jamming concept to the behavior of colloidal

suspensions. However, the shape of the experimental phase diagram differs significantly from that originally proposed by Liu and Nagel, having everywhere the opposite curvature and diverging at each corner. These divergences reflect the particular details of attractive colloidal particles.

1.3 Complex flow and experimental evidences

Due to the advantageous length scales and timescales, the effect of shear flow can be controlled and precisely measured in colloidal suspensions using scattering or direct imaging methods. The phenomenology of colloids under shear comprehends very diverse complex behaviors, which we will introduce in the following subsections together with some of the experimental results obtained up to now.

1.3.1 Shear thinning

Usually, at low shear rates, colloidal suspensions show a Newtonian behavior, resulting in a plateau in the flow curve at the value of the zero shear viscosity η_0. This regime is followed by a shear thinning regime and at very high shear rates a shear thickening regime may be observed. An example of such a behavior is shown in Fig. 1.3 for a charged suspension at different concentrations. In hard spheres, charged spherical spheres or anisotropic colloids, shear thinning behavior has been explained as due to an ordered microstructure induced by the flow. This enhances the sliding between layers perpendicular to the velocity gradient direction (see section 2.5.1). In disordered colloidal suspensions, the origin of shear thinning cannot be due to a coupling between the flow and the microstructure (see section 2.2), but has to be found in the interaction between the slow dynamics and the shear flow. Some of the experiments performed to investigate this microscopic mechanism are presented in the following section.

Experiments on shear thinning glassy colloids

For glassy colloids, the experimental investigation of the shear-influenced slow dynamics at the microscopic level is still relatively poor. Typically, in the experiments performed up to now, colloidal suspensions are prepared at a volume fraction high enough to be in the glassy phase, where an aging behavior is observed. In some experiments, the waiting time t_w is set to

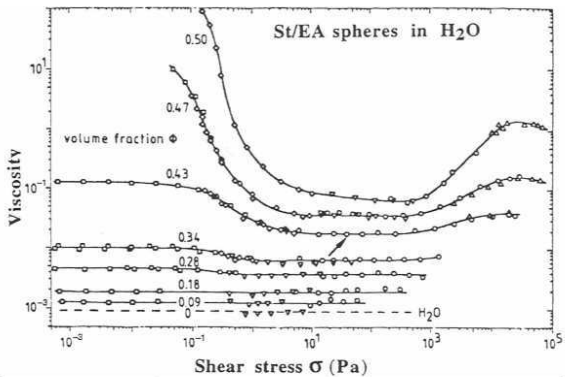

Figure 1.3: *Viscosity versus shear stress for aqueous suspension of charged polysterene-ethylacrylate copolymer spheres of diameter $d = 250$ nm at various volume fractions Φ. Figure from [2]*

zero soon after sample preparation. In other experiments, the quench into the glassy phase is obtained by applying a high shear, which have a strong rejuvenation effect: the counting of t_w starts soon after shear cessation. At rest, the evolution of slow dynamics since the quench are usually monitored through light scattering techniques. In particular, the scattered intensity autocorrelation function is calculated and the slow time relaxation of the correlation function is linked to the structural relaxation time τ of the system. Therefore, the scaling between τ and t_w is measured. The effect of shear flow on this aging dynamics has been investigated both in oscillatory and steady shear. For reasons that we will explain in 3.1.2, the measurement of the slow relaxation timescale is not possible during steady shear, as under the effect of the flow the intensity correlation function would decay at shorter times. Therefore, the procedure followed to investigate the system dynamics consists in stopping the flow for a short time to allow the measurement and turning it on soon after. Diffusing Wave Spectroscopy (DWS) experiments performed by Bonn and coworkers following this procedure have shown the rejuvenating effect of shear on an aging sample [3]. The system investigated is a Laponite suspension, a charged discoidal colloid that we will describe in 4.1.1 and will also be used in our experiments. In Bonn's experiment, the sample is left aging at rest after preparation. After a fixed time period, a steady shear is started and the correlation function is measured. Repeating the procedure for various shear rate values, the slow relaxation time of the

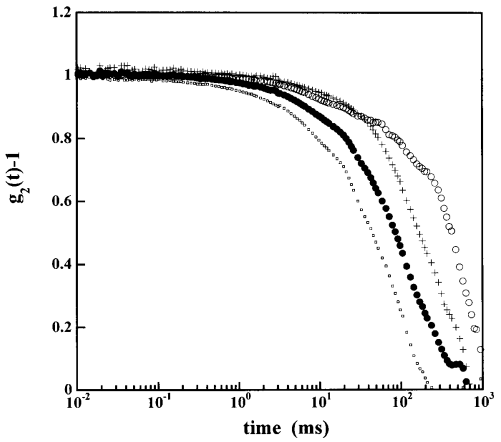

Figure 1.4: *Correlation functions measured by Bonn and coworkers using DWS for different shear rates. The curve to the right is the reference without shear and after 1 h of aging. After that, from right to left: 0.25 s^{-1}, 2.5 s^{-1} and 25 s^{-1}. Figure from Ref. [3].*

correlation function is observed to decrease with increasing shear rate (Fig. 1.4). However, a quantitative analysis of this dependence is missing in this work.

Under oscillatory shear, Light Scattering Echo (LSE) technique allows to investigate the dynamics during the shear, with no need to stop the flow. LSE [4, 97] and also DWS experiments [6, 7] have been performed on various glassy colloids, ranging from hard spheres to anisotropic charged particles, under oscillatory strain. Evidences for a shear dependent structural relaxation time and for rejuvenation of aged samples have been obtained. In particular, the DWS experiment realized by Viasnoff and Lequeux [6] on a glassy sample of charged spherical colloids is interesting. The system is quenched through the application of an oscillatory strain of high amplitude. In the spontaneous slow relaxation process that follows, τ scales linearly with t_w. After the high shear quench, various straining are applied and the following dynamics is monitored. While shear of high amplitude rejuvenates old samples by accelerating their dynamics, moderate shear amplifies aging: a phenomenon that the authors call overaging. In an experiment performed by Kaloun and coworkers [97], a similar protocol of shear is applied to aged samples of charged discoidal colloids. Again, a linear dependence between τ and t_w

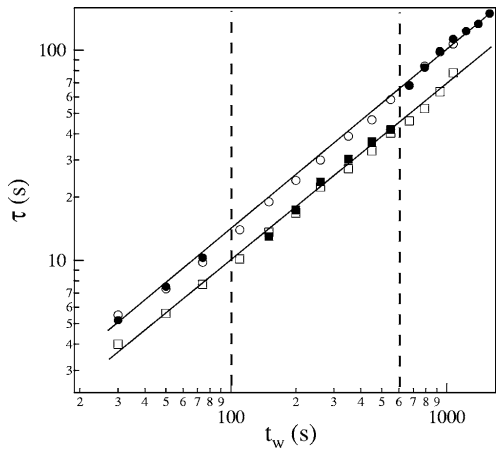

Figure 1.5: *Characteristic time of the correlation functions, measured through LSE by Kaloun and coworkers, as a function of the waiting time t_w. For $t_w < 100$ s, the system is not sheared (•), then it is sheared at moderate shear amplitude (■) and at $t_w > 600$ s the shear is stopped (•). Reference aging in the absence of shear (•) and under shear (□) is also reported. Figure from Ref. [97].*

after the shear quench exhibits. The sample is then submitted to various periodic shear protocols and dynamics of tracer particles are investigated during shear and after shear cessation. What they observe is that, though a moderate shear amplitude fastens the dynamics during its application, once the shear is ceased this acceleration doesn't affect the dynamics any more (Fig. 1.5). On the contrary, a strong shear completely rejuvenates the system, as the aging evolution obtained after the shear quench is retraced afterwards. As small amplitude oscillatory shearing does not significantly deform the fluid microstructure, comparison with steady shear experiments are not straightforward.

The statistical properties of multiple scattered light, probed in these DWS and LSE experiments, are not easily represented in terms of the particle density correlation function. For this reason, another technique is chosen in this thesis to probe the dynamics of colloidal glasses under shear. It is the dynamic light scattering technique in the single scattering regime (DLS), which, on the contrary, provides a direct measurement of the particle correlation functions. As will be explained in 3.1, the DLS technique probes indeed the intermediate scattering function of the colloidal particles $F^M(q, t_0, t)$ [8],

which plays a central role in both theoretical and numerical approaches.

1.3.2 Shear thickening and jamming

After a regime of shear thinning, when the shear stress exceeds a critical value σ_c, concentrated suspensions may exhibit a viscosity increasing with the applied stress. The increase of the viscosity may even lead to cessation of the flow, inducing a jamming transition. Shear thickening have been observed in hard sphere colloids and, mainly, in charged sphere colloids, where it is enhanced. The dependence of σ_c on particle size, concentration and polydispersity has been investigated by Maranzano and Wagner [9] in weakly charged and hard sphere colloids. The onset of shear thickening is facilitated by high concentration (as also shown in Fig. 1.3), large particle size, monodispersity of the colloids and by strong repulsive interactions between the particles. As will be explained in 2.5, the origin of the shear thickening phenomenon has been found theoretically in the formation of hydrodynamic clusters along the compressional direction (see Fig. 1.1). The size of these clusters grow with increasing stress, thus inhibiting the flow; while at high stresses clusters spanning the entire system may lead to flow instability at the jamming transition [104]. Systems permanently jammed after flow cessation have also been observed [44]. The shear thickening phenomenon is accompanied by a sign reversal in the first normal stress difference N_1, which is usually positive in non Newtonian liquids and turns out to be negative in such regime.

Experimental study of the shear induced cluster formation is not trivial. The first measurements investigating the particle structure of a system in the shear thickening regime were conducted through small angle neutron scattering by Laun and coworkers [11] and proved the existence of a short range order and the absence of long range order. In this kind of experiments [12], the quiescent scattering profile was recovered after shear cessation, showing that the structure formed under shear is reversible. Measurements of normal stress differences are extremely difficult, due to their very small value. However, the behavior of N_1 as a function of the velocity gradient direction have been investigated by Kolly and coworkers [13], who have shown that heterogeneities in the particle density form in a direction that depends on the flow direction. Direct observations have been used to better probe the cluster formation [14, 15, 16]. Confocal microscopy enables the observation of index-matched suspensions of colloidal particles. It has been observed

that, just after the cessation of flow at high shear rates, local particle density is extremely heterogeneous and highly concentrated regions appear. Crystallites forming under flow have also been detected and are supposed to be responsible for jamming [15, 16]. Nevertheless, confocal microscopy does not allow the observation of rapid motion of particles, thus the dynamics of the particles under flow haven't been investigated yet.

1.3.3 Yield stress and shear banding

In some complex fluids, when a stress below a critical yield stress σ_y is applied, the material deforms reversibly, recovering its original shape when the stress is removed. Once the applied stress reaches σ_y, the material deforms irreversibly. This behavior is observed in glassy colloids, where a network of interactions spanning the entire system may form and a finite stress is required in order to break this network before yielding. Also in electrically charged colloids and in concentrated hard sphere suspensions a yielding behavior may emerge. In these cases, a finite stress is necessary for the breakage of the macrocrystals characterizing the system structure at rest.

Glassy systems may also show a yielding behavior more complex than ideal yield stress fluids. It is the so called viscosity bifurcation behavior, observed by Coussot and coworkers in glassy clay suspensions [17]. For small stresses, the viscosity increases in time until the system stops flowing; while above a critical stress, the viscosity decreases continuously with time and the flow accelerates (thixotropic behavior). This critical stress increases with the time of preliminary rest before the stress application, due to spontaneous aging of the system. A simple theoretical model able to predict these results has been developed by the authors and is reported in 2.4.2.

Another interesting phenomenon which may show in complex fluids is shear banding: flow subdivides into different bands, parallel to the flow direction, characterized by different local shear rates. This phenomenon is induced by a decreasing branch in the flow curve (Fig. 1.6): in a controlled shear experiment, shear banding is observed when the stress falls in the interval where the flow curve is multivalued. Shear banding has first been observed in various non colloidal complex fluids, like surfactant wormlike micelles, liquid crystals and lamellar surfactant systems which can roll into multilamellar vesicles ("onions"). In these systems, a structural phase transition occurs under flow, with an ordered phase coexisting with a disordered phase. Thus the difference between the flowing bands lies in the microstructure. Shear

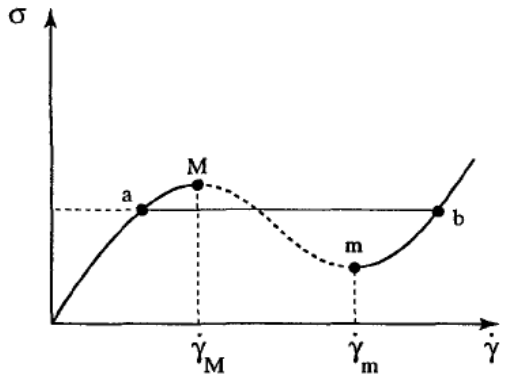

Figure 1.6: *Schematic representation of a non-monotonic flow curve. When the stress falls in the interval where the curve is multivalued, shear banding emerges. Figure from Ref. [58].*

banding has also been observed in yielding, glassy colloids, where the yield stress provides a multivalued region in the flow curve. When heterogeneous flow emerges in such systems, a band with null local shear rate, flowing as a solid block, may coexist with a band flowing at a finite local shear rate. This behavior has been called shear localization. According to numerical models [56], which are reported in 2.3.4, here the difference between the flowing bands is of dynamical nature.

Experimentally, shear localization behavior in glassy colloids have been investigated with the local velocity profile being accessed through magnetic resonance imaging (MRI) [18, 20, 45] or visualization techniques [19]. The first experiment evidencing the existence of a shear localization phenomenon was performed by Pignon and coworkers [19] on a Laponite suspension in a cone-plate geometry. In order to distinguish it from the local shear rate $\dot{\gamma}$, when necessary, the global applied shear rate will be represented with $\dot{\Gamma}$ in the following. After yielding, at very low applied shear rate $\dot{\Gamma}$, shear is localized in a thin layer in the bulk, which represents the interface between two bands flowing as solid bodies. A so called "stick-slip" behavior is observed, with the solid bands fracturing and rehealing periodically at the interface. As a result, the measured stress shows stationary oscillations with a time period $T \simeq 100$ s. When $\dot{\Gamma}$ is increased, this fracturing behavior ceases and the size of the layer where the shear is localized increases from the length scale of particle distance to the entire gap size. An oscillating flow behavior have

also been detected by Holmes and coworkers [45] for a colloidal star polymer in a Couette flow. Rapid fluctuations ($T < 1$ s) between a linear velocity profile and a profile characterized by shear localization were observed and interpreted as a flow induced transition between a jammed and unjammed state. Shear localization has been observed also in other clay suspensions in Couette and cone-plate geometry by Coussot and coworkers [18]. In their experiment, the size of the unsheared band is observed to increase with the time of rest before shear application, due to spontaneous aging of the system. The unsheared band size also depends on $\dot{\Gamma}$ and decreases with $\dot{\Gamma}$ until eventually disappearing over a critical $\dot{\Gamma}$, as in the experiment by Pignon and coworkers. However, while in the last the sheared band nucleates in the bulk, in all the other experiments it forms next to the wall and only two bands are observed.

It's important to remind that, in a circular Couette geometry, the stress of a steady flow varies along the gap between a maximum value at the inner wall and a minimum value at the outer wall. If the critical yield stress (or the critical stress in the viscosity bifurcation behavior) falls into this stress interval, thus the shear localization phenomenon will automatically occur, with the unsheared band next to the outer wall. In a cone-plate geometry instead, where the stress is constant across the gap, the shear localization phenomenon is only induced by the instability in the flow curve. Investigation of the dynamics of glassy colloids when shear localization occurs is still missing. Thus the fact that a different dynamics accompanies the different flowing bands haven't been confirmed experimentally yet.

CHAPTER 2

Microscopic theories and phenomenological models

Without aiming to an exhaustive review, in this chapter we will present some of the models that have been developed to describe the behavior of colloidal systems under shear. First, in order to better understand the general behavior of colloidal systems, we will start with the examination of the interactions between its constituents (2.1). A distinction between the microscopic mechanisms inducing a non-linear rheological behavior in glassy or non-glassy colloids is evidenced in 2.2. We will then focus on the various theories introduced to investigate the microscopic dynamics underlying the complex flow behaviors of glassy colloidal systems. Shear thinning and yielding behavior result from these theories, while sometimes the models can be extended to describe shear thickening or shear banding behaviors (2.3). Other models, mainly focusing on shear banding or yielding behavior are reported in a following section (2.4). Finally, we will present the theories describing the flow behavior of non glassy spherical colloids, characterized by a shear thinning region followed by the onset of a shear thickening regime (2.5).

2.1 Interactions between colloids

The statistical mechanical description of a colloidal suspension is facilitated by the possibility of coarse-graining over the solvent molecules, which are many orders of magnitude smaller than the colloidal particles. A transition from the microscopic level to the mesoscopic level is then achieved by integrating out the fast degrees of freedom accounting for the solvent molecule dynamics. This results in an interaction potential between the colloids depending on the solvent properties. Approximating it as a sum of pair-potentials between N spherical particles, the potential energy can be written as

$$V(\mathbf{r}^N) = \frac{1}{2}\sum_{i\neq j} v(r_{ij})$$

where $r_{ij} = \mid \boldsymbol{r_i} - \boldsymbol{r_j} \mid$. These potentials are equivalent to the interaction potentials between atoms in liquids or solids. Thus, methods developed for the statistical mechanical description of liquids and solids can be applied to derive macroscopic properties of colloidal suspensions. Considering two spherical particles of radius R, separated by a distance r, they induce on each other both attractions and repulsion. As neutral atoms interact by van der Waals attractive potentials [22], by summing over the atoms of the two extended spheres, the attractive interaction between the two colloidal particles results in the attractive potential $v_{vdW}(r)$. In a simple picture, this potential behaves as $-AR/r$ for $r << R$ and as $-A(R/r)^6$ for $r >> R$, where the Hamaker constant A can be expressed as the difference $\varepsilon_c - \varepsilon_s$ of the dielectric constants of colloids and solvent. Actually, the dielectric constant depends on the frequency ω of the electric field inducing polarization in the medium, but the dominant component in the Hamaker constant is the one at $\omega \simeq 0$. The strength of the van der Waals attraction can thus be controlled by changing the refractive index n_s of the solvent ($n_s \simeq \sqrt{\varepsilon_s}$). If this were the only interaction between the colloidal particles, the suspension would be unstable against aggregation. There are essentially two ways to stabilize the suspension: charge stabilization and surface protection by polymer layers.

Similarly charged particles dispersed in a polar solvent repel each other, while the presence of dissociated counter-ions and salt screen this repulsion over the Debye length λ_D. The resulting screened Coulomb potential $v_c(r)$, which also depends on the state of the solvent through the dielectric constant, decreases as $\exp(-r/\lambda_D)$ for $r > 2R$. Increasing the ionic strength of

the solution (e.g. by adding salt) induces a drop of both the amplitude and the range λ_D of this repulsion. When the Debye length gets smaller than the range of the attractions, the suspension becomes unstable and eventually flocculates. The competition between electrostatic repulsion and van der Waals attraction for charged colloidal spheres in a salty solution is the content of the DLVO theory [23, 24]. In the resulting pair potential, the attraction always dominates at very long and very short separations, while the electrostatic repulsion dominates at length scales in between, where it may induce a potential minimum. The overall behavior of the suspension then depends on the depth of this minimum and on the amplitude of the barrier that separates it from the minimum corresponding to quasi-contact between the colloidal particles.

Another classical method to avoid aggregation of the particles is to sterically protect the colloid surface with a polymer layer of thickness δ. In a good solvent for the polymers, such layers are swollen by the solvent and form brushes which repel each other for entropic reasons. The low polymeric concentration of the layers keeps the dielectric properties close to the solvent, without inducing additional van der Waals attractions. The resulting interactive potential between two colloids is very short-ranged and strongly repulsive and it is well approximated by a wall potential typical of hard spheres.

Different interaction potentials between the colloidal particles may induce very diverse structural and dynamical behaviors in the system. For example, in spherical charged colloids, the long range nature of electrostatic interactions may lead to the formation of a colloidal crystal at modest volume fractions, as particles under strong repulsive interactions move to well defined lattice points at which the separations between nearest neighboring particles are as distant as possible. Also in hard sphere suspensions, at high particle volume fractions, colloidal crystals form; while at higher volume fractions the suspension form a colloidal glass. The picture given above for model colloids is extremely simplified and doesn't comprehend non spherical colloidal particles, which are still very common. The interparticle pair potential of anisotropic particles, such as rods or disk-like colloids, may be more complex, but typically induces collective behavior at volume fractions much weaker than their spherical counterpart. For example, in charged discoidal particles a glassy behavior may result at very low volume fractions.

2.2 Glassy or non-glassy colloids under shear

Usually, the dynamics of a suspension is controlled by the Brownian motion of the colloidal particles; while in glassy dispersions, the slow structural rearrangement dominates the dynamics inducing aging. When a colloidal system is put under a shear rate $\dot{\gamma}$, a new timescale, $1/\dot{\gamma}$, is introduced into the problem. The effect of a constant shear rate $\dot{\gamma}$ on the particle dynamics of a non glassy system can be quantified by the Peclet number, defined as the ratio between the characteristic time of the shear rate ($1/\dot{\gamma}$) and the characteristic time of Brownian motion:

$$Pe = \frac{6\pi\eta a^3\dot{\gamma}}{k_B T} = \frac{a^2\dot{\gamma}}{D}$$

where D is the diffusion coefficient of the particles of diameter a in a solvent of viscosity η. This parameter may also be interpreted as the ratio between the energy induced by the shear flow ($\eta\dot{\gamma}a^3$) and the thermic activation energy ($k_B T$). At low Pe, the system exhibits a Newtonian behavior, while at $Pe > 1$ a shear thinning regime emerges and at much higher Pe a shear thickening behavior is observed. Instead, if the quiescent system exhibits a structural relaxation time scale τ_s much longer than a^2/D, then a second, "dressed" Peclet number, $Pe^* = \dot{\gamma}\tau_s$, can be defined [36]. This characterizes the influence of shear on the structural relaxation and increases drastically at the glass transition. The nonlinear rheology of colloids near the glass transition is driven by the competition between structural rearrangement and shearing that arises when $Pe << 1 < Pe^*$. A yielding behavior usually emerges at low stress; while once the system starts flowing, it is characterized by a shear thinning behavior. Very different microscopic mechanisms are responsible for the non linear rheology of these two prototypes of colloidal systems. As we will describe in 2.5, an order transition, induced in the structure by the flow when $Pe > 1$, is responsible for shear thinning in non glassy systems, while this order is disrupted when shear thickening occurs. In glassy colloids instead, shear thinning is already evident when $Pe << 1$ and ordering transitions can be assumed absent. Thus the origin of this phenomenon have to be found in the dynamical properties of the system, as described by the various microscopical models reported in 2.3. The diverse microscopic mechanisms underlying the shear thinning behavior also reflect in the shear banding phenomenon. A heterogeneous dynamics along the flow gradient direction induces the shear bands in a glassy system, while

in other complex fluids the phenomenon originates from a difference in the microstructure of the various bands.

2.3 Models for glassy colloids under shear

To investigate microscopically the dynamics of glassy colloidal systems under shear, theories and models often inspired by theoretical studies on molecular or atomic glasses have been developed. In these adapted models, the volume fraction of the colloids represents the role played by the temperature in the glass transition of supercooled liquids. Actually, colloidal suspensions can be considered as ideal systems to understand fundamental aspects of the glass transition. They are indeed tunable prototypes of atomic or molecular glassy systems, with controllable interactions, while the spatial and temporal length scales are advantageously much larger than in molecular systems and permit easier experimental investigation.

In the following, we will proceed to the review of the principal theories and models that describe the competition between spontaneous aging and shear rejuvenating effect. Not only the yield and shear thinning behavior emerges, but also a shear thickening behavior can be described microscopically by some of these theories, while the shear banding induced by the presence of a yield stress in the flow curve is predicted by some phenomenological models. In the soft glassy rheology model, proposed by Sollich et al. and presented in 2.3.1, the yielding and shear thinning phenomena emerge from the description of the energy distribution in the system. The extension of the mode coupling theory to shear flow have been proposed by various authors and will be explained in 2.3.2: in this case, the shear thinning behavior after yielding results from the decorrelation of the density fluctuations induced by the flow. In both cases, an extension of the models to describe a shear thickening system is attempted. The phenomenological simple model proposed by Derec and coworkers, which may also be adapted to the description of the shear banding phenomenon in yielding glassy colloids, is introduced in 2.3.3. Numerical models have been proposed in the literature to describe the various complex flow behaviors of colloids, including also the shear banding phenomenon. We have selected the numerical models more representative for us and present them in 2.3.4.

2.3.1 The soft glassy rheology model

A promising route for the investigation of the interplay between the drive and the relaxation of a glassy system is the one followed by Sollich and coworkers [27, 28], which extends the phenomenological "trap" model to driven systems, giving rise to the so-called soft glassy rheology (SGR) model. The picture emerging from this model characterizes the shear thinning phenomenon as the result of the energy pumped in the system by the shear perturbation. This energy let the system overcome the deep energy barriers that confine it in the arrested phase, thus accelerating the structural dynamics.

Before presenting the SGR model, we need to introduce the concept of the effective temperature in a glassy system. During the aging regime, the energy scale for mesoscopic rearrangements ΔE typically gives $\Delta E >> KT$, though the dynamics are not completely frozen and exhibit slow evolution. Empirically, it is possible to explain many of the rheological properties of soft glasses by assuming that there is some sort of effective temperature T_{eff} at which the structural degrees of freedom (accounting for the slow dynamics) thermalize. As the waiting time t_w passes, the effective temperature slowly relaxes to the vibrational temperature, which characterizes the fast dynamics. Quantitatively, this is shown by studying the fluctuation dissipation theorem (FDT), as the same aging behavior is observed both in the correlation and response function of some significative variable [30]. Whereas at equilibrium the bath temperature appears in the FDT, the theorem has to be generalized in non-equilibrium aging systems at a given t_w by replacing the bath temperature with the effective temperature (which can thus be defined by a generalized FDT). Adding the effect of a shear field to this simplified approach leads generically to shear-thinning behavior; while introducing extra parameters in the model, shear thickening and jamming effects can be described. Let's start by introducing the trap model [31, 32], which we will later extend to obtain first the SGR model and then the jamming SGR model.

The trap model

One of the simplest model of glasses was obtained through a mathematical trick, which reduces the glass transition to an effective one-body problem showing a glass transition [49]. The trap model considers an ensemble of independent particles moving by activated hopping between uncorrelated traps. There is a distribution of barrier heights $\rho(E)$ and the jump rate

out of a trap is $\Gamma_0 \exp(-E/x)$, where x represents the effective temperature ($x = KT_{eff}$). These dynamics is defined by the equation of motion for a probability distribution $P(E,t)$ of traps occupied:

$$\dot{P}(E,t) = -\Gamma_0 e^{-E/x} P(E,t) + \Gamma(t)\rho(E) \tag{2.1}$$

where the first term on the right is escape from and the second is jump into traps of energy E, while $\Gamma(t) = \langle \Gamma_0 \exp(-E/x) \rangle_P$. Bouchaud [32] showed that by choosing $\rho(E) \sim \exp(-E/x_g)$, for large E, a unique stationary solution to equation 2.1 exists for $x > x_g$, whereas no stationary solution exists for $x < x_g$. It is convenient to set $x_g = 1$. This transition is reminescent of a glass transition: the system is ergodic for $x > 1$ and non ergodic for $x < 1$. In particular, above the transition ($x > 1$) one must wait a long time for the deepest traps to become populated, but the distribution $P(E,t)$ converges to the equilibrium state. On the contrary, below the transition ($x < 1$), the system evolves forever into deeper and deeper traps without reaching a steady state. This leads to the aging behavior.

The SGR model

To extend the trap model to rheology, Sollich and coworkers [27] associated the wells with harmonic mesoscopic regions, where a local strain variable l may be defined. As the system is sheared, such regions will deform elastically, gaining a stored energy $\frac{1}{2}kl^2$ (where k is an elastic constant), up to a yield point, characterized by a strain l_y and a maximal elastic energy $E = \frac{1}{2}kl_y^2$. The local shear stress is given by kl and, at the yield point, the mesoscopic regions rearrange to new positions in which they are less deformed, thus relaxing stress. While the region is distorted by the stress, the stored elastic energy can be used to overcome the energy barriers and this principle can explain qualitatively the macroscopic shear thinning behavior. A distribution of the yield energies E is assumed to model the effects of structural disorder. The state of a macroscopic sample is then characterized by a probability distribution $P(l, E; t)$, ruled by the following equation:

$$\dot{P}(E,l;t) = -\dot{\gamma}\partial P(E,l;t)/\partial l - \Gamma_0 e^{-(E-kl^2/2)/x} P(E,l;t) + \Gamma(t)\rho(E)\delta(l) \tag{2.2}$$

where the first term on the right is from the deformation of local elements between jumps and the others have the same interpretation as in the analog equation for trap model 2.1. The macroscopic stress of the system is given by

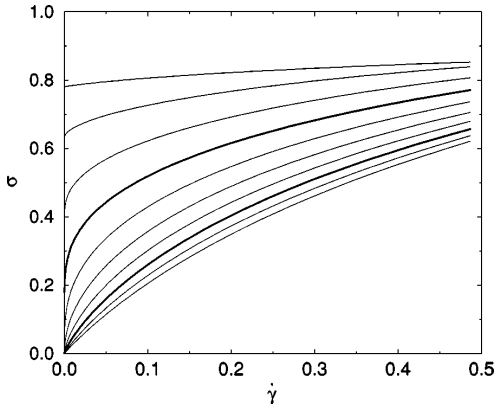

Figure 2.1: *Flow curve for the SGR model, with x increasing from top to bottom; the bold lines are for $x = 2$ and $x = 1$. A yield stress shows up for all curves with $x \leq 1$. The figure have been taken from Ref. [33].*

$\sigma = k\langle l \rangle_P$. From equation 2.2, one finds out that flow interrupts aging and ergodicity is restored with a steady state probability distribution by imposing a steady $\dot{\gamma} > 0$. Steady state flow curves can be obtained and are shown in Fig. 2.1. In the small $\dot{\gamma}$ regime, one finds a Newtonian fluid for $x > 2$, when $\sigma = \eta\dot{\gamma}$. In the model, the viscosity is simply the average relaxation time to overcome the traps $\eta = \langle \exp(E/x) \rangle_{eq} = \langle \tau \rangle_{eq}$, taken over the equilibrium distribution of energies. For $1 < x < 2$ a power-law fluid with $\sigma \sim \dot{\gamma}^{x-1}$ is obtained, while for $x < 1$ the so called Herschel-Bulkley behavior, with the appearance of a yield stress, shows up: $\sigma(\dot{\gamma}) - \sigma_y \sim \dot{\gamma}^{1-x}$. Sollich and coworkers also obtain the behavior of the complex dynamic shear modulus $G(\omega) = G' + iG''$ for the various regimes of the x parameter in an oscillatory flow [27, 28].

In a following work, Hébraud and Lequeux [29] have proposed another model, still based on the scheme of a system divided into mesoscopic blocks carrying a stress σ, which this time depends on both time and position. In their model, when the stress in a block reaches the critical stress value, the block stress is set to zero and, as a consequence, the stress field is modified in the whole sample. They define a probability $P(\sigma, t)$ of finding a stress σ in a block at time t and thus utilize a mean field approach to build an equation for the evolution of P. As a result, they find a flow curve characterized by a Newtonian regime or yield stress at low shear rates, a slow variation of the

stress for higher shear rates and then an apparent Newtonian regime for very large shear rates.

The jamming SGR model

The SGR model is exclusively shear thinning, with a monotonic flow curve for all x. However, one can adapt the model to describe shear thickening materials. The simplest route, proposed by Head and coworkers [34, 33], is to declare that the noise temperature x is no longer constant, but is a decreasing function of the global shear stress: $x = x(\sigma)$. The basic idea is that in shear thickening materials, stress can force particles to come very close, thus forming clusters. This will make local rearrangements more difficult and a lower noise temperature will characterize this state of the system. Depending on the form of $x(\sigma)$, a range of scenarios can be obtained. Many choices of $x(\sigma)$ produce flow curves with nonmonotonic regions, which exhibit hysteresis in $\sigma(t)$ under ramping the shear rate $\dot{\gamma}(t)$ first upwards and then downwards. Moreover, a subset of these $x(\sigma)$ also give rise to a jammed state for a range of applied stresses. The criterion for this to arise is that the curve of $x(\sigma)$ drops below the inverted SGR yield stress curve $\sigma_y(x)$. For an imposed shear rate that decays to zero at late times, a jammed configuration is defined as one with a finite asymptotic stress, $\sigma(t) \sim \sigma_y > 0$ as $\dot{\gamma}(t) \to 0^+$ and $t \to \infty$. It is found that whether or not this configuration is reached depends on the entire strain history of the system.

Another way proposed by Head and coworkers to modify the SGR model in order to obtain a shear thickening behavior, is to consider a noise temperature depending on the local strain l: $x = x(l)$, with x decreasing with increasing l. Under these conditions, the flow curves are always monotonic and continuously shear thickening, with a steady flow that is always reached under a constant imposed strain rate. However, for a range of imposed stresses and some choices of $x(l)$, the response is not steady flow, but spontaneous oscillation: $\dot{\gamma}$ periodically oscillates around a well-defined mean.

2.3.2 Extension of the Mode Coupling Theory

Another approach to the investigation of the arrest and flow behavior of glassy systems is the mode coupling theory (MCT), which is a mean field theory proposed by Göetze [35] to describe the dynamics of supercooled liquids and glasses. MCT has been particularly successful for colloidal suspensions

and can be extended to include the presence of an external drive inducing flow in such systems. In the following, we will first give a hint at the MCT, then we will present the extension of the theory to systems under shear that have been proposed by various authors, and finally we will introduce a model that accounts for jamming behavior in the context of the MCT.

The Mode Coupling Theory

This is not the place to explain the MCT in detail [35], only those aspects pertinent to the developments of the theory to sheared glasses will be outlined. The theory was developed to describe the glass transition in supercooled molecular liquids. However, in these systems the dynamical timescales are often too short to be accessed experimentally and the most promising systems for quantitative tests of the MCT have been dense suspensions of purely repulsive particles, for which the temperature parameter used in the theory have to be replaced by the inverse particle volume fraction. The central quantities of the theory are the density correlators $F(\boldsymbol{q},t)$. In a liquid, the system is ergodic and $F(\boldsymbol{q},t)$ decays to zero with time for all $\boldsymbol{q}$. On the contrary, in a glass $\lim_{t\to\infty} F(\boldsymbol{q},t) = f_{\boldsymbol{q}} > 0$, where $f_{\boldsymbol{q}}$ is a nonergodicity parameter characteristic of the arrested state. A finite $f_{\boldsymbol{q}}$ represents the inability of the structure to relax on lengthscales $\sim 2\pi/\boldsymbol{q}$, preventing an initial fluctuation from fully decaying. Therefore, upon smooth variation of the density, the system exhibits a sudden arrest transition corresponding to a discontinuous jump of the non ergodic parameter from zero to a finite value. A closed equation of motion can be found for the correlators; for a colloidal system, by making the suitable approximations, the result is [35]:

$$F(\boldsymbol{q},t) + \tau\dot{F}(\boldsymbol{q},t) + \int_0^t m(t-t')\dot{F}(\boldsymbol{q},t')dt' = 0 \tag{2.3}$$

where τ sets the timescale for the microscopic dynamics, while $m(t-t')$ is a memory function. The structural relaxation is dominated by particle interactions which either cage or bond a central particle among its neighbors. Near the glass transition, either mechanism leads to a slowing down of particle rearrangements accompanied by growing memory effects. The memory function describes the retarded friction effect which arises by this caging process. The cage effect is driven by the local order as measured in the height of the principal peak of the static structure factor, $S_{\boldsymbol{q}_p}$, where the wavevector $\boldsymbol{q}_p$ is inversely related to the average particle spacing. The decay time of this dominant density mode sets the structural relaxation time.

MCT for glassy systems under flow

The effect of a constant shear rate $\dot{\gamma}$ on the particle dynamics can be measured by the Peclet number, as explained in 2.2. Here we are interested in the case when $Pe << 1$. In this regime, the steady state structure factor differs only smoothly from the quiescent $S_{\boldsymbol{q}}$ around $\boldsymbol{q} \sim \boldsymbol{q}_p$, thus the effect of shear cannot lie in a destruction of the quiescent local order. Rather, the effect needs to arise from a shear-induced decorrelation of the memory built up in the collective cage mode. Particles separated by a small distance in the flow gradient direction become well separated for times beyond $1/\dot{\gamma}$. Beyond this timescale, any system at nonzero flow rate should loose memory of previous configurations, so that ergodicity is restored. In the $\boldsymbol{q}$-space, the important density fluctuations, characterized by $\boldsymbol{q} \sim \boldsymbol{q}_p$, are advected on this timescale to higher $\boldsymbol{q}$, where they decay rapidly. Even those fluctuations that are not directly advected become ergodic. Hence cages, that transiently immobilizes particles, are dissipated, thus resulting in a shear thinning behavior.

These are the considerations underlying the approaches proposed by Fuchs and Cates [40] and by Miyazaki and Reichman [41] for the extension of the MCT to systems under a stationary shear flow. The physical picture of these two works is quite similar and also the results show many similarities. To incorporate shearing into the MCT equations containing the density correlators, they need to consider that translational invariance is violated under shear. Another spatial symmetry is valid [81] by defining a time dependent position vector $\boldsymbol{r}(t) = \boldsymbol{r} + \dot{\gamma} t x \boldsymbol{e}_y$, where $\boldsymbol{e}_y$ is the flow gradient direction, while $\boldsymbol{e}_x$ is the flow direction. In the $\boldsymbol{q}$-space, this reflects in a coupling of fluctuations of wavevector $\boldsymbol{k}$ with later fluctuations of wavevector $\boldsymbol{k}(t) = \boldsymbol{k} + \dot{\gamma} t k_y \boldsymbol{e}_{\boldsymbol{x}}$. In both works, hydrodynamic interactions are neglected [37] and only the Brownian contributions are considered. Under these conditions, they construct a nonlinear equation for the correlators, where the effect of the shear appears in a generalized memory function. The solution is evaluated numerically for a two-dimensional model of colloidal suspension by Miyazaki and Reichman and the result is a structural relaxation time decreasing as $\dot{\gamma}^{-m}$ with $m = 0.8$. Fuchs and Cates even go further by developing the so called isotropically sheared hard spheres model [36]. As a result, they obtain a shear-thinning behavior with exponent $m = 1$ and predict a transition in the flow of these shear-thinning fluids, with diverging viscosity upon increasing the interactions, and a solid yielding, with a yield stress that is finite at (and beyond) the critical packing fraction characterizing the glass point.

Actually, the first theoretical work extending the MCT to supercooled liquids under stationary flow was developed by Berthier, Barrat and Kurchan [38], who proposed a schematic model based on the exactly solvable p-spin model [43]. As a result, they obtain that a fluid above the glass transition temperature, which has two well-separated relaxation time scales at equilibrium, shows instead an acceleration of the slow structural relaxation when sheared in a certain range of shear rates. In particular, the following relation for the slow relaxation time τ_s is predicted: $\tau_s \sim \dot{\gamma}^{-2/3}$. This shear thinning behavior is accompanied by the appearance of an effective temperature for the slow degrees of freedom, resulting in the violation of the fluctuation-dissipation theorem. Below the glass transition temperature, when the system is in a nonergodic state and the slow dynamics at rest is characterized by an effective temperature, the shear induces a shear thinning behavior and a stationary state is reached. Moreover, by constructing the free-energy landscape of the model, the existence of a yield stress can be explained. Above the dynamical transition temperature T_c, the available phase space is dominated by one large basin in the free energy, corresponding to the paramagnetic liquid state. At T_c, a threshold level in free energy appears, below which the free-energy surface is split into exponentially many disconnected regions. When the system is prepared in one of the deep regions below the threshold, a weak driving force is expected to have no effect beyond a trivial elastic response of the system, as it is not strong enough to make the system overcome the barriers. If instead a strong drive is applied, the system should escape the low-lying valley and surface above the threshold, where the drive will suffice to keep it forever. These expectations are verified by calculations proving the existence of a static yield stress $\sigma_y(T)$ in the model, as defined by the minimal force required to make it flow.

As a consequence of the shear thinning and yielding behaviors found in the model [39], a multivalued flow curves is expected in the interval of shear stress $\sigma \in [0, \sigma_y]$. Therefore, shear localization would spontaneously develop in such a stress interval, with a flowing band ($\dot{\gamma}_{local} > 0$) coexisting with a non-flowing band ($\dot{\gamma}_{local} = 0$).

Schematic model for the jamming transition

The shear thickening phenomena has been explained theoretically in terms of hydrodynamic interactions, as we will describe in 2.5. However, a recent experiment by Bertrand and co-workers [44] have shown a shear induced

jamming transition in a concentrated suspension that cannot be explained by hydrodynamic forces alone. The jammed state persisted indeed after cessation of shear. These observations have inspired a work by Holmes and coworkers [45], where a schematic scalar model of the jamming transition in the context of the MCT have been developed. Their speculative scenario for the formation of the shear-induced glass is the following: the applied shear stress induces a jamming transition through hydrodynamic interactions at concentrations somewhat lower than would be required without the stress. In the arrested state, flow ceases but stress remains and is now sustained by interparticle and entropic forces rather than hydrodynamics.

Two features are introduced in the MCT approach in order to allow shear-thickening and jamming scenarios to emerge: strain-induced memory loss, which we have already introduced to account for shear thinning behavior and stress-induced arrest. Stress can indeed hinder diffusion by distorting cages and creating closer contact between particles. Holmes and coworkers propose a schematic model considering a single correlator $F(t)$, rather than the infinite set $F_q(t)$ used in the MCT. The memory function is then simplified and, to account for both effects induced by shear, is modelled as follows:

$$m(t) = (v_0 + \alpha\sigma)\exp(-\dot{\gamma}t)F^2(t)$$

where v_0 represents the system tendency to structural arrest in the absence of any external drive and α represents the degree to which the intrinsic memory of the system is enhanced by a shear stress σ. The exponential function accounts for the flow-induced memory loss, which thus becomes important as $\dot{\gamma}t \geq 1$. To close the schematic model, an equation for the viscosity is defined [46]: $\eta = \int_0^\infty F(t)dt = \tau$. The model has been solved numerically and, for nonzero α, a nonergodic solution at zero shear rate always turns out for σ sufficiently large. However, this state is unstable with respect to an ergodic solution whenever the latter exists, meaning that a flowing state is preferred to a jammed one if both exist. Fig. 2.2 shows three thickening scenarios, depending on model parameters: upon increasing v_0, there is a progression from a monotonic, continuously shear-thickening curve, via a nonmonotonic S-shaped curve, to a curve that extends right back to the vertical axis. As the flow curve with negative slope are unstable to shear banding, in any experiment at controlled shear rate, the stress would be expected to jump discontinuously from the lower to the upper branch in the unstable region. The steady state and the unstable solutions for the flow curves also emerged in the jamming SGR model (2.3.2). Additionally, for the largest values of the

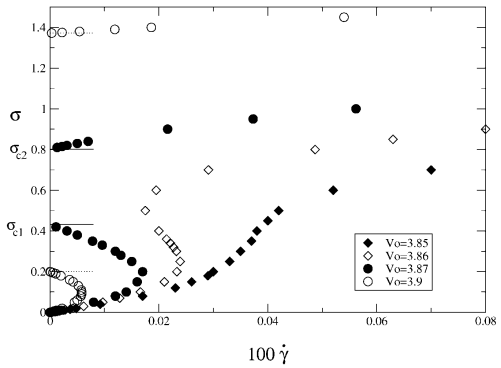

Figure 2.2: *Flow curves for different values of the v_0 parameter. For the two largest values, it appears that in the stress window $\sigma_{c1} < \sigma < \sigma_{c2}$, the relaxation time has diverged showing a jamming transition. Figure from Ref. [45].*

parameter v_0, there is a range of stress ($\sigma_{c1} < \sigma < \sigma_{c2}$) for which the shear rate returns to zero: this is the region where non ergodic solution exists and the jammed state is stable.

2.3.3 Phenomenological Maxwell model

A simple model for the rheology of soft glassy materials, with no reference to any microscopic mechanism, has been proposed by Derec et al. [47]. Also a shear banding behavior can emerge from this model under certain conditions [50], providing one of the most exhaustive descriptions of this phenomenon in a glassy colloid. In the following, we will present the model, that results in a yielding and shear thinning behavior, while the extension to the description of the shear banding phenomenon will be explained in the next section. Derec and coworkers adopt a homogeneous, scalar description, which focuses on the collective relaxation mechanism and captures the competition between spontaneous aging and flow-induced rejuvenation. Their approach is based on the Maxwell model, which is the simplest visco-elastic model, with a single time scale, but with a relaxation rate that evolves in time and is thus history-dependent. The equation linking the stress σ to the shear rate $\dot{\gamma}$ contains a purely viscous element in series with an elastic one:

$$\partial_t \sigma = -a(t)\sigma + G\dot{\gamma}$$

where G is the shear modulus and a is the so called fluidity, which is the inverse of the mechanical relaxation time: $a = 1/\tau$ and thus will be low in the vicinity of the glassy phase. To close the system, the equation for the fluidity stands:

$$\partial_t a = -f(a) + g(a, \sigma, \dot{\gamma}) \tag{2.4}$$

where f, which accounts for spontaneous aging and g, accounting for shear induced fluidization, are both positive functions. For long waiting times and weak shear, the fluidity is expected to be small, so we are interested in the behavior of f and g in the vicinity of $a \simeq 0$. Using formal expansions, the two functions are expressed as

$$f(a)_{a\to 0^+} \simeq -ra^\alpha + va^{\alpha+\beta}$$

$$g(a, \sigma, \dot{\gamma})_{a\to 0^+} \simeq u\sigma^n \dot{\gamma}^m a^p$$

The r parameter depends on the concentration and is positive in the liquid phase and negative in the glassy one: $r \sim -(\Phi - \Phi_c)$. This general model encompasses various models in the literature corresponding to specific choices for the phenomenological exponents (α, β, n, m, p) [48]. Derec and coworkers solve the general case and also present a specific simple case which we will summarize in the following. They fix $\alpha = 2$, which is the smallest value for α such that the fluidity relaxes slower than the stress in the glassy phase. The fluidity is thus the memory parameter in the system. For the other parameters, they choose $\beta = 1$, $n = 0$, $m = 2$ and $p = 0$. The system is quenched at $t = 0$ through a strong oscillating shear that fluidizes it, is then left to relax spontaneously and finally is submitted to a constant shear rate starting at $t = t_w$. When the steady shear is turned on, the response of the system will be in the linear regime as long as the coupling term $u\dot{\gamma}$ remains smaller than ra^2. This earlier regime may provide a way to follow aging in the system: they find that in the glassy phase the mechanical timescale is $\tau(t) = 1/a(t) \sim t^\mu$ for long times, with $\mu = 1/(\alpha - 1)$. In this specific case, $\mu = 1$ and we are in the so called full aging regime. After a certain time, as the fluidity decreases, the response of the system in the glassy phase becomes non linear. In this regime, at low shear rates, a yield stress appears in the flow curve and after yielding the time scale imposed by the shear rate determines the fluidity ($a \propto \dot{\gamma}$). In the liquid phase ($r > 0$), a newtonian regime is found at low shear rates. At higher shear rates, the liquid and glassy behavior both merge in a shear thinning steady regime with an effective viscosity $\eta \propto \dot{\gamma}^{-2/3}$.

In the general case, keeping generic exponents in the model, the yield stress in the low shear non linear regime holds whenever the parameter $\epsilon = \alpha - n - p$ is null, while a power-law fluid shows up when $\epsilon > 0$. The low shear rate behavior in the liquid phase is still Newtonian, while for high shear rates a shear thinning power law regime is obtained for both the liquid and glassy phase. A similar result of the flow behavior in the liquid and glassy phase had already been obtained through the MCT theory approach on the p-spin model [38], as we explained in 2.3.2.

Shear banding

Under certain conditions, the general model just presented can also describe heterogeneous flows in yield stress fluids, as shown by Picard and coworkers [50]. A nonmonotonic local flow curve is required, with a yield stress and a decreasing branch for small but nonzero values of $\dot{\gamma}$. In order to describe spatial heterogeneities in the flow, the authors need to account for the effect of a heterogeneous value of the fluidity on the dynamics. This is achieved by adding a diffusion term $D\nabla^2 a$ in the equation 2.4 for the fluidity. Boundary conditions for the fluidity equation are also required and can sensitively influence the solution of the system of equations defined in the model. Indeed, the wall affects the dynamics of the fluid in its neighborhood [51] and can have important consequences on the overall macroscopic behavior. Two limiting simple cases are considered for the boundary conditions of the fluidity, while direct wall slippage is excluded. The geometry chosen to develop the model is the plane Couette flow, with the two bounding plates located at $y = 0$ and $y = H$ and the top plate moving along x at a velocity V. The equations defining the model for a simple shear geometry are thus the following:

$$\partial_t \Sigma = -a(t)\Sigma + \dot{\gamma}$$

$$\partial_t a = -f(a) + h(a)\Sigma\dot{\gamma} + D\partial^2_{yy} a$$

$$\int_0^H dz \dot{\gamma}(y,t) = V = \dot{\Gamma} H$$

$$a|_{y=0,H} = a_w \quad \text{or} \quad \partial_y a|_{y=0,H} = 0$$

where $\Sigma(t)$ and $\dot{\Gamma}(t)$ are global variables for the stress and the shear rate, whereas $a(y,t)$ and $\dot{\gamma}(y,t)$ are local variables.

Under imposed stress Σ, the dynamics of the field $a(y)$ can be determined by a Σ dependent functional evolving towards a local minimum. Two steady

state solutions are found and the one selected by the system depends on the initial conditions. There is a frozen branch corresponding to a frozen bulk at $a \sim 0$, with layers of finite fluidity close to the wall induced by the boundary conditions. And a fluidized branch with the bulk at a finite value of a (corresponding to the stress Σ on the up-rising part of the local flow curve), with layers of possibly weaker fluidity close to the wall. The flow curve at imposed stress Σ is plotted in Fig. 2.3. For stress values Σ lower than a limiting value σ_d, only the frozen branch is stable, whereas for values larger that a given σ_i only the fluidized branch is. The two limiting values depend on the boundary condition of a, as the walls can act as nucleation centers for either the frozen or fluidized phase. For intermediate values of the stress $\sigma_d < \Sigma < \sigma_i$, both branches are possible solutions at long times and the one selected depends on the initial conditions, i.e. on the system history. When increasing the imposed fixed stress, the sudden jump from the frozen to the fluid branch can thus be anticipated at a value σ^*, depending on the preparation scheme, which fixes the transition from a final frozen to a final fluid steady state. Therefore, the system has an effective yield stress between σ_d and σ_i.

The case of an imposed shear rate $\dot{\Gamma}$ is more complex, as both the field $a(y,t)$ and $\Sigma(t)$ evolve in a coupled way in the system of equation describing the model. The resulting macroscopic picture is represented on Fig. 2.3. The two branches resulting from an imposed stress are still present in this case, but for intermediate shear rates the system stabilizes in a banded state at a stress very close to σ^*. In this shear banding state, a fraction of the system is characterized by a fluidity close to zero, while another fraction has a fluidity close to $a(\sigma^*)$. The width of the fluidized region h_f is typically given by $h_f \sim H\dot{\Gamma}/\dot{\gamma}^*$, where $\dot{\gamma}^* = a(\sigma^*)\sigma^*$.

Finally, in a narrow vicinity of the transition from the quasi-homogeneous branches to the situation of coexisting shear bands, various phenomena can occur in the vicinity of the wall: nucleation of thin layers of fluidity different from the bulk, or of layers of periodically oscillating fluidity with features characteristic of a "stick-slip" behavior. In particular, for small wall fluidity and imposed shear rate, a layer localized either close to the wall or in the middle of the cell shows a fluidity oscillating between a frozen and a fluidized state, while the rest of the system remains frozen. The system rapidly relaxes to the frozen state (small fluidity), while the stress increases until a limit where the fluidity abruptly increases, so the fluid is suddenly sheared. To maintain a fixed global shear rate, σ relaxes quickly and the cycle starts again,

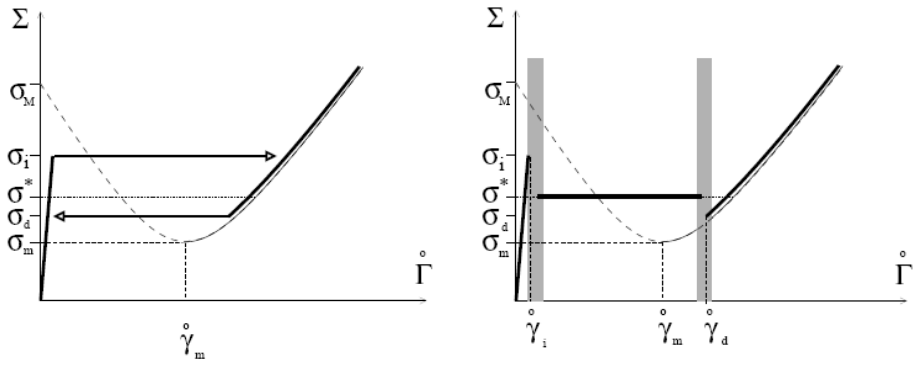

Figure 2.3: *Schematic flow curve at imposed stress Σ (left panel) and at imposed shear rate $\dot{\Gamma}$ (right panel). Thick lines represent the macroscopic and dashed and continuous lines the local flow curves. The limits of stability of the frozen and fluid branch are fixed by σ_i and σ_d in the left panel and by $\dot{\gamma}_i$ and $\dot{\gamma}_d$ in the right panel. At imposed shear rate, between these two values shear bands from in the system. At the transition between the two branches (grey areas), stable or oscillating thin layer structures are observed in the vicinity of the wall. The figures have been taken from Ref. [50].*

as shown in Fig. 2.4. Oscillating response under steady driving has also been observed in the model presented in 2.3.1 for shear thickening materials [45]. Contrarily to the present model, that one described the homogeneous behavior of a system, as no spatial heterogeneities were introduced in the formalism, while the shear rate oscillated at a fixed stress.

2.3.4 Numerical Simulations

Non-linear rheological behavior of complex fluids can also be described through computer simulations of supercooled liquids under shear. Yamamoto and Onuki have done molecular dynamics simulations of a binary liquid with a soft-core potential near the glass transition temperature [81], while Barrat and Berthier numerically investigated a binary Lennard-Jones mixture [53, 54, 55]. A shear localization behavior has also been predicted by Varnik et al. [56] using this last model, as we will report in the following section.

Yamamoto and Onuki define bonds between neighboring particle pairs owing to the sharpness of the first peak of the pair correlation functions and they investigate the system dynamics by following the bond lifetime τ_b,

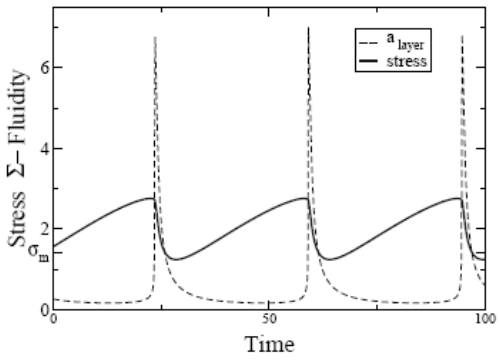

Figure 2.4: *Evolution of the global stress and of the maximum fluidity in the oscillating layer. Figure from Ref. [50].*

which turns out to be a decreasing function of the temperature T. Upon structural rearrangements, the bonds break collectively in the form of clusters, whose sizes grow with lowering the temperature. When a simple shear flow is applied to the system, the perturbation drastically changes the glassy dynamics when $\dot{\gamma}$ exceeds the inverse of the structural relaxation time. The bond breakage time, which is proportional to the structural relaxation time, has the following dependence on the shear rate:

$$\frac{1}{\tau_b(\dot{\gamma})} \simeq \frac{1}{\tau_b(0)} + A\dot{\gamma} \tag{2.5}$$

where A is a constant. Thus the bond breakage rate $1/\tau_b(\dot{\gamma})$ consists in a thermal breakage rate, represented by the first term on the right, which is strongly dependent on T, and a shear induced breakage rate, proportional to $\dot{\gamma}$. In the strong shear condition ($\tau_b(0)\dot{\gamma} > 1$), jump motions are induced by shear on the timescale of $1/\dot{\gamma}$. When investigating the density autocorrelation function, the authors find a stretched exponential form $\exp[-(t/\tau)^{\beta}]$ for the slow relaxation, with $0 < \beta < 1$ and β increasing with $\dot{\gamma}$ and T. This stretched behavior of the slow relaxation is induced by large-scale heterogeneities in the bond breakage process, marked by the coexistence of relatively weakly and strongly bonded regions. As the shear rate or the temperature are increased, the breakage occurs more homogeneously (β increases). In conclusion, the authors determine the viscosity of the system from the bond breakage time:

$$\eta(\dot{\gamma}) \cong A_\eta \tau_b(\dot{\gamma}) + \eta_B$$

where η_B represents a background viscosity and A_η is a constant. Under strong shear ($\tau_b(0)\dot{\gamma} > 1$), the viscosity has the temperature independent behavior: $\eta(\dot{\gamma}) \cong (A_\eta/A_b)/\dot{\gamma} + \eta_B$. If the background viscosity is negligible, a constant limiting stress follows: $\sigma_y \cong A_\eta/A_b$.

In the molecular dynamics simulations by Barrat and Berthier, results comparable with the main predictions of mean-field calculation [38] are obtained. When a shear rate $\dot{\gamma}$ is applied to the system, a non-equilibrium stationary state is reached after a transient of a few $\dot{\gamma}^{-1}$. A shear thinning behavior is thus established both in the liquid and glassy phase, with an exponent depending on temperature. When $\dot{\gamma}^{-1}$ is larger than the slow relaxation time, over the glass transition temperature a Newtonian regime is found instead. In this context, they also study the FDT and its violations. In the glassy phase, the violation of the theorem is similar to the one observed in an aging system in the absence of an external drive. In the fluid state, violations of the FDT appear only when the fluid is driven beyond the Newtonian regime, and are then similar to that observed in the glassy phase. By increasing the strength of the driving force, the effective temperature defined by the generalized FDT increases.

Shear localization

Molecular dynamics simulations on the same glassy model investigated by Barrat and Berthier [53] have been performed by Varnik and coworkers [56] and shear localization phenomena has been observed. The flow curve exhibited by the model system is shown in Fig. 2.5. For global shear rates $\dot{\Gamma}$ smaller than a critical value $\dot{\Gamma}_c$, the system separates into a fluidized band, with a finite local shear rate and an unsheared band. Due to the finite size of the simulation box, the appearance of the shear band can occur equally likely on both sides of the cell. In experimental systems, this symmetry is not expected as one of the two solutions would be stabilized by the large size of the system. By increasing the global shear rate, the thickness of the sheared region grows, passing from the order of a few atomic diameter to the whole gap size. When $\dot{\Gamma} > \dot{\Gamma}_c$, the flow is homogeneous with a linear velocity profile.

Similarly to the results by Picard et al. 2.3.3, at very small global shear rates, the authors observe a time dependence of the shear stress characteristic of stick-slip phenomenon. As shown in Fig. 2.6, the stress oscillates between a value close to the yield stress and a value smaller than the one obtained in

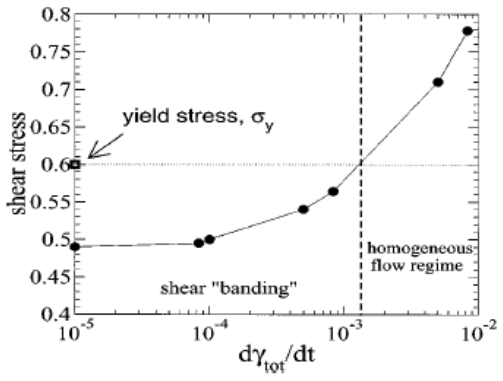

Figure 2.5: *Shear stress versus imposed shear rate* $\dot{\Gamma} = d\gamma_{tot}/dt$. *Under imposed shear rate, if the corresponding steady state stress falls below the horizontal line, a heterogeneous flow is expected, while the flow will be homogeneous in the opposite case. The vertical line marks the shear rate* $\dot{\Gamma}_c$ *on the boundary of this two flow regimes. Figure from Ref. [57].*

a homogeneous flow. Qualitatively, this behavior is obtained when the thickness of the sheared layer becomes of the order of a few particle diameters, which also corresponds to the width of the interface separating the sheared and jammed regions. Finally, static properties are found to be constant across the gap and a purely dynamical distinction between the two bands is observed instead, as shown by the density correlation functions shown in Fig. 2.7. There are indeed two limiting behaviors of the correlation functions, corresponding to the sheared and jammed regions, with a rapid change from one behavior to the other within a few layers localized at the interface between the two bands. In the jammed region the system behaves as a glassy solid as $\Phi_q(t; z)$ shows only a decorrelation accounting for the fast dynamics and does not relax to zero on the simulation timescale. On the contrary, in the sheared region the correlation function exhibits a two-step relaxation, with a finite structural relaxation timescale. In order to validate experimentally the results of the model, the authors thus encourage a determination of velocity profiles together with a local probe of the dynamics.

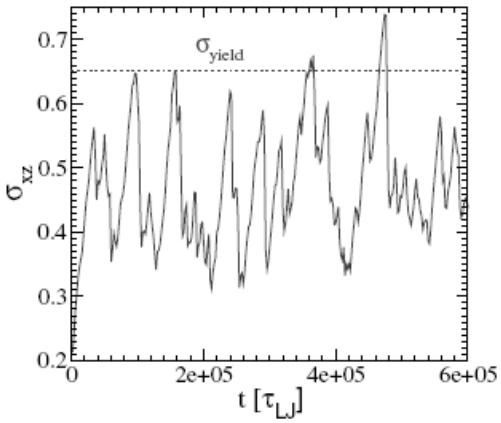

Figure 2.6: *Shear stress versus time for small global shear rates ($\dot{\Gamma} << \dot{\Gamma}_c$). The stress rises up to a value close to the yield stress and then suddenly drops to a value smaller than the one obtained in a homogeneous flow. Figure from Ref. [56].*

2.4 Other theories for shear banding and yielding

The shear banding phenomena has first been observed in various non colloidal complex fluids, like surfactant wormlike micelles, liquid crystals and lamellar surfactant systems which can roll into multilamellar vesicles ("onions"). These systems don't exhibit a glassy dynamics and their flow curve is not characterized by the presence of a yield stress. It shows instead a decreasing branch, which follows a region where the stress increases with the shear rate (Fig. 1.6). In a controlled shear experiment, bands characterized by different finite local shear rates may be observed when the stress falls in the interval where the flow curve is multivalued. While in glassy systems the difference between the bands is of dynamical nature, in these systems a structural phase transition occurs under flow and an ordered phase coexists with a disordered phase. Many theoretical models have been developed to describe the shear banding phenomenon in these systems, in particular for wormlike micelles [59, 60, 61]. The structural differences between the flowing phases is usually identified through an order parameter and the investigation of its coupling with the flow allow to obtain a selection criterion for the flow pattern and the resulting macroscopic rheological behavior.

For glassy systems, where a structural variable cannot be identified to distinguish the coexisting phases, exhaustive microscopical models are still

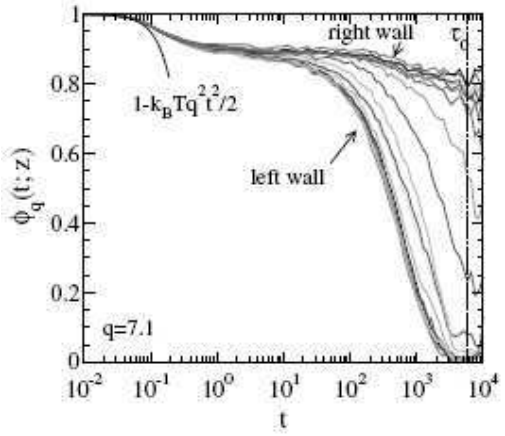

Figure 2.7: *Intermediate scattering function $\Phi_q(t;z)$ across the gap, when the velocity profile of the system shows a fluidized band next to the left wall and an unsheared band next to the right wall. Figure from Ref. [56].*

missing. A phenomenological simple model for heterogeneous flow in yield stress fluids has been proposed in Ref. [50], as described in 2.3.3. A numerical work, describing shear localization in a model glass [56], has also been presented in 2.3.4. An interesting work for non-glassy systems is the one presented by Dhont [62], where a gradient term is added to the standard constitutive relation in order to account for the rapid variation of the local shear rate at the interface between the flow bands. As a result, shear banding occurs in the fluid under controlled shear conditions, but the stationary state is not uniquely determined and depends on the initial perturbation applied to the system. A "quasi-thermodynamic" model proposed by Porte and coworkers [58] describes the shear banding phenomenon in phase separating fluids, but the same basic physical mechanism can be adapted to the banding originating in glassy materials. Section 2.4.1 will be devoted to the presentation of this model. A very simple phenomenological model, which we will present in (2.4.2), has been proposed by Coussot and coworkers [17] to describe the behavior of thixotropic, yielding fluids which they had investigated experimentally.

2.4.1 A "quasi-thermodynamic" model

In the microscopic model proposed by Porte and coworkers [58], the system is described in terms of an effective non-equilibrium potential F_s, defined over mesoscopic scales, that accounts for the free energy stored in a viscoelastic material under steady-shear conditions. A strain-like order parameter γ_s for the potential F_s is introduced in the model and describes the effective state of the medium averaged over mesoscopic scales. The description of the system through this order parameter is also adaptable to glassy systems, as no direct dependence on the structure of the system is present in the model. In steady state conditions, a generalized viscous constitutive equation yields: $\sigma = \eta(\gamma_s)\dot{\gamma}$ and the flow pattern depends on the shape of the potential $F_s(\gamma_s)$. If F_s is concave upwards at all γ_s, then the flow curve is monotonic. If, on the contrary, the concavity of F_s changes sign in some range of γ_s, then the flow curve is non monotonic, but its specific features depend on the viscous law characterizing the system.

In a shear thinning system ($d\eta/d\gamma_s < 0$), the flow curve exhibits a decreasing branch and the fluid will undergo an internal transition at a unique stress σ_t forming shear bands. This inhomogeneous flow regime is uniquely defined by the system of equations proposed in the model, which determines the local shear rates $\dot{\gamma}_1$ and $\dot{\gamma}_2$ in the two bands for a given global shear rate $\dot{\Gamma}$ (Fig. 1.6). The relative proportions x and $1-x$ of the high and low shear-rate bands is defined by the equation

$$x\dot{\gamma}_1 + (1-x)\dot{\gamma}_2 = \dot{\Gamma}$$

For a shear thickening system ($d\eta/d\gamma_s > 0$), the generic non-monotonic shear curve has the form shown in Fig. 2.8. The resulting flow behavior is completely different from the shear thinning case and shear banding is not observed. In a shear controlled experiment, below $\dot{\gamma}_1$ the lower branch is followed and the homogeneous flow is stable. At $\dot{\gamma}_1$ the stress σ_t is reached, germs of the viscous state nucleates at a shear rate $\dot{\gamma}_2$, but a stationary state is reached at point 3. Once above $\dot{\gamma}_1$, a stationary homogeneous flow is recovered on the upper branch. Thus, upon increasing the shear rate, a discontinuous jump from σ_t to σ_3 is expected for the measured stress as $\dot{\gamma}$ passes through $\dot{\gamma}_1$. A reentrant region in the flow curve with unstable solutions also resulted in the glassy models for shear thickening (2.3.1, 2.3.2), where an oscillating stress resulted under steady shear.

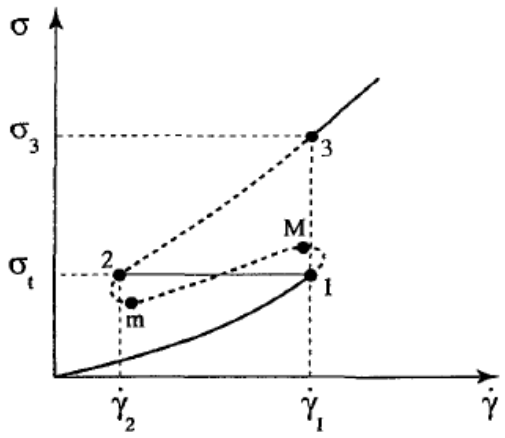

Figure 2.8: *Schematic representation of a non-monotonic flow curve for a shear thickening fluid. Figure from Ref. [58].*

2.4.2 A simple model for yielding fluids

The experimental results on the mechanical behavior of various glassy fluids, has suggested the simple phenomenological model for yielding fluids presented in Ref. [17]. At rest, the systems exhibited an aging behavior, while in response to an applied stress, the fluid showed a bifurcation in flow behavior that depended on its flow history. In particular, a time-dependent critical stress determined whether prolonged shearing would lead to a flow or non-flow condition in steady state. This critical stress is identifiable as a yield stress. The typical picture to describe yielding suspensions views a network of interactions between the particles extending over the entire sample. The structural rearrangements taking place during the aging evolution enhance the strength of the network interactions. The effect of the flow is to disperse particles and consequently to diminish the strength of the network. As usual, the rheological behavior of the system thus results from the competition between the aging process and the rejuvenating effect of the shear flow. In this framework, the authors suppose that the state of the material at a given time can be described by a single parameter λ, which represents, for instance, the degree of aggregation. For an aging system at rest, λ increases at a constant rate of $1/T_0$, being T_0 the characteristic time of the aging. The rate of decrease of λ under shear rejuvenation is assumed proportional to the shear rate. Therefore, the evolution of the λ parameter is described by the

equation

$$\frac{d\lambda}{dt} = \frac{1}{T_0} - \alpha\lambda\dot{\gamma}$$

where α is a system dependent constant. In the model, the viscosity of the system is a function only of the instantaneous state of the material: $\eta = \eta_0 f(\lambda)$, with f an increasing function of λ. A dimensionless shear stress $T = \sigma\alpha T_0/\eta_0$ is written as a function of a dimensionless shear rate $\Gamma = \alpha T_0\dot{\gamma}$ as $T = \Gamma f(1/\Gamma)$. For a function f that increases sufficiently rapidly, thus a viscosity increasing rapidly with λ, at small shear rates the flow curve turns out to be nonmonotonic. Under controlled shear rate, shear banding instability thus shows up below a critical shear rate Γ_0, while a homogeneous flow occurs over Γ_0. Under controlled stress, for such a choice of f, the fluid evolves either towards complete stoppage if the stress is smaller than a certain value T_c, or towards a steady flow otherwise. This critical stress depends on the previous flow history and can be expressed as a function of the initial state of the material λ_0. The more the system ages before stress application, the bigger will be λ_0 and T_c. The temporal evolution of the viscosity as predicted by the model under various levels of stress is reported in Fig. 2.9. For stresses larger than T_c the viscosity decreases and reaches a steady value, while for smaller stresses the viscosity increases at an increasing rate and tends towards infinity inducing flow stoppage, just as observed in the experiments which suggested this model [17]. However, the yield stress does not have a specific value as in ideal yield stress fluids. Indeed, it results from a bifurcation, at the critical stress $T_c(\lambda)$, between a drastic increase in the viscosity leading to flow stoppage and a shear rejuvenation leading to a steady state flow.

2.5 Shear thinning and shear thickening in non glassy colloidal suspensions

In non glassy, concentrated colloidal suspensions, a shear thinning behavior is observed at low shear stresses, while at high stresses a thickening regime, which may end up in a jamming transition, shows up. Actually, dimensional analysis implies that for a given value of the volume fraction, all monodisperse hard-sphere suspensions ought to show an onset of shear thickening, which is not always accessible experimentally. In particles with long-ranged

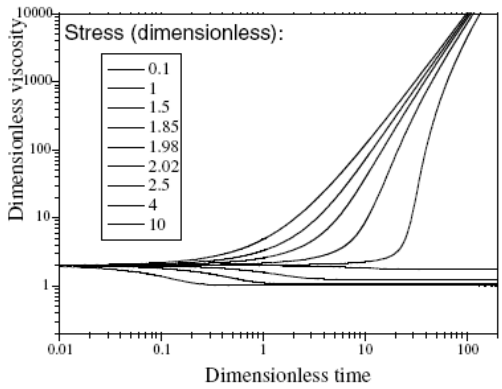

Figure 2.9: *Change in dimensionless viscosity (T/Γ) over dimensionless time for different dimensionless stress levels, according to the model proposed in Ref. [17]. The stress increases from top to bottom. Figure from Ref. [17].*

interactions, like charged colloids, a more sever shear thinning is expected, while the onset of the shear thickening regime and a following jamming transition are enhanced. A yield stress behavior may also be observed in these systems before the onset of the shear thinning regime. This complex rheology originates from a coupling between the flow and the microstructure, which has been investigated both on the theoretical and numerical ground. In the following, the microscopic theories for this phenomenology are reported (2.5.1), while in a later section (2.5.2) some numerical simulations and simple models, describing the onset of shear thickening and jamming, are presented.

2.5.1 Microscopic theories

Hoffman first formulated a theory for the structural origin of shear thickening in the framework of charged colloids [63]. He interpreted the onset of the shear thickening regime as an order-disorder transition. Concentrated, charged sphere colloids form an ordered, crystalline phase at rest, with a face centered cubic structure. Like in other fluids with an ordered phase, a yield stress behavior is observed when they are forced to flow. After yielding, the three-dimensionally ordered structure transforms into a layered structure that permits continuous deformation. In particular, planes of hexagonally close-packed spheres orthogonal to the flow gradient direction glides over each other inducing a shear thinning behavior. Hoffman argued that,

at some critical level of shear stress, a flow instability causes the particles to break out of their ordered layers, inducing the rise in viscosity that defines shear thickening. However, the breakup of the layered structure turned out be a necessary but insufficient condition for shear thickening.

Therefore, another model has been proposed to describe the onset of the shear thickening regime, which is the most often cited in recent literature. This theory involves the formation of hydrodynamic clustering and explains the increase of viscosity with the shear stress as due to the increasing dimension of these clusters [65]. This theory investigates the non-equilibrium microstructure through the Smoluchowski equation for the probability density of the particle positions, taking into account hydrodynamics, Brownian interactions and also an effective hard-sphere interparticle interaction. Only binary collisions between particles are considered. The parameter used in the model to quantify the effect of the flow on the system is the Peclet number Pe (see 2.2). At small Pe the viscosity exhibits a Newtonian behavior, followed by shear thinning when $Pe > 1$, while at larger Peclet numbers, $Pe > 10$, the system enters in the shear thickening regime. The shear thinning is due to the alinement of the particles under shear: convection starts to influence diffusion in this regime of Pe and the microstructure is distorted faster by the imposed flow than Brownian motion can restore isotropy. In this regime, the dominant transport mechanism is still Brownian motion, which leads to a positive value of the first normal stress difference. Shear thickening is instead due to the formation of hydrodynamic clusters and the state of order of the particles is not responsible for it as in the model proposed by Hoffman [66]. At high Pe, hydrodynamic interactions dominate, as a result the first normal stress difference changes from positive to negative values. Moreover, the pair distribution function $g(r)$ is found to be asymmetric, with an excess of particles in the compressional axis. The pair-distribution function at contact in the flow gradient plane, calculated for hard spheres with or without hydrodynamics interactions, is plotted in Fig. 2.10 as a function of θ, the angle from the flow direction, and Pe. In the absence of hydrodynamic interactions, there is no reduction of the mobility when two particles approach one another and particle density in a boundary layer in the compressive region of the flow accumulates rapidly with increasing Pe. Focusing on a reference particle, this acts indeed as an obstruction to particles being advected from upstream, while downstream there is no obstruction to transport and the extensional region is depleted of particles at large Pe. The inset of the figure demonstrates that growth of the boundary-layer scales linearly with

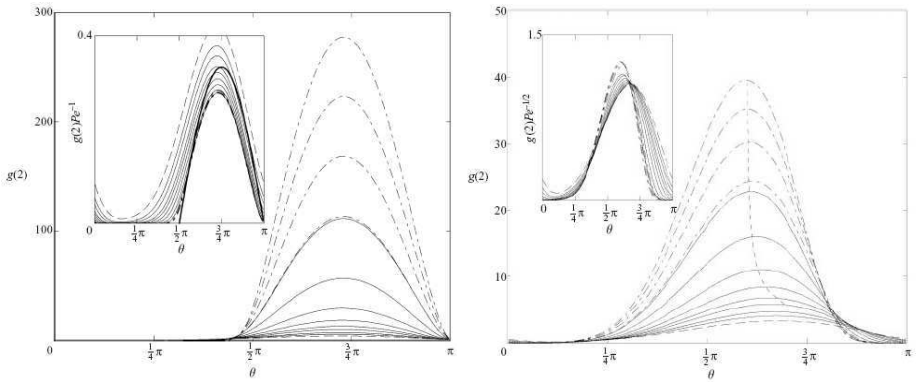

Figure 2.10: *Pair distribution function under flow at contact ($r = 2$) in the flow gradient plane as a function of θ, and Pe. From bottom to top: Pe =10, 15, 20, 30, 40, 60, 100, 200, 400, 600, 800, 1000. The left graphics is obtained from the Smoluchoski equation for hard spheres in the absence of hydrodynamics interactions, while the right one results from considering hydrodynamics interactions. The inset shows the same results scaled by Pe (left plot) or $Pe^{1/2}$ (right plot). The figures have been taken from Ref. [67].*

Pe. In the presence of hydrodynamic interaction, the detailed structure of the boundary layer changes for the lubrication effect of hydrodynamic forces. The squeezing together of two particles in the compressional region is indeed resisted by the expulsion of solvent from the narrow gap separating them and so is the pulling apart of the pair in the extensional region resisted by the replenishment of solvent in the growing gap. The former action tends to decrease the contact density in the compressional region, while the latter creates a finite contact density in the extensional region. Now the growth of the boundary layer scales as $Pe^{1/2}$ and the weaker accumulation of particle density in the boundary layer is compensated by a concomitant increase of the boundary layer thickness. In the case of hard spheres subject only to hydrodynamic interactions, Brownian motion renders the contact value of g finite. When excluded volume interactions are considered, the boundary layer structure changes and is seen to separate from particle contact. Shear thickening can thus be understood from this boundary layer analysis: the hydrodynamic contribution to the stress from the boundary layer shear thickens as the layer thins and the particles are pushed closer to contact with increasing Pe. The above analysis at the level of two particles can explain

the onset of shear thickening in dilute suspensions, but the treatment can also be extended to concentrated suspensions [68], where the same boundary layer structure is obtained.

2.5.2 Phenomenological models and numerical simulations

The microscopic theory developed by Brady and coworkers have inspired many numerical works or theoretical models investigating the shear-induced formation of hydrodynamic clusters in the compression axis [69, 71, 72].

A model of colloidal spheres interacting via shear, squeeze and rotation lubrication interactions has been simulated by Ball and Melrose [69] and the cluster formation phenomenon results. In particular, they investigate the effect of hydrodynamic and Brownian interactions on the cluster formation. In the absence of Brownian motion, the flow is found to be blocked by the formation of particle clusters, within which catastrophically narrow gaps exist between neighbors. The spacing between the particles in these clusters gets smaller and smaller as the shear stress applied to the system increases: the authors find indeed that the probability of having a percolating cluster with a given inter-particle spacing saturates when the applied stress increases. This gap narrowing in the clusters is referred to as a breakdown of lubrication. The inclusion of a surface interaction or Brownian motion, having a repulsive effect, can prevent this unphysical result. However, for high enough shear rates very narrow gaps again may form in the clusters, while jamming is not observed in this Brownian case.

Jamming transition is observed instead in a simple lattice model in two dimensions studied by O'Loan and coworkers [71]. The model accounts for the formation of clusters of particles under an imposed shear flow, which fragment stochastically. The size distribution of these shear-induced clusters shows a power law behavior and a hysteresis is found in the evolution of their average size as a function of the shear rate. When clusters spanning the entire system along the compression axis form, the system jams and in this regime the average size of the clusters is found to increase roughly linearly with increasing shear rate. An interesting picture of the jamming process in a colloidal suspension is also given by [70]. A kinetic clustering model, developed by Farr and coworkers [72], also predicts a jamming transition. The theory is based on the shear induced growth of rigid rodlike clusters down the compression axis and, compared to the pair theory of Brady and coworkers, have the advantage of considering many body instabilities. In the

model, rods grow by aggregation with other rods as they rotate in the flow. As a result, a rapid collapse is found and a jamming transition at a volume fraction below close packing is defined. It takes place when a rod cluster, first forming in the compression axis, grows to infinite size before it tumble, by passing $\theta = \pi/2$ and entering in the region of extensional flow.

Finally, as the shear thickening phenomenon is governed by the shear stress, efforts have also been devoted to the investigation of the critical stress value for the onset of this regime, in dependence to the kind of interparticle interactions. Scaling arguments have been used to determine the critical stress as a function of particle size and volume fraction for hard spheres or charged particles [73]. This is obtained by balancing the dominant repulsive force responsible for the stability of the suspension with the hydrodynamic force. When the ratio between this two forces is close to one, the onset of the shear thickening regime takes place. When strong dissipative surface forces are considered instead, shear thickening is enhanced [74]. Indeed, the main consequence of the friction between particle surface is to induce an asymmetry in the interparticle interactions. This asymmetry at contact facilitates the formation of the hydrodynamic clusters and the onset of the shear thickening regime takes place at smaller volume fraction and at smaller shear stress.

Part II

Methods and materials

CHAPTER 3

Dynamics investigation through light scattering techniques

When a colloidal suspension is illuminated by coherent light, the far field pattern of scattered light comprises a grainy diffraction pattern, where light intensity is spatially correlated over an area called speckle (Fig. 3.1 a). At some points in the far field, the phases of the light scattered by individual particles are such that the individual fields interfere largely constructively to give a large intensity; at other points, about one speckle size far, destructive interference leads to a small intensity. Motion of the scatterers leads to a significant change in the phase of the scattered light, thus the speckle pattern fluctuates from one random configuration to another. In particular, the intensity scattered to a point in the far field fluctuates randomly in time. Information on the motions of the particles is encoded in this random signal: at the simplest level, the faster the particles move, the more rapidly the intensity fluctuates. Experimentally, information on the system dynamics is extracted from the fluctuating scattered intensity $I(t)$, by computing its time correlation function:

$$G(t) = \langle I(0)I(t)\rangle \equiv \lim_{T\to\infty} \frac{1}{T}\int_0^T dt' I(t')I(t'+t) \tag{3.1}$$

As can be seen from this definition, the intensity correlation function compares the signal $I(t')$ with a delayed version $I(t'+t)$ of itself, for all starting

times t' and for a range of delay times t. In order to have a high signal to noise ratio, the acquisition time T in the experiment must be much larger than the typical fluctuation time τ_c of the intensity: $T \gg \tau_c$. This relation is formalized in equation 3.1 through the $\lim_{T\to\infty}$. When the system dynamics are non-stationary on a timescale τ_e larger than the acquisition time ($\tau_e \gg T$), the correlation function depends on the time t_0 when the measurement starts:

$$G = G(t_0, t) = \langle I(t_0)I(t_0 + t)\rangle \tag{3.2}$$

We want to remark here that the systems that we investigate in this work may be non stationary: in the following, we will thus refer the more general equation (3.2) for the correlation function. At zero delay ($t = 0$), equation (3.2) reduces to $\langle I^2\rangle$ (we consider the case where the scattered intensity is stationary but the system dynamics are not). For delay times much greater than the typical fluctuation time τ_c of the intensity (Fig. 3.1 b), fluctuations in $I(t_0)$ and $I(t_0+t)$ are uncorrelated so that the correlation function reduces to $\langle I\rangle^2$. Thus, the intensity correlation function decays from the mean-square intensity at small delay times to the square of the mean at long times. The characteristic time τ_c of this decay is a measure of the typical fluctuation time of the scattered intensity (Fig. 3.1 c) and quantifies the timescale of the dynamics of the scattering particles.

Typically, in a light scattering experiment, laser polarized radiation hits the sample and a detector, set in the far field, measures the intensity $I(t)$ of the scattered radiation. A classical (non-quantistic) approach to light scattering theory is valid when the laser wavelength is much larger than the length scale of the scattering particles in the medium. Thus, the incident beam can be schematized by a plane-wave, monochromatic radiation of wavelength λ (inside the medium) and frequency ω:

$$E_1(\boldsymbol{r}, t) \equiv E_0 \exp[i(\boldsymbol{k}_i \cdot \boldsymbol{r} - \omega t)] \tag{3.3}$$

where the incident electric vector E_0 is usually polarized perpendicular to the scattering plane and the propagation vector $\boldsymbol{k}_i$ has magnitude $|\boldsymbol{k}_i| = k_i = 2\pi/\lambda$. The scattering event usually implies only a very small change in frequency and the process can be assumed "quasielastic". Thus, the propagation vector $\boldsymbol{k}_s$ of the light after one scattering event also has magnitude $2\pi/\lambda$. When light weakly interacts with the sample so that one can consider only single scattering events, Light Scattering theory is used to describe the

system and the corresponding technique is called Dynamic Light Scattering (DLS). On the other hand, Diffusive Wave Spectroscopy theory (DWS) has been developed to account for highly multiple scattering media.

DLS and DWS are the basic techniques that we have been using to investigate microscopically the rheological behavior of some colloidal systems. In the following, the basic theories underlying these two techniques are presented.

3.1 Dynamic light scattering

In a dynamic light scattering experiment, most photons pass through the sample undeviated and a few are scattered once. A detector set in the far field at scattering angle θ fixes the direction of the scattered light, with propagating vector $\boldsymbol{k}_s$. The intersection between the incident and scattered beam is called scattering volume. The difference between the propagation vectors of the scattered and incident beam defines the scattering vector $\boldsymbol{q}$

$$\boldsymbol{q} \equiv \boldsymbol{k}_s - \boldsymbol{k}_i \tag{3.4}$$

whose modulus can be expressed as a function of the scattering angle and the radiation wavelength as $q = 4\pi/\lambda \sin(\theta/2)$. In the so called homodyne method, the time correlation function of the scattered intensity $I(\boldsymbol{q}, t) = |E(\boldsymbol{q}, t)|^2$ is measured. When normalized, it is defined as

$$g^{(2)}(\boldsymbol{q}, t_0, t) \equiv \frac{\langle I(\boldsymbol{q}, t_0) I(\boldsymbol{q}, t_0 + t) \rangle}{\langle I(\boldsymbol{q}) \rangle^2} \tag{3.5}$$

In the heterodyne method, a small portion of the unscattered laser light (called local oscillator) is mixed with the scattered light. The sum of these two interfering fields $E_{lo} + E$ (with E_{lo} for the local oscillator and E for the scattered light) hits the detector surface and the time correlation function of the collected intensity $I_e(\boldsymbol{q}, t) = |E_{lo}(t) + E(\boldsymbol{q}, t)|^2$ is computed. By proper choice of the experimental conditions and providing that the amplitude of the local oscillator is much larger than the amplitude of the scattered field, this correlation function is:

$$\langle I_e(\boldsymbol{q}, t_0) I_e(\boldsymbol{q}, t_0 + t) \rangle \propto I_{lo}^2 + 2 I_{lo} Re[\langle E^*(\boldsymbol{q}, t_0) E(\boldsymbol{q}, t_0 + t) \rangle] \tag{3.6}$$

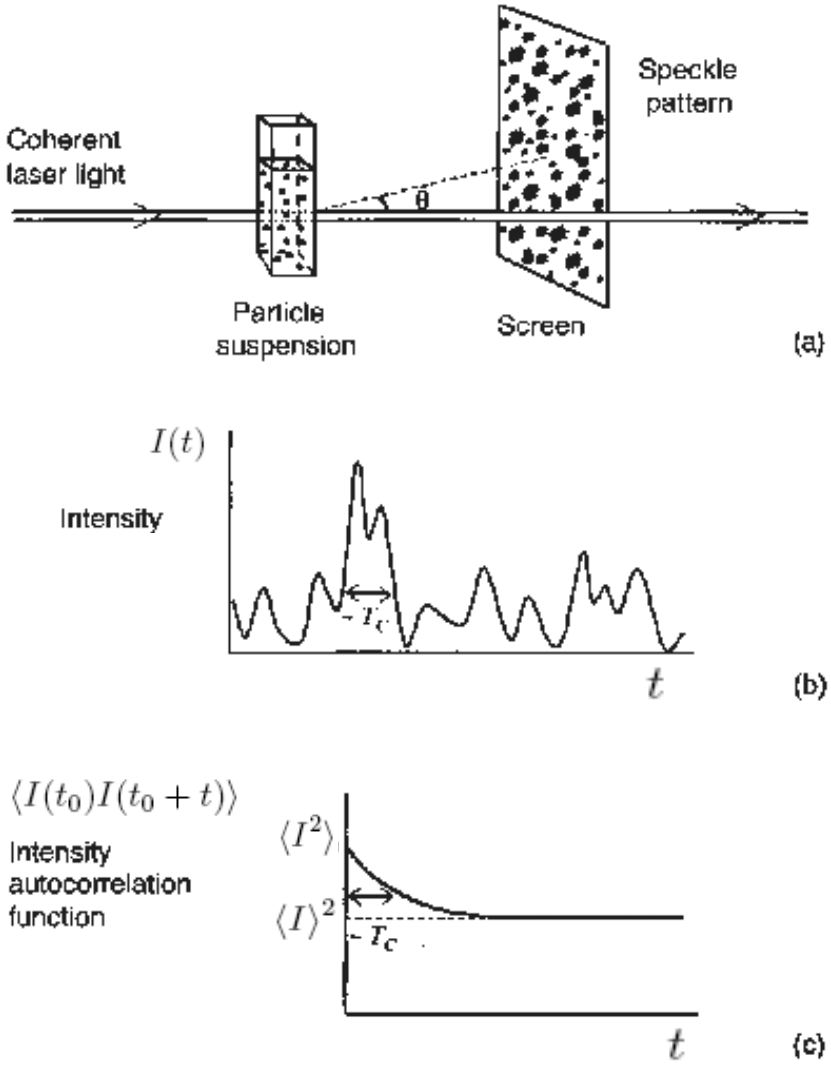

Figure 3.1: *a) Coherent light scattered by a random medium, such as a suspension of colloidal particles, give rise to a speckle pattern in the far field. b) The fluctuating intensity observed at a detector with the size of about one speckle. c) The time-dependent part of the correlation function decays with a time constant τ_c, corresponding to the typical timescale of the particle dynamics. Figure from [75].*

where $I_{lo} = |E_{lo}|^2$. Therefore, the real part of the scattered field correlation function can be measured through the heterodyne method. When normalized, the field correlation function is defined as:

$$g^{(1)}(\boldsymbol{q}, t_0, t) \equiv \frac{\langle E^*(\boldsymbol{q}, t_0) E(\boldsymbol{q}, t_0 + t) \rangle}{I(\boldsymbol{q})} \tag{3.7}$$

When the dynamics of the sample are stationary, $g^{(2)}(\boldsymbol{q}, t_0, t) = g^{(2)}(\boldsymbol{q}, t)$ and $g^{(1)}(\boldsymbol{q}, t_0, t) = g^{(1)}(\boldsymbol{q}, t)$.

In the following, we will elucidate the basic principles of dynamic light scattering theory, in order to interpret the variables measured in a DLS experiment and predict their behavior. Light scattering theory is introduced in 3.1.1, while the effect of a shear flow on light scattering is discussed in 3.1.2.

3.1.1 Light scattering theory

In the single scattering regime, the amplitude of the scattered electric field in the far field can be calculated through Maxwell's equations. The basic picture underlying light scattering theory [8], holding when the wavelength λ is much larger than interatomic distances, views the incident electric field inducing an oscillating polarization in the sample: charges are so accelerated in the medium and irradiate light. At a mesoscopic level, the interaction between the medium and light is represented by the local fluctuations of the dielectric constant in the medium. These fluctuations are induced by the motion of the molecules and are responsible for light scattered in directions different from the incident one. The form, dimensions and interactions of the molecules in the sample determine the properties of the scattered light (its polarization, intensity, frequency shift and angular distribution).

The fundamental variable used in light scattering theory is the dielectric constant fluctuation tensor. Calling $\varepsilon(\boldsymbol{r}, t)$ the dielectric constant tensor at position $\boldsymbol{r}$ in the scattering volume V, its fluctuations are $\delta\varepsilon(\boldsymbol{r}, t) = \varepsilon(\boldsymbol{r}, t) - \varepsilon_0 I$, where I is the unity tensor and ε_0 is the average dielectric constant in the medium. The spatial Fourier transform of $\delta\varepsilon(\boldsymbol{r}, t)$ is defined as

$$\delta\varepsilon(\boldsymbol{q}, t) = \int_V \exp(i\boldsymbol{q} \cdot \boldsymbol{r}) \delta\varepsilon(\boldsymbol{r}, t) d^3 r \tag{3.8}$$

The main result of light scattering theory is to express the scattered electric

field $E_s(\boldsymbol{R}, t)$ at position $\boldsymbol{R}$ in the far field as a function of $\delta\varepsilon(\boldsymbol{q}, t)$ [8]:

$$E_s(\boldsymbol{R}, t) = -\frac{\boldsymbol{k}_s E_0}{4\pi\varepsilon_0 R} \exp(i\boldsymbol{k}_s\boldsymbol{R} - i\omega t)\delta\varepsilon_{if}(\boldsymbol{q}, t) \tag{3.9}$$

where $\delta\varepsilon_{if}(\boldsymbol{q}, t) \equiv \boldsymbol{n}_f \cdot \delta\varepsilon(\boldsymbol{q}, t) \cdot \boldsymbol{n}_i$ is the component of the dielectric constant fluctuation tensor along the initial and final polarization directions $\boldsymbol{n}_i$ and $\boldsymbol{n}_f$. It is now evident that light scattering is induced by fluctuations of the dielectric constant $\varepsilon(\boldsymbol{r}, t)$ in the medium in $\boldsymbol{q}$-space: if $\varepsilon(\boldsymbol{r}, t)$ is homogeneous, there would be no scattered light in other than the forward direction.

We now specialize to the case of samples which are isotropic in average (as are the systems we use in our experiments), so that averaged quantities such as $g^{(1)}(\boldsymbol{q}, t_0, t)$ depend only on the modulus q of the scattering vector. From equation 3.9, the following relations hold for the normalized electric field and intensity correlation function:

$$g^{(1)}(q, t_0, t) = \frac{\langle \delta\varepsilon^*_{if}(q, t_0)\delta\varepsilon_{if}(q, t_0 + t)\rangle}{\langle \delta\varepsilon_{if}(q)\rangle^2} \tag{3.10}$$

$$g^{(2)}(q, t_0, t) = \frac{\langle |\delta\varepsilon_{if}(q, t_0)|^2 |\delta\varepsilon_{if}(q, t_0 + t)|^2\rangle}{\langle |\delta\varepsilon_{if}(q)|^2\rangle^2} \tag{3.11}$$

Dielectric constant fluctuations, which are defined when the wavelength λ is much larger than interatomic distances, can be expressed as a function of the density fluctuations in the medium: $\delta\varepsilon_{if}(q, t_0, t) \propto \delta\rho(q, t_0, t)$. Detecting $g^{(1)}(q, t_0, t)$ then represents a direct measurement of the density density autocorrelation function (defined in equation 1.2), which is the variable used in the theoretical and numerical works to investigate the dynamics in fluid systems (as evidenced in 4.10):

$$g^{(1)}(q, t_0, t) = F(q, t_0, t) \tag{3.12}$$

For this reason, the field correlation function $g^{(1)}(q, t_0, t)$ is frequently called the "intermediate scattering function" $F^M(q, t_0, t) \equiv g^{(1)}(q, t_0, t)$.

In a DLS experiment, the intermediate scattering function is usually the quantity of interest and, under certain conditions, it can be obtained from the measured intensity correlation function $g^{(2)}(q, t_0, t)$. When the number of particles in the scattering volume is large, the scattered field $E(\boldsymbol{q}, t)$ is a complex random variable having a Gaussian probability distribution. The

intensity $I(\boldsymbol{q}, t)$, measured at a point in the far field, is then distributed exponentially. In this case, the speckle in the random diffraction pattern is known as "Gaussian speckle". At a point in the pattern there is small probability of finding a very high instantaneous intensity and the most likely value is very small. The correlation function of a complex Gaussian variable has factorization properties which results in the following relation for $g^{(1)}(q, t_0, t)$ and $g^{(2)}(q, t_0, t)$ [8]:

$$g^{(2)}(q, t_0, t) = 1 + |g^{(1)}(q, t_0, t)|^2 \tag{3.13}$$

which is called Siegert relation and can be easily derived, for example, for a dilute suspension of identical spheres. However, this formula is applicable to any fluid system for which the range of spatial correlations is much smaller than the linear dimension of the scattering volume. Under these conditions, the scattering volume contains a large number of correlation volumes (*i.e.* volumes within which particle positions are correlated), and the correlation volumes may take the role of the independent particles [75]. However, the Siegert relation is obtained by considering the amplitude of the electric field scattered to a *point* in the far field. In reality, a detector has a non-zero active area and therefore sees different scattered fields at different points on its surface. Then it can be shown that equation (3.13) is modified to

$$g^{(2)}(q, t_0, t) = 1 + B|g^{(1)}q, t_0, t)|^2 \tag{3.14}$$

where the factor B represents the degree of spatial coherence of the scattered light over the detector and is determined by the ratio of the detector area to the area of one speckle. In practice, with a classical two-pinhole setup for collection, the detector aperture is usually chosen to accept about four speckles, which give the maximum value for $B = 0.8$ [101]. The intermediate scattering function can thus be derived by inverting equation (3.14).

The size of a speckle in the far field diffraction pattern can be estimated from the size of the scattering volume. One should calculate how much two points in the far field must be separated in order to have the scattered electric fields at the two points uncorrelated. If the two points are defined by scattering vectors $\boldsymbol{q}_1$ and $\boldsymbol{q}_2$, with $\Delta\boldsymbol{q} \equiv \boldsymbol{q}_2 - \boldsymbol{q}_1$, the following relation holds [75]:

$$\langle E(\boldsymbol{q}_1, t)E^*(\boldsymbol{q}_2, t)\rangle = |E_0|^2 \sum_{j=1}^{N} \langle \exp[i\Delta\boldsymbol{q} \cdot \boldsymbol{r}_j(t)]\rangle$$

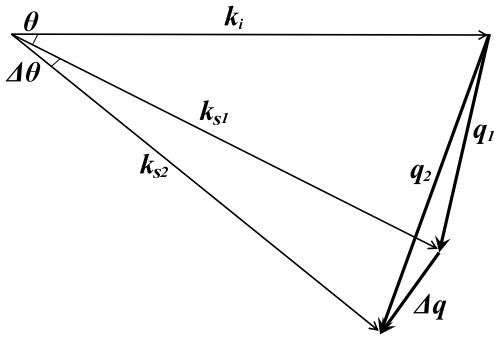

Figure 3.2: *Propagation and scattering vectors describing light scattered to two different points. When $\Delta\theta$ is small, fluctuations in the two fields are correlated; when $\Delta\theta$ is large enough for the points to be in different speckles, the fluctuations are uncorrelated.*

where the position $\boldsymbol{r}_j(t)$ of the particle can lie anywhere in the scattering volume. Thus, an estimate of the value of $\Delta\boldsymbol{q}$ at which correlation between the two fields is lost is given by $\Delta\boldsymbol{q}L_v \approx 2\pi$, where L_v is the dimension of the scattering volume parallel to $\Delta\boldsymbol{q}$ (perpendicular to the direction of the scattering). From Fig. 3.2, it is evident that the angle at the scattering volume subtended by one speckle is

$$\Delta\theta = \Delta q/k_s \approx \lambda/L_v$$

We will now proceed with the explicit expressions for the intermediate scattering function in the specific case of a sample containing discrete scattering objects suspended in a liquid [75].

Discrete scatterers

For a colloidal system, the properties of the fluctuating scattered light can be investigated by considering the simple situation of discrete spherical scatterers. Typically, the colloidal particles in solution scatter much more than the solvent molecules, as they have an enormously larger polarizability. Besides, their dynamics is much slower and their motion can be considered independent on the motion of the solution molecules. The superposition of the electric fields scattered in the direction of $\boldsymbol{k}_s$ by all the colloidal particles contained in the scattering volume represents the electric field collected by the detector. The degrees of freedom accounting for the solvent can instead

be integrated, resulting in a dependence of the scattered field on the solvent dielectric constant. For discrete spherical scatterers, it can be shown that the electric field at scattering vector $\boldsymbol{q}$ can be expressed as (as DLS deals with normalized quantities, we omit the electric field amplitude E_0):

$$E(\boldsymbol{q}, t) = \sum_j \exp[-i\boldsymbol{q} \cdot \boldsymbol{r}_j(t)] \tag{3.15}$$

where $\boldsymbol{r}_j(t)$ is the position of the center of mass of particle j at time t (relative to an arbitrary origin). Due to motion of the particles, positions $\boldsymbol{r}_j(t)$ and phase angles $\{\boldsymbol{q} \cdot \boldsymbol{r}_j(t)\}$ evolve randomly with time, thus the total scattered field itself fluctuates. For small time differences t, the phase angles have not changed much and the total scattered field at time $t_0 + t$, $E(\boldsymbol{q}, t_0 + t)$, is still correlated to $E(\boldsymbol{q}, t_0)$. On the other hand, over times t such that a particle moves a distance $|\boldsymbol{r}_j(t_0 + t) - \boldsymbol{r}_j(t_0)| \approx 2\pi/|\boldsymbol{q}|$, the phase angles change by $\sim 2\pi$ and the total scattered field becomes totally uncorrelated. If the suspension is dilute and particle positions are uncorrelated, $g^{(1)}(q, t_0, t)$ can be expressed as

$$g^{(1)}(q, t_0, t) = \langle \exp(i\boldsymbol{q} \cdot \Delta\boldsymbol{r}(t_0, t)) \rangle \tag{3.16}$$

where $\Delta\boldsymbol{r}(t_0, t) \equiv \boldsymbol{r}(t_0 + t) - \boldsymbol{r}(t_0)$ are considered the same for each particle (identical particles). Reminding that $q = 2\pi/\lambda$, the correlation function thus decays appreciably when $\Delta r \approx \lambda$.

A typical case of dynamic light scattering experiment occurs when colloidal particle motion is dominated by Brownian diffusion and the dynamics are stationary. In general, when the difference $\Delta\boldsymbol{r}(t)$ in equation 3.16 is a Gaussian variable, then $g^{(1)}(q, t)$ can be expressed as

$$g^{(1)}(q, t) = \exp[-q^2 \langle \Delta r^2(t) \rangle / 6] \tag{3.17}$$

For simple diffusion, $\langle \Delta r^2(t) \rangle = 6Dt$, where D is the particle diffusion coefficient, thus we obtain

$$g^{(1)}(q, t) = \exp[-q^2 Dt] \tag{3.18}$$

In this simple case, the autocorrelation function decays exponentially with a time constant $\tau = (Dq^2)^{-1}$. As the diffusion coefficient is linearly related to the particle size, this result is used in a widespread application of DLS: measuring particle size in dilute suspensions.

3.1.2 Light scattered from a system under shear

When the particles in the scattering volume flow with a drag velocity, light scattering is strongly affected whenever Brownian motion is dominated by these drift dynamics. When scattering particles are moving at velocity $\boldsymbol{v}$, the frequency of the scattered electric field is Doppler shifted by $\omega = \boldsymbol{q} \cdot \boldsymbol{v}$, where $\boldsymbol{q}$ is the scattering vector. In the heterodyne method, this results in an oscillating behavior of the measured correlation function at frequency ω. Local velocimetry measurements can thus be performed through this technique and the detailed velocity profile in a stationary flowing fluid can be obtained by varying the position of the scattering volume within the sample. On the other hand, in the homodyne method, the effects of the drift velocity are decorrelation terms of geometrical nature in the measured correlation function. Through these terms, local velocimetry measurements may thus be performed also through the homodyne method. However, in a colloidal suspension under shear, this decay of the correlation function due to flow usually takes place at timescales shorter than the structural relaxation time. As a consequence, the timescale characterizing the slow dynamics of such systems is no longer accessible during the flow. This represents the strongest limit to dynamics investigation in complex systems under shear. Light Scattering Echo experiments may overcome this problem [4, 97] in the case of an oscillating shear rate. DLS experiments on colloidal systems under shear are not reported in the literature, while in DWS experiments [6, 7] (where the decorrelation effects are present: see 3.2), the system dynamics is investigated by stopping the flow for a short time to allow the measurement. In our DLS experiments, we have used the same procedure. This is a delicate point, as some authors [36] state that the effect of shear rate on the structural dynamics holds only during the flow and vanishes soon after shear cessation. This problem will be discussed in 5.2, referring to the experiment in which we investigated by DLS the shear effect on the structural dynamics of a glassy system. In the following, the detailed expressions for the correlation functions in heterodyne and homodyne DLS are retrieved.

Derivation of the intermediate scattering function

In a shear flow, the physical properties are no longer invariant under spatial translations. However, a new translational invariance follows from the fact that a shift of the origin of the reference frame (Fig. 3.3) by l along the x-axis is equivalent to a new reference frame moving with a velocity $-l\dot{\gamma}\boldsymbol{e}_y$ [81, 82].

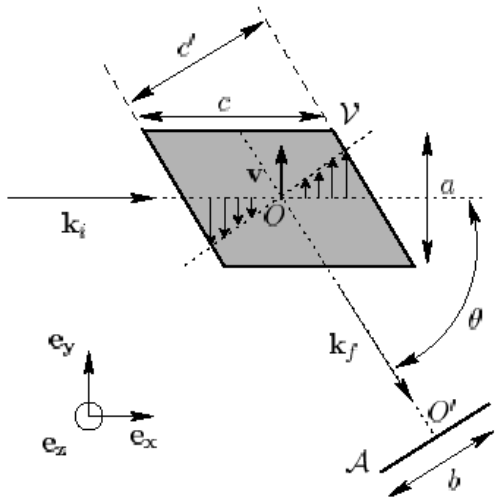

Figure 3.3: *Geometry of the scattering volume in a shear flow. V stands for the scattering volume and A for the photocathode area. Figure from [79].*

This implies that, in homogeneous stationary states, the time correlation function of a density variable $F(\boldsymbol{r}, \boldsymbol{r}', t_0, t) = \langle \rho(\boldsymbol{r}, t_0)\rho(\boldsymbol{r}', t_0 + t)\rangle$ may be written as

$$F(\boldsymbol{r}, \boldsymbol{r}', t_0, t) = F(\boldsymbol{r}' - \boldsymbol{r} - (\boldsymbol{v} + \dot{\gamma}(\boldsymbol{r}' \cdot \boldsymbol{e}_x)\boldsymbol{e}_y)(t - t_0), t - t_0) \tag{3.19}$$

In the Fourier space, $F(\boldsymbol{q}, t) = \int d^3\boldsymbol{r} \exp(i\boldsymbol{k} \cdot \boldsymbol{r})\langle \rho(\boldsymbol{r}, t)\rho(0, 0)\rangle$ and this invariance implies that

$$F(\boldsymbol{q}, \boldsymbol{k}, t_0, t) = (2\pi)^3\delta(\boldsymbol{k} - \boldsymbol{q} - \dot{\gamma}(t - t_0)(\boldsymbol{q} \cdot \boldsymbol{e}_y)\boldsymbol{e}_x)F(\boldsymbol{q}, t - t_0) \tag{3.20}$$

The Dirac delta function can be explained by noticing that a plane wave composition fluctuation ($\propto \exp(i\boldsymbol{q} \cdot \boldsymbol{r})$ at $t = 0$) changes in time into a plane wave with a time dependent wave vector

$$\boldsymbol{q}'(t - t_0) = \boldsymbol{q} + \dot{\gamma}(t - t_0)(\boldsymbol{q} \cdot \boldsymbol{e}_y)\boldsymbol{e}_x \tag{3.21}$$

As a consequence, the intermediate scattering function (generalized for two different wave vectors)

$$g^{(1)}(\boldsymbol{q}, \boldsymbol{k}, t_0, t) = \langle E^*(\boldsymbol{q}, t_0)E(\boldsymbol{k}, t_0 + t)\rangle$$

will be non zero only when $\boldsymbol{k} = \boldsymbol{q}'(t - t_0)$. In fact, this is strictly true only for an infinite scattering volume V, while in practice, V corresponds to the finite intersection of the incident and scattering beam. Approximating V as the intersection between two infinite cylinders, its dimensions are $a \times a \times c$ (Fig. 3.3). Thus, the scattering vector $\boldsymbol{q}$ is only defined up to a precision $\delta q_x = \pm 2\pi/c$ and $\delta q_y = \delta q_z = \pm 2\pi/a$. Let's consider that one coherence area of the speckle pattern is collected by the detector. The condition on the scattering vectors ($\boldsymbol{k} = \boldsymbol{q}'(t - t_0)$) results in the motion of coherence areas in the x-direction. This leads to decorrelation in the intermediate scattering function when $|\boldsymbol{k} - \boldsymbol{q}| > \delta q_x$. From equation 3.21, the time characterizing this decay of the correlation function, called the advection time, is

$$\tau_a = 2\pi/(c\dot{\gamma} q_y) \tag{3.22}$$

Another decorrelation term has to be considered. As soon as a particle goes out from the scattering volume, it will no more contribute to the intermediate scattering function (as it is evident from equation 3.15. Therefore, the correlation function will decay on a timescale τ_t, which is the transit time of the particles across the scattering volume. This time is

$$\tau_t \approx a/v \tag{3.23}$$

where v is the mean velocity in the scattering volume. The values of τ_t and τ_a have to be calculated according to the properties of the experimental set-up. However, they are usually smaller than the timescale characterizing the structural dynamics of the system under shear, which therefore cannot be accessed.

Considering these two "artificial" decorrelation terms, we can calculate the intermediate scattering function under a shear flow with negligible Brownian displacement. For the phase in equation 3.16 expressing $g^{(1)}$, we can write (see Fig. 3.3):

$$\boldsymbol{r}(t_0 + t) - \boldsymbol{r}(t_0) = \boldsymbol{v}(t - t_0) + \dot{\gamma} x \boldsymbol{e}_y (t - t_0) \tag{3.24}$$

Under stationary conditions, the intermediate scattering function can thus be expressed as

$$g^{(1)}(t) = \exp(i\boldsymbol{q} \cdot \boldsymbol{v}) F(t) \tag{3.25}$$

where

$$F(t) = \int_V \exp(i\dot{\gamma} x q_y t) d^3\boldsymbol{r}$$

This function decays to zero on a timescale $\tau \sim min\{\tau_a, \tau_t\}$.

In the homodyne method, where the modulus of the field correlation function is measured (see equation 3.13), the phase factor disappears and one measures:

$$g^{(2)}(t) \propto |F(t)|^2$$

If the geometry of the experiment is chosen in order to have $\tau_t > \tau_a$, the decay of $F(t)$ will be dominated by the transit time. In this case, the homodyne method can be used to estimate the local velocity in the scattering volume.

In the heterodyne method, the measured correlation function is determined by the real part of the intermediate scattering function (see equation 3.6):

$$\langle I_e(\boldsymbol{q}, 0) I_e(\boldsymbol{q}, t)\rangle \propto Re[\langle E^*(\boldsymbol{q}, 0) E(\boldsymbol{q}, t)\rangle] = \cos(\boldsymbol{q} \cdot \boldsymbol{v}t) F(t) \tag{3.26}$$

The information about the velocity $\boldsymbol{v}$ is contained in the phase of the scattering field. For this reason, the interference between the scattered field and the local oscillator allows direct access to this velocity, while in the homodyne method this information is lost. The correlation function measured in the heterodyne method then oscillates periodically at frequency $\omega = \boldsymbol{q} \cdot \boldsymbol{v}$. Knowing the scattering vector $\boldsymbol{q}$, the velocity in the scattering volume can thus be measured with high resolution.

3.2 Diffusive wave spectroscopy

In traditional DLS, the characteristic decay time of the intermediate scattering function is related to the dynamics of the medium through the length scale set by the inverse scattering wave vector $\boldsymbol{q}^{-1}$. Knowledge of the $\boldsymbol{q}$ vector is thus required in DLS to interpret the decay time of $g^{(2)}(q, t_0, t)$. This strictly limits its application to the single scattering regime. In the entirely opposite limit, when very high multiple scattering occurs in the medium, DWS approaches the problem of interpreting the scattered intensity correlation function. In this regime, in which the sample has a "milky" appearance, the propagation of light can be treated within the diffusion approximation. Each photon is scattered a large number of times and its path can be described as a random walk. As for conventional DLS, the decay of the measured correlation function results from a change in phase of the scattered field by $\approx 2\pi$. However, as it is the total path length of the light through the sample that

must change by approximately one wavelength to decorrelate the scattered field, each scatterer need to move only a small fraction of wavelength. Therefore, on a qualitative ground, DWS probes particle motion on length scales much shorter than in traditional DLS.

In the multiple scattering limit, there are two length scales that characterize light scattering and transport: the mean free path l between scattering events and the transport mean free path l^*, which is the length scale over which the direction of light propagation is randomized. When the particle size a is comparable with the wavelength of light λ, scattering is strong and $l \sim l^*$. On the contrary, when $a \ll \lambda$, l and l^* become very large, with $l < l^*$, and multiple scattering is relatively low. In the highly multiple scattering limit, an expression for the field autocorrelation function can be obtained by using the diffusive approximation. Let's consider a DWS measurement in transmission geometry, with a sample of thickness $L \gg l^*$ and the scattered light collected from a small area at the edge of the sample. A single photon passing through the sample undergoes n scattering events and emerges with a phase that depends on its total path length s. The total phase shift of the photon after passing from the laser to the detector is $\Phi(t) = k_i s(t)$. The total field at the detector is the superposition of the fields from all light paths through the sample to the detector:

$$E(t) = \sum_{p}^{N} E_p \exp(-i\Phi_p(t))$$

where the sum is over the paths and E_p is the amplitude of the field at the detector from path p. Another sum over the particles in each path is implicitly contained in $\Phi_p(t)$. For a large number of paths N and for independent particles, the electric field correlation function can be expressed as a sum over path lengths s (in order to simplify the formalism, we consider the stationary case):

$$g^{(1)}(t) = \sum_{s} P(s) \exp(-\frac{1}{3} k_i^2 \langle \Delta r^2(t) \rangle \frac{s}{l^*})$$

where $P(s)$ is the fraction of scattered intensity in paths of length s and $\langle \Delta r^2(t) \rangle$ is the mean square displacement of the particles. For diffusive motion and passing to the continuum limit, we obtain

$$g^{(1)}(t) = \int_0^\infty P(s) \exp(-\frac{2t}{\tau} \frac{s}{l^*}) ds \tag{3.27}$$

where $\tau = (k_i D)^{-1}$. Therefore, a light path of length s corresponds to a random walk of s/l^* steps and such a path contributes, on average, $\exp(-2t/\tau)$ per step to the decay of the autocorrelation function. The characteristic decay time for a light path of length s is $\tau l^*/(2s)$, the time it takes the total length to change by $\approx \lambda$. Thus, the decay time of long light paths will be relatively short and viceversa. Long paths decay relatively quickly because displacements of the single particles much smaller than one wavelength are enough to induce a change by one wavelength for the entire path length. In the following, we will keep considering a Brownian motion for the particles of the sample.

An explicit expression for the correlation function $g^{(1)}(t)$ can be obtained by calculating the path length distribution $P(s)$. Exploiting the diffusive nature of light transport in highly scattering media, $P(s)$ can be calculated by solving the diffusion equation for light with the appropriate boundary conditions. Therefore, the final expression for $g^{(1)}(t)$ depends on the boundary conditions: the size and shape of the sample, the size of the incident beam, which may be expanded or collimated, and the point from which the outgoing light is collected. On the other hand, as the number of scattering events is large, there is no appreciable angular dependence of the scattered light fluctuations, contrarily to DLS.

In the transmission geometry, nearly all the photons leaving the sample will have scattered the same number of times, corresponding to $n \approx (L/l^*)^2$ random walk steps and will have travelled a total distance $s \sim nl^*$. Since all the photons scatter approximately the same number of times, $g^{(1)}(t)$ will decay nearly exponentially: $g^{(1)}(t) \approx \exp(-t/T)$. As the correlation function decays, on average, $\exp(-2t/\tau)$ per step, the characteristic time of $g^{(1)}(t)$ is approximately $(l^*/L)^2\tau$. Another commonly used geometry in DWS experiments is the backscattering geometry. It is very convenient, as it requires access to the sample from only one side. However, as backscattering involves a significant number of light paths with length comparable to l^*, the diffusion approximation must be used with caution in describing light transport. In this geometry, there is a very broad distribution of photon path lengths: some photons will enter the sample and scatter only a few times before leaving, while others will scatter many times before being collected. Correspondingly, there will be a broad distribution of decay times, so we expect that $g^{(1)}(t)$ is a stretched exponential. The behavior of the correlation function is well approximated by the expression $g^{(1)}(t) = \exp(-\alpha\sqrt{6t/\tau})$, where α is a parameter depending on the geometry. The long light paths, which decay

quickly and probe relatively short length scale motion, will contribute to the fast decay of $g^{(1)}(t)$. At longer times, the decay of the correlation function comes from the short paths and probes relatively long length scale motion.

Let's conclude with the case of a multiple scattering sample under shear [77]. We neglect Brownian motion and only consider a stationary shear for the particles in the suspension, with a shear rate $\dot{\gamma}$. The mean square displacement of the particles along the flow direction will be $\langle \Delta r^2(t) \rangle \simeq (\dot{\gamma} t)^2$. As the integration in equation 3.27 is over s, once the new expression for $\langle \Delta r^2(t) \rangle$ has been substituted, the same derivations can be followed by replacing $2t/\tau$ with $(k_i \dot{\gamma} t)^2 l^{*2}/30$. For example, in the backscattering geometry, one obtains

$$g^{(1)}(t) = \exp(-t/\tau) \tag{3.28}$$

with $\tau^{-1} = \alpha k_i l^* \dot{\gamma}/\sqrt{10}$. As in dynamic light scattering, investigation of the system dynamics under shear is limited by this decorrelation effect of geometrical nature and the slow relaxation time of the system is not accessible under flow. This is the reason why the shear has always been stopped during the measurements in the DWS experiments proposed in the literature to investigate the effect of the flow on a colloidal system dynamics [6, 7].

CHAPTER 4

The samples and the techniques

The behavior of colloidal systems under an imposed flow has been largely investigated from a mechanical point of view through rheology. Complex phenomena like shear thinning, shear thickening or yield stress have been evidenced experimentally and many phenomenological and microscopic theories have been proposed to describe them, as reported in the previous chapters. However, the experimental study of the microscopic dynamics underlying these rheological behaviors is still relatively poor, due to the difficulty in monitoring the dynamics of the system under an imposed flow. During our experimental work, we have used light scattering techniques to investigate how a shear flow influences the dynamics of the colloidal particles in the system. In particular, through DLS we directly accessed the density autocorrelation function of the particles of a Laponite suspension, a shear thinning system largely investigated in the "glass" community. The rejuvenation effect of a steady shear flow on the aging dynamics of the system has been largely studied. The formation of shear bands with a complex phenomenology has also been monitored at low applied shear rates and an attempt of detecting a distinct dynamics in the different shear bands has been done. The sample and the methods used for these experiments are described in 4.1. The effect of the flow on the dynamics of a shear thickening system has also been investigated. With this purpose, a concentrated suspension of silica particles has been synthesized. The sample is highly multiple scattering and a particular

technique based on DWS, called Speckle Visibility Spectroscopy, has been utilized. The technique and the sample for this experiment are presented in 4.2.

4.1 DLS measurements on a glassy suspension

The effect of the flow on the dynamics of a glassy suspension will be experimentally investigated under several aspects using a DLS apparatus. The general properties of the Laponite sample used in the experiments are described in 4.1.1. The DLS set-up used for measuring the intermediate scattering function and optionally monitoring the detailed velocity profile during the flow is described in 4.1.2. The homodyne method will be used to follow the evolution of the intermediate scattering function during aging, when the system is subject to a steady shear flow (the shear will be temporarily stopped during the measurement). Through the heterodyne method, shear banding phenomenon will be observed instead. When shear banding phenomenon occurs in glassy colloidal suspensions, a different dynamics is expected in the different shear bands. As we will explain in 4.1.3, the classical DLS measurements in homodyne method cannot be used to investigate these dynamics and a new DLS method, based on an ensemble average over many rejuvenating experiments, is proposed to measure the intermediate scattering function. This method will also be exploited to study the effect of a shear rejuvenation on the following aging dynamics, when the shear is applied to a Laponite sample in the arrested phase.

4.1.1 The Laponite clay suspension: a model system for glassy dynamics

The sample we used in our experiments is a suspension of a synthetic mineral clay, called Laponite. Mineral clays are a group of silicate materials characterized by a layered structure. When wetted, clay is plastic and can be easily shaped. Once dried, it becomes firm and, when subject to high temperature, permanent physical and chemical reactions occur, inducing hardening of the clay. All these properties made clay an ideal substance for earthenware, building bricks and pottery since prehistoric times. Besides, water suspensions of clays show thixotropic properties, as one may have experienced when walking on a wet clay soil (the shear exerted by the shoe sole makes the soil slippery).

This rheological behavior is largely exploited in industry: the Laponite clay, for example, is often used as an additive to modify the rheological behavior of many waterborne products such as surface coatings, household cleaners and personal care products. Besides its various industrial applications, Laponite suspensions represent a very interesting colloidal system in the physicists' community. Indeed, these suspensions display a dynamical behavior typical of glassy systems, which makes them an ideal model of soft glassy materials. Laponite samples also have the advantage of a very simple preparation and thus their dynamical and rheological behavior have been largely investigated experimentally. In the following, the chemical structure of the Laponite particles in a water solution is discussed. Then, some theoretical, numerical and experimental works investigating the dynamics and rheology of Laponite suspensions are briefly presented. Finally, the procedure we have followed to prepare the samples is described.

Chemical structure of mineral clay colloids

Typically, the layered structure of mineral clays consists in two dimensional sheets of tetrahedrally coordinated silica linked to parallel sheets of octahedrally coordinated alumina or magnesium oxide. Each silica layer is a monocrystalline structure consisting of planes of silica tetrahedra (SiO_4^{2-}) covalently bonded together. The surfaces of the silica sheet are covered by the oxygen atoms of the tetrahedra and are hence negatively charged. The octahedral sites in between the silica layers are occupied by divalent or trivalent ions. Alkali ions like potassium K^+, sodium Na^+, or calcium Ca^{++} compensate the oxygen charge forming an ionic bond. Synthetic clays like Laponite are in general synthesized in a sodium rich environment, then the great majority of their inter-layer cations are sodium ions [83]. This layered structure is easily cleaved along the oxygen surface plane into separate leaves, because the bonding between different crystals are much weaker than the bonding between tetrahedral sheets within each sheet. Many clay mineral particles, such as hectorite and bentonite, have a column shaped structure when dry, with the monocrystalline layers orthogonal to the column axis. When dispersed in a polar solvent, like water, the weak bonds are easily broken as the solvent penetrates into the inter-layer regions. The layered structure thus separates into primary discoidal particles with the octahedral layer sandwiched between two silica layers, and become dispersed as colloidal platelets.

Among synthetic mineral clays, Laponite is characterized by discoidal particles that closely resembles the hectorite natural clay in both structure and composition. Its mass density is $\rho_L = 2.7\ 10^3$ Kg/m^3 and the unitary disk has an average diameter of 25 nm and is 1 nm thick. Laponite particles are quite monodisperse, with a relative diameter variation of about 30% [84]. Each platelet contains roughly 1500 unitary cell, which are repeated in two directions and result in the disc shaped appearance of the crystal. The unit cell is constituted by six octahedral magnesium ions sandwiched between two layers of four tetrahedral silicon atoms groups. These groups are balanced by twenty oxygen atoms and four hydroxyl groups. Some magnesium ions are substituted by lithium ions and some spaces are empty, to give typically a composition with the empirical formula:

$$Na^{+0.7}[(Si_8Mg_{5.5}Li_{0.3})O_{20}(OH)_4]^{-0.7}$$

The height of the unit cell represents the thickness of the Laponite disk. In dry Laponite powder, due to the holes of magnesium ions, the disks would have a deficiency charge of 0.7 per unit cell. Sodium ions thus sandwich between the platelets neutralizing them and inducing the column shaped structure. In water, this structure is believed to disperse into single unitary disks (Fig. 4.1). Sodium ions are thus released from the surface of the particles, leading to a negative charge on the crystal surface. The free sodium counterions are attracted by the bare negative charge on the surface of the discoidal particle. A fraction of them is again adsorbed on the platelet, the others remain into the surrounding of the surface, giving rise to a layer of condensed counterions. At the same time, depending on the solution pH, the edge of the disc adsorbs hydroxyl groups, getting positively charged. When Laponite is suspended in pure water, the value of the pH is ≈ 10, corresponding to an ionic strength $I \approx 10^{-4}$M (the whole contribution to the ionic strength of the sample is due to the hydroxyl groups). At the end, the total negative charge on the surface of the platelets is about 700 elementary charges, while the positive charge on the edges is about one order of magnitude smaller than the surface charge.

Dynamics in Laponite suspensions

Laponite have been extensively investigated as a model system for disk-like charged colloids. Due to the electric double layer around the platelets, the interacting potential between the colloids is a repulsive Yukawa potential [85],

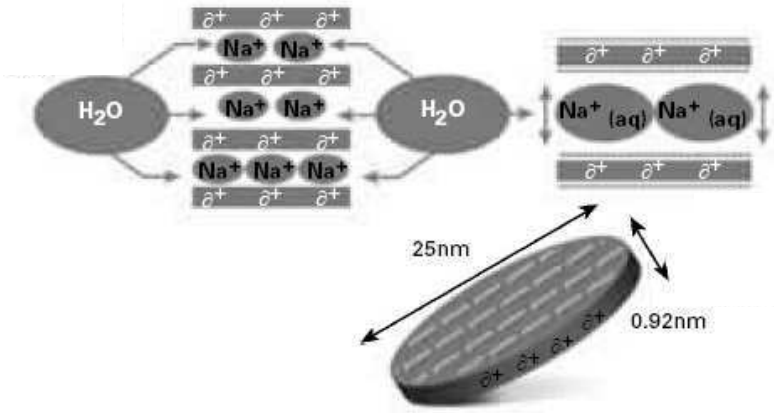

Figure 4.1: *Hydration of the sodium ions. In the dried powder, Laponite particles are organized into columnar structure. In aqueous dispersion, water hydrate sodium ions in the interlayer region, leading to a dispersion of single laponite particles. The typical dimensions of a single Laponite disc are also drawn. Figure from [86].*

characterized by a screening length of about 30 nm at $pH = 10$. Taking into account this screening effect, concentrations of the order of 1% in volume correspond to effective volume concentrations of about $\sim 50\%$, which is the value at which glassy phase is observed in hard-sphere systems. Diverse theoretical and numerical works have been devoted to the study of the complex behavior resulting from this electrostatic interaction between the platelets. In Ref. [87], the suspension has been modelled by a system of nonintersecting disks carrying a rigid point quadrupole, which favors edge-to-face pair configurations. Monte Carlo simulations on this model show that, at sufficiently large values of the quadrupole moment, the system undergoes a reversible sol-gel transition: at low concentration, disks assemble into elongated clusters, while a space-filling gel phase is found at higher concentrations. The gel phase exhibits a nearly incompressible network structure similar to the "house-of-cards", in which most of the particles are edge-to-face to each other and there is no long-range order. This structure is conjectured to be typical of clay gelation. Recent Brownian dynamics simulations [88] have explored the out of equilibrium dynamics of a Laponite model with a repulsive Yukawa potential among the particles. As a result, an aging behavior driving to an arrested disordered state is observed.

The phase diagram of Laponite suspensions has been largely investigated experimentally, with particle concentration and ionic strength being the two parameters controlling the system [89, 90, 91, 92, 93]. The formation of a disordered arrested phase even at very low volume fractions and high ionic strength has been observed, while at higher ionic strength ($I \gtrsim 10^{-2}$), flocculation occurs. It has largely been debated whether the arrested phase of Laponite suspensions corresponds to a gel or a glassy phase [89, 90, 94]. Anyway, the aging dynamics, which drive to the arrested phase, is believed to be induced by the formation of particle aggregates. By monitoring the intermediate scattering function through DLS [92, 95, 96], the aging dynamics is observed to display a two step relaxation scenario: a fast exponential relaxation process, whose characteristic time τ_f remains of the same order of magnitude found in very dilute suspensions; and a slow stretched exponential process, with characteristic time τ_s. The fast relaxation is found to be independent on the age of the system and is believed to be related to single particle diffusion. The slow relaxation is instead related to cooperative motions and is observed to increase exponentially, or more than exponentially with the waiting time t_w, while becoming strongly stretched. When the ionic strength is increased, the growth of τ_s proceeds more rapidly. For sufficiently concentrated samples, a two stage aging process has been observed through Multi-Speckle Dynamic Light Scattering [96, 97]: after the exponential regime, a linear dependence of τ_s on t_w shows up at long t_w.

Rheological measurements

The aging dynamics and the effect of a steady shear has also been investigated through rheology [20]. The external drive is observed to induce a drastic slowing down of the aging dynamics or even, in some cases, the rejuvenation of the system. Under shear, the spontaneous aging process observed at rest is suppressed after surprisingly long time: in the numerical simulations described in 2.3.4, a stationary state is reached instead after a short transient of a few $\dot{\gamma}^{-1}$. In the non-equilibrium stationary state, the viscosity η depends on the applied shear rate through the shear thinning behavior $\eta \sim \dot{\gamma}^{-m}$, with $m = 0.6$. Actually, in another work (by the same authors!) [3], a different exponent is found: $m = 0.9$. As described in 1.3.1, in this last work, the effect of a shear flow on the aging dynamics has also been investigated microscopically, but a quantitative analysis is missing.

Sample preparation

For our experiments, the sample is prepared following the procedure usually described in the literature [90]. In particular, Laponite powder provided by Laporte Ltd is dispersed in ultrapure deionized water at 3.4% wt concentration and stirred for ~ 30 min. In order to eliminate aggregates (which may form through the electrostatic interaction between the particles), the sample is then filtered through a Millipore filter with a pore dimension of 0.45 μm. While filtering, the sample is loaded into the shear cell. The obtained suspension is optically transparent and initially "liquid". Cell loading is taken as the origin of waiting times t_w^0 for the aging dynamics of the system at rest.

4.1.2 The experimental set-up for homodyne and heterodyne method

The sample is investigated in a home made [98], cone and plate shear cell for DLS measurements, having a flat optical window as the static plate. The cone has a radius of 5 cm and a bottom angle $\alpha = 0.20$ rad (Fig. 4.2). It is made up of aluminium and the surface is covered by a thin layer of paint, in order to prevent ions from being released from the metal into the Laponite suspension, thus changing the ionic strength of the sample. To minimize stray light at the interface between the cone and the sample during the DLS experiments, we used black paint. The cone is made rotate around its symmetry axis at an angular velocity ranging from $10^{-2}\,Hz$ to $10^{2}\,Hz$ by a DC electrical motor with permanent magnet. The rotational axis is put in the horizontal direction. Optionally, a plate-plate geometry can be used by exchanging the cone with a glass plate of the same dimension. The glass refractive index is 1.41 and the one of water (which is the average refractive index of dilute Laponite suspensions) is 1.33: the difference among the two indexes is small enough that the stray light at the interface is negligible.

The set-up we implemented for DLS measurements is sketched in Fig. 4.3. A diode pumped solid-state laser ($\lambda = 532$ nm, $P = 150$ mW) is directed towards a beam splitter; one of the two beams coming out is directed, through a mirror and a convergent lens (of focal length $f = 250$ mm), towards the cell containing the sample; the other beam, representing the local oscillator, is attenuated by a filter and collected by a fiber collimator (of focal length $35\,mm$), followed by a single-mode optical fiber (f_1, core diameter $3.5\,\mu m$). The beam scattered by the sample passes through a convergent lens (of focal

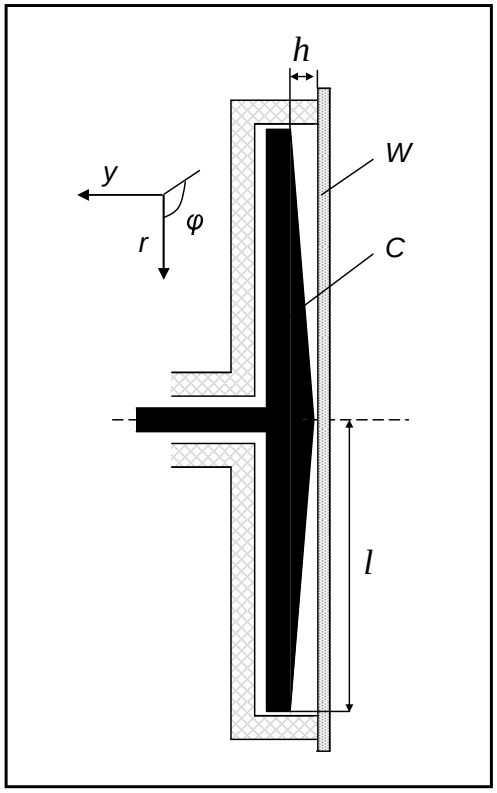

Figure 4.2: *Shear cell used in the DLS experiments. W: optical window, C: cone rotating around its symmetry axis, l: radius of the cone, $\alpha = l/h = 0.20$ rad: angle of the cone with respect to the bottom plane. A cylindrical coordinate system is also drawn.*

length $f = 100$ mm) and is collected, in the direction perpendicular to the optical window, by another couple of collimator (of focal length $50\,mm$) and fiber (f_2). Approximating the beams as Gaussian beams [102], the focal length is $z_0 = 160$ mm for the incident and $z_0 = 13$ μm for the scattered beam. We fixed the intersection of the incident and scattered beam as closer as possible to the waists (the waist is the focal point of the beam). Both fibers are polarization-maintaining and the interference among the scattered field and the local oscillator is achieved through a fiber optics beam splitter, which ensures an optimal matching of the beam wavefronts [79]. Another optical fiber propagates the interfering beam from the beam splitter to a

photomultiplier (*Hamamatsu*). Finally, the digital signal in output from the photomultiplier is sent to a correlator: photocounts are acquired through a general purpose, counter/timer PCI board (*National Instruments PCI 6602*) and a set of software classes (implemented as extension modules of the object oriented language *Python*) have been developed to perform basic tasks for the statistical analysis of digital pulse trains. A typical application is real time multi-tau photon correlation. However, a software approach, having access to the full photocounts train, allows to efficiently prototype different analysis protocols, going far beyond the simple autocorrelation function [99, 100].

In our experiment, the scattering geometry is fixed at a scattering angle $\theta = 132^{o}$, thus the scattering vector is $q = 22\ \mu\text{m}^{-1}$. This fiber collection apparatus allow a direct visualization of the scattering volume, as suggested in Ref. [79]. Replacing the fiber f_1 collecting the local oscillator with the one at the opposite side of the beam splitter (see Fig. 4.3), the scattering volume results as the intersection of the incident beam and the beam coming out from f_2. The scattering volume dimensions are $c \sim 160\ \mu$m in the x-direction and $a \sim 120\ \mu$m in the y-direction (see Fig. 3.3). We placed the shear cell in order to have the scattering volume positioned at a radial distance $R = 2.1$ cm from the rotational axis and the flux velocity in the azimuthal direction (see the cylindrical coordinate system drawn in Fig. 4.2) coplanar with the incident and scattering beams.

In the following, we describe the experimental protocols used for the investigation of the particle dynamics through the homodyne technique and for the velocimetry measurements through the heterodyne method.

Dynamics investigation through the homodyne method

For the sample of Laponite at 3.4% wt concentration, the number of scattering platelets in the scattering volume is about 10^{11}. The Gaussian approximation is therefore valid and the Siegert relation 3.14 holds. Through the homodyne method (achieved by blocking the beam of the local oscillator in the set-up described above), the intermediate scattering function can thus be measured in the system at rest, giving a direct investigation of the system dynamics. With respect to pinhole collection, classically used in DLS, the optical fiber collecting device ensures a higher spatial coherence of the beam on the photocatode [101]. Indeed, the electric field passing through the collecting fiber has a fixed transverse profile [102], and the motion of the scatterers result only in fluctuations of the amplitude and the phase of the field

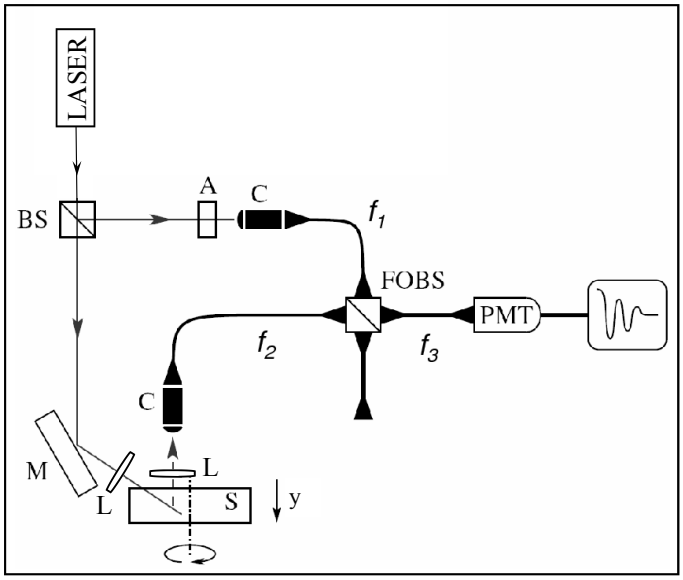

Figure 4.3: *Experimental setup for DLS measurements. BS: beam splitter, A: attenuator, C: collimator, M: mirror, S: sample, FOBS: fiber optics beam splitter, f: single-mode fibers, L: converging lens, PMT: photomultiplier.*

wave. Therefore, the optimal value $B = 1$ may be reached in equation 3.14. An example of the correlation functions measured in the homodyne mode is shown is Fig. 4.4, where the aging dynamics of a Laponite suspension is monitored after cell loading.

When the system is under shear, fast decorrelation of the measured correlation function due to geometrical effects will be observed, as explained in 3.1.2. In any point along the cell gap, the advection time τ_a will be responsible for this decay, as the corresponding transit time τ_t is expected to be much longer than τ_a in this scattering geometry. For example, fixing the minimum shear rate applicable in the cell $\dot{\gamma} = 1.3\ 10^{-2}\ \mathrm{s}^{-1}$ (assuming a linear velocity profile along the gap), using equation 3.22 and 3.23, we obtain $\tau_a \sim 6$ ms and $\tau_t \sim 240$ ms when the scattering volume is in the middle of the gap. When we study the influence of a shear flow on the aging dynamics of the Laponite sample, the timescales characterizing these slow dynamics will soon become larger than τ_a, already at the minimum applicable shear rate (see Fig. 4.4). For this reason, the homodyne measurements will be always performed in

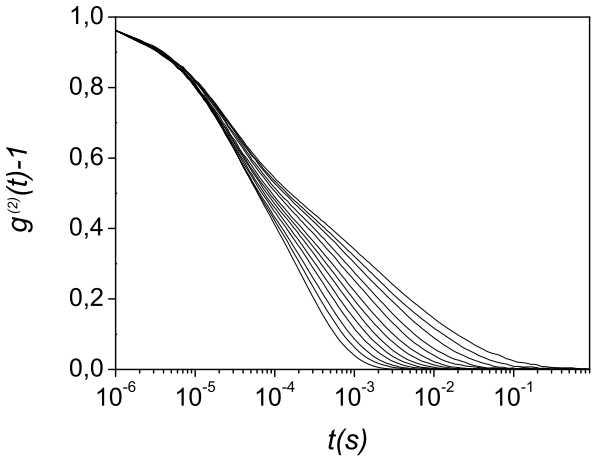

Figure 4.4: *Normalized intensity autocorrelation functions during aging, for ten equally spaced waiting times between* 0.1 *and* 15 *hours, when a Laponite suspension is left still after cell loading.*

short time intervals during which the shear is stopped.

Velocimetry measurements through the heterodyne method

By choosing the heterodyne correlation scheme, the detailed velocity profile in the shear cell can be measured by shifting the cell along the velocity gradient direction. As explained by equation 3.26, the velocity of the particles in the scattering volume is obtained from the oscillating frequency ω of the measured correlation function: $v = \omega/(q\cos\boldsymbol{\hat{qv}})$, where $q\cos\boldsymbol{\hat{qv}}$ is fixed by the scattering geometry. The frequency ω can be easily obtained as the point of maximum of the correlation function Fourier transform [100]. In order to spare computational time, one can directly calculate the Fourier transform of the collected intensity $I_e(t)$ and obtain the same result. Indeed, according to the Wiener-Khinchin theorem, the power spectral density of a stationary random process is the Fourier Transform of the corresponding autocorrelation function:

$$\int_{-\infty}^{+\infty} \langle I_e(0) I_e(t)\rangle \exp(2\pi i\nu t)dt = 2\pi \left| \int_{-\infty}^{+\infty} I_e(t)\exp(2\pi i\nu t)dt\right|^2$$

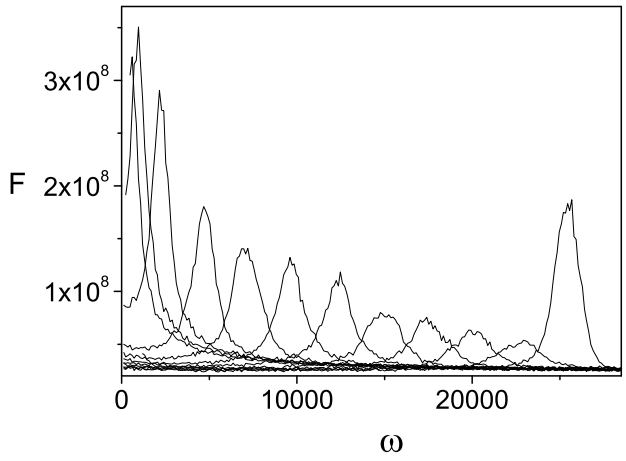

Figure 4.5: *Time Fourier transform F of the intensity signal collected through the heterodyne set-up for equally-spaced positions of the scattering volume spanning the entire gap in the plate-plate geometry. The increase in the amplitude of the peak as the static window is approached is probably due to an increase of the scattering intensity (such heterogeneity may be induced by the cell wall). For each curve, the point of maximum ω_m is related to the particle velocity $\boldsymbol{v}$ in the scattering volume through the relation $\omega_m = \boldsymbol{v} \cdot \boldsymbol{q}$.*

The particle velocity in the scattering volume can thus be measured in real time by calculating, through the software correlator, the Fourier transform of the intensity signal $I_e(t)$ acquired in the time interval $0 \div T$, as shown in Fig. 4.5. The maximum time resolution that we can achieve with this measurement, at a fixed position of the scattering volume in the gap, is $T = 10^{-2}$ s. The spatial resolution is instead determined by the scattering volume dimensions $\sim 100\mu$m. Considering that the gap width is $H = R \tan \alpha = 4.2$ mm, a good spatial resolution is assured in the measurements of the velocity profile.

4.1.3 A new method for measuring the Intermediate Scattering Function

Through the velocimetry measurements, shear localization phenomenon is observed in the Laponite suspension for low applied shear rates and for long waiting times since sample filtration. These results will be presented in 6, here we only want to explain the motivations leading us to the introduction of a novel DLS method. As suggested by the numerical and theoretical studies on shear localization (see 2.3.3, 2.3.4), the dynamics is expected to be arrested in the null shear band and fluid-like in the band at finite shear. Experimentally, this difference in the dynamical behavior hasn't been evidenced yet. As usual, the dynamics can't be monitored under shear, but may be followed soon after shear stop in the two different bands. If the dynamics in the two bands is completely different during the flow, we expect this difference to be reflected in the dynamics of the particles soon after flow cessation in the two regions of the sample. As we will report in 5.3, the aging dynamics following shear cessation, when the time elapsed since sample filtration is long, proceed very fast. As a consequence, DLS can't be the proper technique to investigate such dynamics.

Indeed, in classical DLS experiments, the intensity correlation function is measured as an average on the time origin over the acquisition time T (see equation 3.1). When investigating Laponite system dynamics, the acquisition time T needed to get a good signal to noise ratio must be kept longer than the characteristic slow relaxation time of the system τ_s and shorter than the time one should wait before changes in τ_s, due to the aging process, are significant. This condition doesn't hold when the aging dynamics is characterized by a very fast evolution, as in the case described above. The intensity correlation function thus cannot be obtained by time averaging and an ensemble average may overcome the problem. Multi-Speckle Dynamic Light Scattering (MS-DLS) or Multi-Speckle Diffusive Wave Spectroscopy (MS-DWS) compute the intensity correlation function by averaging the intensity fluctuations over the pixels of a digital camera detector, which collects part of the speckle pattern [109]. The acquisition time is strongly reduced in these techniques, enabling the investigation of the system dynamics for much longer τ_s or for faster aging processes. However, in both techniques, the time resolution is much smaller than in DLS, as it is limited by the frame rate of the camera device used as detector. In particular, the timescale characterizing the slow dynamics of the Laponite suspension in the regime we are interested in may be too short

to be investigated through MS-DLS.

Thus, an original protocol to measure the intensity correlation function is used. The intermediate scattering function is calculated as an ensemble average over many rejuvenating experiments:

$$g^{(2)}(t_0, t) = \langle I(q, t_0) I(q, t_0 + t) \rangle_e / \langle I(q) \rangle_e^2$$

where $\langle .. \rangle_e$ indicates the ensemble average over several intensity evolutions acquired after cessation of a repeated shear application. In particular, we choose the following protocol: a shear rate $\dot{\gamma}_1$ is applied to the system for a time interval T_1; after shear cessation, the counting of t_w starts and the intensity fluctuations are collected for a time interval T_0 with a time resolution of dt; then a shear rate of the same value $\dot{\gamma}_1$ is applied for T_1 and the cycle starts again. The whole measurement lasts several hours and we obtain an ensemble of N acquisitions, having T_0/dt counts each, after the same initial conditions are imposed. In order to reach a good signal to noise ratio in the correlation function, N need to be large. For this reason, the acquisition time is extremely long in comparison to MS-DLS technique, but the time resolution, fixed by dt, can be much higher with this DLS technique and enables the investigation of faster dynamics.

Once the counts have been collected, we proceed to the calculation of the correlation functions. To speed up the computation, the acquired counts are first logarithmically binned: a logarithmic binning of t_w is performed and the counts are averaged in each bin. The intensity autocorrelation function is then calculated for various t_w as an ensemble average over all the bunches of counts, in the time window $dt \div T_0$. Calling $n_i(t_w + t)$ the number of counts in the bin at the elapsed time $t_w + t$ since shear cessation and at the i-th acquisition, we can write

$$g^{(2)}(t_w, t) = \frac{1}{N} \frac{\sum_{i=1}^{N} n_i(t_w) n_i(t_w + t)}{\bar{n}^2}$$

where $\bar{n}$ is the average of all the counts in all the N acquisitions. The resulting correlation functions are checked to be independent on the binning procedures. An example of the resulting correlation functions is represented in Fig. 4.6. In the following, consistency with classical DLS has been checked for this original method of DLS.

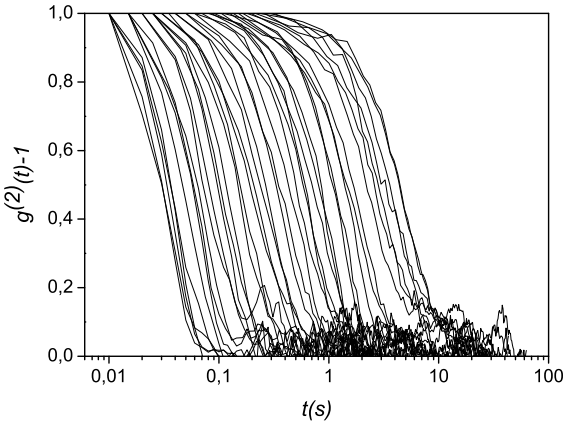

Figure 4.6: *Normalized intensity autocorrelation functions obtained as an ensemble average over many rejuvenating experiments on a initially gelled Laponite sample. The functions are calculated for a set of waiting times between* 0.3 *s and* 40 *s (from left to right) after shear cessation.*

Checking on the method

We first follow the statistics of the correlation functions calculated at different t_w [109]. We calculate for each acquisition i the value $n_i(t_w)n_i(t_w + \bar{t})/\bar{n}^2$, with $\bar{t}$ satisfying the condition $g^{(2)}(t_w, \bar{t}) = e^{-1}$. A histogram of these values calculated over the N acquisitions can be plotted for various t_w (Fig. 4.7). Its shape, though very large, ensures that good statistics have been done in the calculation of the correlation functions.

In order to compare the correlation functions measured through classical DLS and through this novel method, we monitored the dynamics of a Laponite sample aging under shear (this regime will be described in details in 5.2). At elapsed time $t_w^0 \lesssim 30$ h since sample filtration, the system dynamics after shear are stationary over the timescale of the tens of seconds and can thus be investigated through classical DLS too. Soon after cell loading, the sample is left aging under shear at $\dot{\gamma}_1 = 100\ s^{-1}$ and periodically shear is stopped after a time $T_1 = 60$ s, a pause of 5 s is taken in order to avoid inertial effects due to flow stop and then the scattered intensity is acquired for $T_0 = 1$ s, with a time resolution $dt = 10^{-5}$ s. Each hour, the time-averaged intensity

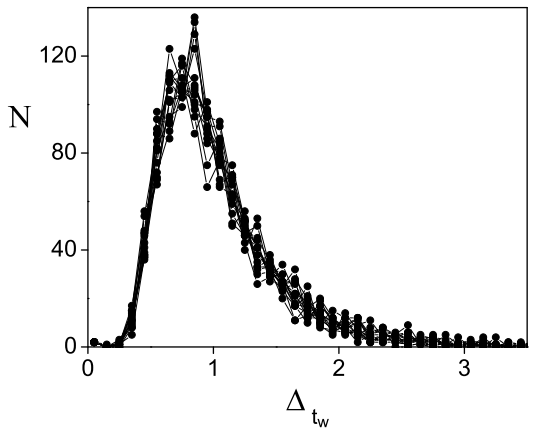

Figure 4.7: *Histograms for the ensemble averaged correlation functions: for 14 waiting time values between* 1 *and* 80 *s, we plot the histograms of* $\Delta_{t_w} = n_i(t_w)n_i(t_w + \bar{t})/\bar{n}^2$ *(with* $\bar{t}$ *satisfying the condition* $g^{(2)}(t_w, \bar{t}) = e^{-1}$*) calculated for each acquisition* i *among* $N = 950$ *acquisitions.*

correlation function is also measured through classical DLS by stopping the shear for 80 s. The experiment lasts 24 h and the ensemble averaged intensity correlation function is calculated from $N = 1300$ acquired bunches of counts. As we will show in 5.2, the system under shear keeps on aging with t_w^0. Thus, the dynamics change during the whole experiment and the ensemble averaged correlation function will provide an average value of the slow relaxation timescale. The ensemble averaged intensity correlation function is thus compared to the average of all the intensity correlation functions measured during the experiment through classical DLS. As it is evident from Fig. 4.8, good agreement is observed between the intensity correlation functions measured through the two methods.

4.2 Speckle Visibility Spectroscopy on a shear thickening sample

Concentrated suspensions of silica particles have been largely used to investigate the rheological behavior of charge stabilized colloids. When the

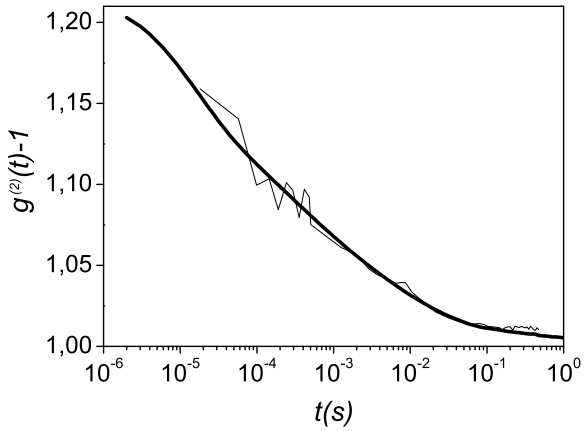

Figure 4.8: *Intensity correlation function measured as an ensemble average over many intensity acquisitions after shear cessation (thin line) compared to the time averaged correlation function measured through classical DLS (bold line). Measurements are performed on a Laponite sample aging under shear at* $\dot{\gamma}_1 = 100\ s^{-1}$ *for 24 h. As the sample ages during this long acquisition time, the correlation function plotted in bold line is an average of all the correlation functions acquired during the experiment through classical DLS.*

suspension is sheared over a critical shear stress, a shear thickening behavior is observed. At the microscopic level, clusters of particles are believed to be responsible for this behavior. We will investigate the dynamics of these flow induced heterogeneities through speckle visibility spectroscopy (SVS), a recently introduced technique, which is based on DWS. In the following, the experiments already proposed in the literature on the silica suspension are briefly discussed and the synthesis we performed to obtain the sample is described (4.2.1). The experimental apparatus for optical measurements on a shear thickening sample is presented in 4.2.2, while the basic principles of the SVS are discussed in 4.2.3.

4.2.1 The Silica suspension

A colloidal suspension of spherical silica particles is stabilized through the electrostatic repulsion between the spheres, which are negatively charged

(as soon as p$H>$ 3). Positive counterions, gathering around the particles, screen the interaction and induce an increase of the effective diameter of the particles and a higher effective volume fraction. Such suspensions represent a model system for spherical charged colloids. For this reason, the rheological behavior of concentrated silica suspensions has been extensively studied in the literature [103, 104]. From mechanical measurements, yield stress is observed in the limit of low shear rates; a shear thinning regime follows as the stress is increased and, above a critical volume fraction Φ_c, shear thickening is observed above a critical stress σ_c. When steady shear rate is applied on the system, giant stress fluctuations are observed in a small range of concentrations and shear rates, indicating a jamming transition [104]. At the microscopic level, when the suspension is ordered at rest (high volume fractions), an ordered structure is kept during the flow at low shear rate, inducing the shear thinning behavior. At high shear rates, this ordered structure melts, but only above Φ_c this melting leads to shear thickening.

The scaling behavior of the critical stress σ_c with the volume fraction Φ has been investigated [103], and a decreasing trend of σ_c as Φ increases (provided that $\Phi > \Phi_c$) is found. The effect of the particle surface roughness on the onset of the thickening regime has also been studied [106]: for fixed particle size, shear thickening occurs at smaller volume fractions and smaller shear stress when the particle surface is rough. This is because the increased inter-particle contacts and friction, due the rough surface, increase the overall viscosity (see 2.5.2). To reach more easily the jamming regime in our experiments, the particle surface will be roughened.

Synthesis and sample preparation

The silica particles have been synthesized according to Stöber method [105], which is based on the hydrolysis and condensation of tetraoxydethylsiloxane (TEOS), with formula $Si(OC_2H_5)_4$, in a basic medium made up of a solution of ethanol (HOC_2H_5), water and ammonia. The balance equations of the synthesis may be written as:

$$Si(OC_2H_5)_4 + 4H_2O \xrightarrow{NH_3,\, HOC_2H_5} Si(OH)_4 + 4C_2H_5OH \qquad (4.1)$$

$$Si(OH_4) \xrightarrow{NH_3,\, HOC_2H_5} SiO_2 + 2H_2O \qquad (4.2)$$

When TEOS is added to the basic solution, the hydrolysis produces SiO_4, whose concentration grows with time until a maximum (reached after about

1 minute) and then decreases. Germs of silica particles nucleate when an excess of SiO_4 is present in the solution, while when the concentration of SiO_4 decreases under a threshold, layers of silica form around the previously nucleated particles. The first step in the synthesis consists in the nucleation of these germs, while a phase of continuous growth of the silica particles follows, leading to a very monodisperse suspension. The shorter is the nucleation period with respect to the growth period, the more monodisperse will be the particles at the end of the synthesis. During the growth period, the concentration of SiO_4 must be kept low, in order to avoid nucleation of new particles with a consequent increase of polydispersity. For this reason, low quantities of the reagents (TEOS and the basic solution) have to be added periodically to the initial solution during the growth phase, until the silica particles reach the size needed.

At fixed temperature, the particle diameter depends on the relative concentration of $TEOS/H_2O/NH_3$ and can be determined through an empiric equation [106]. Once the concentrations of the reagents are chosen, one proceeds to the nucleation phase. The average diameter d_0 of the silica particles after nucleation is measured through DLS. For the growth regime, one expects an average final diameter $d = d_0(n/n_0)^{1/3}$, where n_0 is the mass of TEOS added to the basic solution during the nucleation period, while n is the total mass of TEOS added during the whole synthesis. The relative concentrations of TEOS, ethanol, ammonia and water have been chosen in order to obtain a final diameter $d \sim 700$ nm. After nucleation, the particle diameter measured through DLS is $d_0 = 270$ nm, while after the growth, it is $d = 640$ nm. The silica particles are then separated from the basic reaction mixture by centrifugation, in order to obtain a water dispersion. They were redispersed in deionized water and centrifuged again 4 times.

The particle surface is then roughened by adding sodium hydroxide to the water suspension in a mass percentage of 19% with respect to the mass of silica. The dispersion is then left under stirring for 24 hours. At basic pH, the silica slowly depolymerizes [107] and one gets rough particles of the same diameter. The mean square surface roughness of the particles has been measured elsewhere by atomic force microscopy [106] and was 6.20 nm, whereas it was 0.68 nm for the particles before the attack at basic pH. The suspension is then rinsed through centrifugation and redispersed in deionized water, until pH becomes neutral. We then prepared a suspension of rough particles at a volume fraction of 0.37. The obtained sample is stable against sedimentation on the timescale of the hours, while after about one day, a

gradient in the particle concentration develops in the vertical direction. Once poured in the cell, the same sample is used during the whole experiment. Therefore, the experiment duration is limited within a few hours in order to avoid sedimentation effects. The sample has an opaque white appearance, so we can operate in a multiple scattering regime.

4.2.2 The experimental set-up

In order to perform both rheological and scattering measurements on the silica sample, a stress controlled *Carri-Med* rheometer, where the system is optically accessible, is used. The cell is a Couette cell with a rotating internal cylinder of 27.5 mm diameter and a fixed external plexiglass cylinder of 30.0 mm diameter, which lets the laser beam pass through. A *Spectra-Physics* Argon polarized laser beam, of wavelength $\lambda = 514$ nm, is expanded and hits the sample with a gaussian spot size of ~ 6 mm, at an angle of $\sim \pi/6$ from the normal of the outer cylinder surface. The light is then multiply scattered by the suspension and the backscattered light is collected, in a direction perpendicular to the cell outer surface. The collection optics consists of a collimating lens that focuses diffused light onto a diaphragm, which selects a part of it. Finally, a *Pulnix* CCD camera behind the diaphragm collects the speckle pattern. The camera device has 768×484 pixels and can collect the images at a frequency $\nu = 15$ Hz. It is interfaced to a PC provided with a *National Instruments* card and the data are analyzed in real time using *LabWindows*. The diaphragm size can be changed in order to adjust the speckle size and thus the ratio of pixels to speckle areas [109]. As the light multiply scattered by the sample is depolarized, a polarizer is added between the lens and the diaphragm in order to minimize direct reflections. All the measurements are performed in backscattering geometry, the dynamics of the particles is thus probed in a volume defined by the section of the diaphragm ($\simeq 6$ mm $\times$ 6 mm) and the photon penetration depth in the sample. Using a procedure described in Ref. [106], the photon mean free path inside the suspension has been measured: $l^* = 93 \pm 4$ μm. The penetration depth in backscattering geometry is of the order of a few mean free paths, we can thus estimate that the volume explored in an experiment is of the order of 6 mm $\times$ 6 mm $\times$ 0.2 mm. It contains about 10^9 particles, but represents a small fraction of the entire Couette cell. In particular, its depth is approximately one fifth of the gap.

Through the rheometer, we monitor the mechanical properties of the sil-

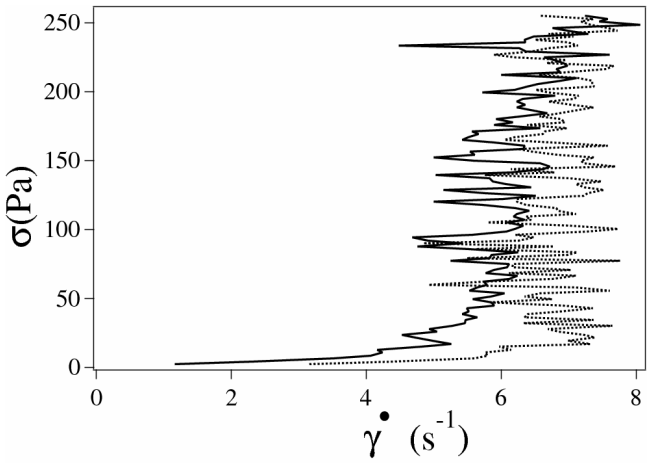

Figure 4.9: *Jamming of the concentrated suspension of rough silica particles. Stress is increased from* 0 *Pa to* 255 *Pa, at a rate of* 2.1 $Pa.s^{-1}$ *(continuous curve). Then, the stress is decreased down to zero with the same absolute rate (dashed curve). Jamming occurs for* $\sigma \gtrsim 20$ *Pa. A slight hysteresis is observed when the stress is decreased.*

ica sample by imposing a ramp of stress on the system. For small stresses, the shear rate increases smoothly with the stress; then, when the stress reaches a critical value, a transition to a different regime occurs, where huge fluctuations of the shear rate around a fixed value are observed (Fig. 4.9). The occurrence of these huge fluctuations of the shear rate evidences a transition to a jamming regime. If a decreasing ramp of stress is applied after the rising ramp, a slight hysteresis in the stress *vs* shear rate curve is observed. Interpreting the shear thickening phenomenon as due to the formation of hydrodynamic clusters (see 2.5), the following picture may hold to explain the occurrence of the jamming regime: shear induced aggregates, of macroscopic size, hinder the flow inducing a drop in the shear rate; then, at this lower shear rate, the aggregates break, so the shear rate increases and the cycle starts again.

4.2.3 Speckle visibility spectroscopy

We are interested in the investigation of the heterogeneities induced by shear in the jamming regime. In particular, we want to study the dynamics of

these heterogeneities while they relax to equilibrium after flow cessation. These dynamics will be non-stationary, and thus cannot be studied through classical DWS, in which the intensity correlation function is measured for one speckle as an average over the time origins. As described in 4.1.3, MS-DWS would overcome this limitation by averaging the intensity fluctuations over the speckles of the diffraction pattern. Nevertheless, the temporal resolution of MS-DWS is limited by the frame rate of the camera collecting the images. In the silica sample, the characteristic time of the dynamics is too small to be investigated through this technique.

A technique that can overcome these problems is the Speckle Visibility Spectroscopy (SVS), which is based on the principles of DWS (discussed in 3.2) and has been recently introduced by Dixon and Durian [110]. The basic idea of the technique is the following: if the exposure time of the camera detector is long compared to the timescale of speckle fluctuations, the same average intensity is recorded for each pixel. On the contrary, if the exposure time is shorter, the speckle pattern is visible. Thus, keeping the exposure time fixed, the faster are the dynamics of the suspension, the more the speckle image is blurred and the less contrasted is the speckle image. The temporal resolution of this technique is of the order of the exposure duration, that is much smaller than the camera frame rate (time elapsed between two successive images), and allows the study of our system dynamics. Quantitatively, one computes the contrast of an image, for a given exposure time, as the variance of the intensity distribution across the pixels:

$$C(T, t_w) = \frac{\langle (I_T(t_w))^2 \rangle_p}{\langle I_T(t_w) \rangle_p^2}$$

where the $\langle .. \rangle_p$ is an ensemble average over all the pixels and the intensity $I_T(t_w)$ is the pixel time-integrated intensity over the exposure duration T:

$$I_T(t_w) = \frac{1}{T} \int_{t_w}^{t_w+T} I(t')dt'$$

For T much larger than the dynamical timescale of the system the contrast is expected to be one, while in the opposite limit the expected value is two. The contrast can be also expressed as a function of the intermediate scattering function [111]:

$$C(T, t_w) \propto \int_0^T (1 - t/T)[g^{(1)}(t, t_w)]^2 dt/T \tag{4.3}$$

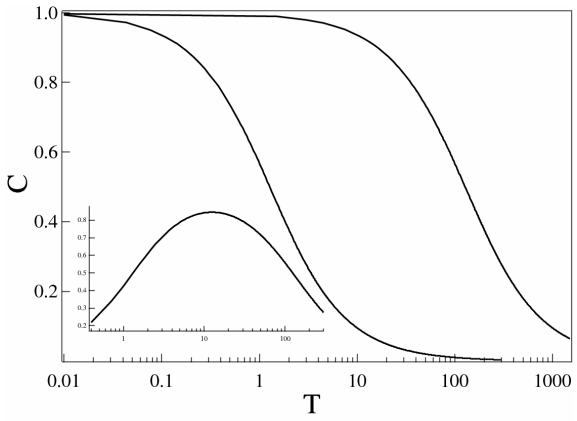

Figure 4.10: *Evolution of the contrast with the camera exposure duration T. The intermediate scattering function is assumed to be a simple exponential, with relaxation time τ evolving during the experiment. Right curve : $\tau \equiv \tau_0 = 100$. Left curve : $\tau \equiv \tau_1 = 1$. Inset : difference between the two contrast curves, $C_{\tau_0}(T) - C_{\tau_1}(T)$ as a function of T. The maximum difference is obtained for a T value approximately equal to the geometric average of τ_0 and τ_1, $\sqrt{\tau_0 \tau_1}$*

As it is evident from this equation, the contrast allows to explore the variations in the particles dynamics when the exposure time T is in the range of the system dynamical timescales. If particle motion accelerates, the contrast will decrease; on the contrary, if the dynamics slow down, the contrast will increase. The exposure duration of the camera device can vary in the range 64 μs $\div$19 ms. When the exposure duration T is varied, the laser intensity is modified in order to keep $\langle I_T \rangle_p$, the average intensity over the pixels, fixed [111].

During the experiment, we chose to keep the exposure duration constant. The optimum choice for T depends on the dynamics of the observed sample. Let us indeed assume that the dynamics of the system is characterized, at a given instant, by a decay time τ of the intermediate scattering function $g^{(1)}$, and that τ may vary, as the system evolves, between τ_0 and τ_1, corresponding to two different values of the contrast, $C_{\tau_0}(T)$ and $C_{\tau_1}(T)$. Assuming that $g^{(1)}$ exhibits a simple exponential decay, the contrast can be calculated as a function of T from equation 4.3: it is plotted for the values $\tau_0 = 100$ and $\tau_1 = 1$ in Fig. 4.10. In order to have a good signal to noise ratio, we wish to observe the maximum variation of the contrast during the experiment. One

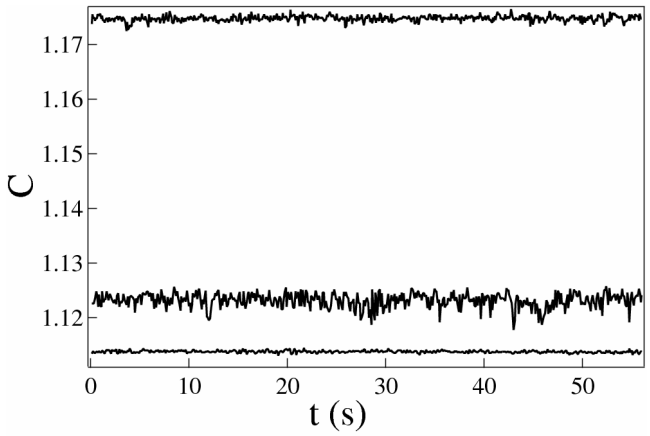

Figure 4.11: *Contrast evolution for a system at rest, for different samples and different camera exposure times T. From top to bottom: silica sphere suspension for $T = 191$ μs, silica sphere suspension for $T = 19.1$ ms and water solution of latex for $T = 19.1$ ms.*

needs to find the value of T that maximizes the difference between $C_{\tau_0}(T)$ and $C_{\tau_1}(T)$. We observe that the maximum difference between the two curves is reached for a time $T = 12$, of the order of the geometric mean of τ_0 and τ_1, $\sqrt{\tau_0 \tau_1}$. This result can be easily generalized, as it doesn't change significantly if we model the decay of the intermediate scattering function by other forms, or if we consider a double decaying correlation function -with one timescale remaining fixed- to account for another dynamical process present in the system at a different timescale. We empirically chose for T the value that maximizes the variation of the contrast during the experiments, and found that $T = 5.08$ ms was the best choice for our system.

SVS on the silica sample

When we monitor the evolution of the contrast in the silica sample at rest, we observe a very noisy signal. This is a consequence of both the properties of the system and our choice of the shutter duration. In order to show that the noise is not due to the setup, but is really an intrinsic characteristic of the sample, we acquire the contrast signal of a water solution of latex, taken for comparison. In Fig. 4.11, we plot the contrast, measured for an exposure duration of the camera $T = 19.1$ ms, for both samples. We calculate the

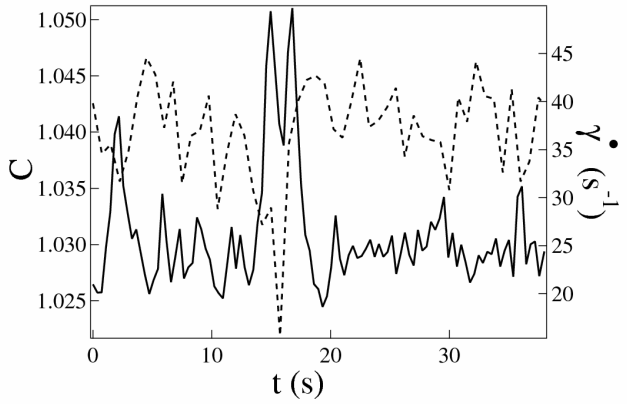

Figure 4.12: *Fluctuations of the gradient (dotted line) and the contrast (solid line) under an applied stress of* 50 *Pa. Low values of the gradient are associated to high values of the contrast.*

relative noise as the ratio between the standard deviation of the signal and the difference between its average value and 1. We obtained a value of 0.011 for the noise of the silica sample and of 0.0035 for the one of the reference sample, which is then a factor of three smaller. For a given sample, the noise of the contrast signal depends on the chosen T. The amplitude of the noise decreases when the exposure time T decreases with respect to the timescale of the system dynamics. For the silica suspension, the relative contrast noise at $T = 191$ μs is smaller by a factor of 4 than the noise at $T = 19.1$ ms (Fig. 4.11). At the shutter duration chosen for the experiment ($T = 5.08$ ms), the amplitude of the noise is similar to the amplitude measured at $T = 19.1$ ms.

Let's now follow the evolution of the contrast while shearing the sample in the jamming regime (we apply a shear stress $\sigma = 50$ Pa). While huge fluctuations are observed in the shear rate, the contrast fluctuates in a correlated manner, as it is evident from Fig. 4.12. When the sample is under shear, the dominant movement of the particles is due to the flow. As evidenced in equation 3.28, the typical timescale characterizing the intensity correlation function thus scales as the inverse shear rate. As a result (see equation 4.3), when the flow velocity decreases due to the shear rate fluctuations in the jamming regime, the contrast will be higher and viceversa.

Part III

Results

CHAPTER 5

Aging dynamics in a shear thinning system

Despite the large amount of numerical and theoretical works investigating the influence of a steady shear flow on the slow dynamics of glassy systems, an experimental microscopic counterpart is still relatively poor. As reported in 1.3.1, evidences for a shear dependent structural relaxation time have been obtained by DWS, but quantitative results are still lacking. Moreover, the statistical properties of multiple scattered light are not easily represented in terms of the particle density correlation function. No attempt has been made up to now to investigate shear influenced dynamics using DLS, which directly probes the intermediate scattering function of the colloidal particles. Through this technique, we begin by monitoring the evolution of the density autocorrelation function when an aging colloidal suspension of Laponite is at rest (5.1). Then, the rejuvenating effect of a steady shear flow on these aging dynamics is investigated following two different protocols. First, we monitor the dynamics while the system ages under shear (5.2). The observed behavior reflects a competition of timescales between the inverse shear rate and the structural relaxation time, as predicted by some of the numerical and theoretical studies discussed in 2.3. A phenomenological model is proposed to interpret the results. Secondly, the effect of the flow on the aging dynamics following shear application is investigated (5.3). Two different regimes

are observed, depending on whether the shear is applied before or after the dynamical arrest (gelation) of the system. The behavior observed before gelation is consistent with the proposed model, while the other regime cannot be interpreted within that framework.

5.1 Standard aging and gelation

We first follow the standard aging evolution of the sample after cell loading. The dynamics is monitored by measuring the intensity correlation function $g^{(2)}(t_w^0, t)$ through the DLS set-up in the homodyne mode, being t_w^0 the time elapsed since sample filtration. The top frame of Fig. 5.1 shows the evolution of $g^{(2)}(t_w^0, t)$, for an evenly spaced set of waiting times t_w^0 spanning the interval $0.1 - 15$ hours. As already observed in Laponite suspensions (see 4.1.1), aging dynamics display a two step relaxation scenario. For the whole set of t_w^0 values reported in Fig. 5.1, a very good fit for the corresponding intermediate scattering functions $g^{(1)}(t_w^0, t)$ is provided by

$$g^{(1)}(t_w^0, t) = f \exp\left[-(t/\tau_s)^\beta\right] + (1-f)\exp\left[-t/\tau_f\right] \tag{5.1}$$

where all parameters (f, τ_s, β, τ_f) depend on t_w^0. The stretched exponential form for the slow relaxation, where $0 < \beta < 1$, can be viewed as the superposition of single exponential decays with a certain distribution $G(\tau)$:

$$\exp[-(t/\tau_s)^\beta] = \int_0^\infty G(\tau)\exp(-t/\tau)d\tau \tag{5.2}$$

The β exponent is closer to one the narrower is the G distribution. Many approaches to slow dynamics in complex systems, as the MCT or the simulated models described in 2.3.4, suggest that such a broad spectrum of time scales arises from the heterogeneous character of slow dynamics [114]. From this broad spectrum, an average relaxation time $\langle\tau_s\rangle$ may be defined in order to quantify the slow decay timescale:

$$\langle\tau_s\rangle = \int_0^\infty \exp[-(t/\tau_s)^\beta]\, dt = \frac{\tau_s}{\beta}\,\Gamma(1/\beta) \tag{5.3}$$

where Γ is the Euler Gamma function. The evolution of $\langle\tau_s\rangle$ and β are reported in Fig. 5.2 (full circles): while the relaxation time increases more than exponentially (as it was also visible from the top inset of Fig. 5.1),

the slow decay becomes very stretched ($\beta = 0.2$). Also the fast relaxation timescale τ_f evolve with t_w^0, exhibiting a slight increasing trend (Fig. 5.9, open squares). This last result seems to be in disagreement with previous observations [92, 96], that showed both the independence of the fast dynamics on the age of the sample and the scaling of the fast relaxation time with q^{-2}. In these previous works, the first decay of the correlation function is interpreted as an evidence of single particle diffusion, while the slow decay accounts for collective dynamics.

For long t_w^0, the slow relaxation of the correlation function will not show a complete decay within the time window explored and the slow relaxation time won't be definable any more. This behavior indicates a strong ergodicity breaking and marks conventionally the crossover to the arrested phase [93]. With the time window accessible in our DLS experiment, gelation takes place in our sample at $t_w^0 \sim 18$ h. A divergent behavior of the slow relaxation time is indeed evident just before gelation in Fig. 5.2.

5.2 Aging under shear

The effect of a steady shear flow on the above described aging dynamics is now investigated by monitoring the intermediate scattering function as the system ages under flow. The competition between the structural relaxation time and the inverse shear rate gives rise to a complex dynamical behavior that we can quantitatively analyze by studying the detailed shape of the measured correlation function. The scenario resulting from this analysis will provide a microscopic counterpart of the strong shear-thinning behavior observed in rheological studies of Laponite and of many other soft materials.

A steady shear rate $\dot{\gamma}$ is applied to the Laponite sample soon after filtration and the correlation functions are collected every time lapse $T_1 = 10$ m in short time intervals $T_0 = 80$ s, during which the rotor is stopped ($\dot{\gamma} = 0$) in order to avoid the decorrelation terms discussed in 3.1.2. By measuring the correlation function at different waiting times t_w since shear cessation, we check that the system is stationary on the timescales of T_0. The robustness of the results with respect to variations of T_1 and T_0 is also checked. The same protocol of measurement is repeated for various $\dot{\gamma}$. Through the heterodyne correlation scheme, we make sure that wall slip and distortion from linearity in the velocity profile are negligible in the whole shear rate range here investigated.

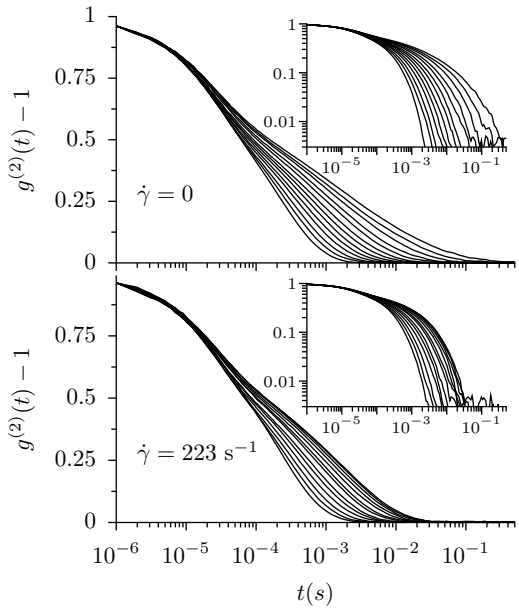

Figure 5.1: *Normalized intensity autocorrelation function for ten equally spaced waiting times between* 0.1 *and* 15 *hours. Top frame refers to aging without shear, while bottom frame refers to aging under shear with* $\dot{\gamma} = 223\ s^{-1}$. *Inset plots show the same data in a double-logarithmic scale.*

In the bottom frame of Fig. 5.1, we report the evolution of $g^{(2)}(t_w^0, t)$, observed on the same set of t_w^0 reported in top frame for standard aging, when a shear rate $\dot{\gamma} = 223$ s^{-1} is applied. Though a stationary state is never reached in the observation time window, for long enough waiting times, the slow relaxation time grows slower than exponentially (the correlation functions come closer in the inset, double-logarithmic plot), while the shape of the relaxation function approaches a constant profile (constant stretching exponent). Equation 5.3 still provides a good fit for all the correlators at the various $\dot{\gamma}$ values here investigated. The presence of a shear induced crossover becomes evident if we plot the fitting parameters $\langle \tau_s \rangle$ and β as a function of t_w^0 for different shear rates (Fig. 5.2). As long as the system dynamics are fast on the timescale $\dot{\gamma}^{-1}$ (indicated by arrows in the plot), non-equilibrium dynamics take place as if shear were not present: both the relaxation time

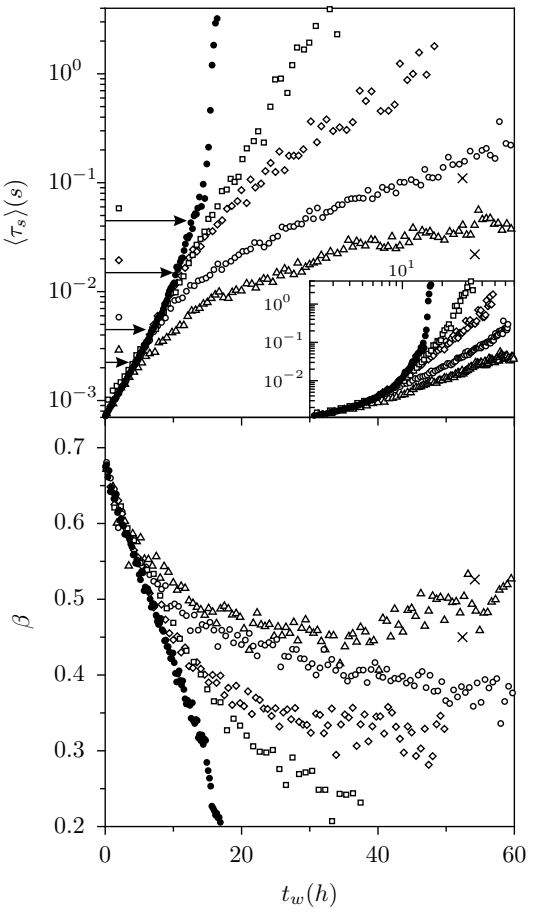

Figure 5.2: *Average slow relaxation time* $\langle\tau_s\rangle$ *and stretching exponent* β *as a function of waiting time* t_w^0*, during aging under different shear rates* $\dot{\gamma}$*:* (△)446, (○)223, (◇)67, (□)22 s^{-1}. *Solid symbols* (•) *refer to aging without shear. Arrows in top frame indicate the* $\dot{\gamma}^{-1}$ *values corresponding to each curve. Inset in top frame shows the same data in a double-logarithmic scale.*

τ_s and the corresponding stretching exponent β evolve with waiting time following the $\dot{\gamma} = 0$ curves (full circles). The presence of shear starts to affect the dynamics as soon as τ_s becomes larger than $\dot{\gamma}^{-1}$: the growth of τ_s is dramatically reduced (even if not completely stopped) and the stretching parameter β behavior flattens.

In the shear dominated region, $\langle\tau_s\rangle$ displays a power law dependence on

t_w^0 (as evidenced in the double logarithmic plot inserted in the top panel of Fig. 5.2), with an exponent which is roughly one for the higher shear rate and increases above unity for lower shear rates. Though aging is never completely absent, the slow relaxation dynamics, for a given waiting time, appears to be very sensitive to $\dot{\gamma}$, being faster and less stretched as $\dot{\gamma}$ increases.

If we suddenly increase $\dot{\gamma}$, rejuvenation is observed leading to faster relaxation time and smaller stretching (higher β). Crosses in Fig. 5.2 are the average relaxation times and stretching exponents of two rejuvenated samples obtained by the two subsequent shear rate jumps: $63\ \mathrm{s}^{-1} \rightarrow 223\ \mathrm{s}^{-1}$ and $223\ \mathrm{s}^{-1} \rightarrow 446\ \mathrm{s}^{-1}$. This sudden rejuvenating effect seems to show that the dynamics only depend on the waiting time t_w^0 and the shear rate $\dot{\gamma}$, while the system doesn't seem to keep memory of the shear history.

Also the fast dynamics seem to be influenced by shear when structural relaxation occurs on a timescale longer than the inverse shear rate. In Fig. 5.3, the left panel shows τ_f vs. t_w^0 for different values of the shear rate, including $\dot{\gamma} = 0$. Similarly to the behavior of τ_s, also τ_f, in the presence of a shear flow, seems to follow the behavior of the $\tau_f(\dot{\gamma} = 0)$ until the *slow* timescale becomes comparable to $\dot{\gamma}^{-1}$. From this time on, τ_f increases slower than in absence of shear. The right panel of Fig. 5.3 better demonstrates this point: when τ_f is plotted against τ_s, all curves tend to collapse, indicating a common origin of the fast and the slow dynamics in Laponite solutions. This result thus seems to refute the interpretation of the fast relaxation as due to single particle diffusion [92, 96]. Recently, the relation between the fast and slow dynamics in Laponite suspensions have been interpreted [112] within the so called coupling model [113].

5.2.1 A phenomenological model

As already reported in other experiments on glassy colloids (which we described in 1.3.1), shear is found to have a deep effect on aging dynamics. Here, we can directly access, through the intermediate scattering function, the particle dynamics resulting from the competition between the highly stretched structural relaxation and the inverse shear rate timescale. In particular, we found that $\dot{\gamma}\tau_s \sim 1$ marks a crossover between an unperturbed and a "shear dominated" aging. In this shear dominated regime, the dynamics becomes strongly depended on the applied shear rate. This shows that, though the shear was temporarily stopped for measuring the intermediate scattering function, the system keeps memory of his dynamics under shear

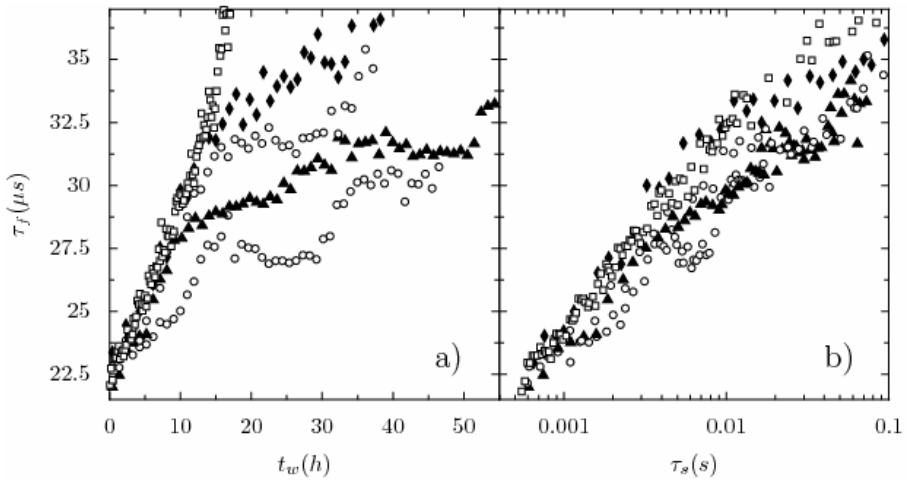

Figure 5.3: *a) Crossover to shear dominated aging as observed in the timescale of fast dynamics τ_f as a function of waiting time; b) all curves collapse when plotted against the respective slow timescale (τ_s) and the crossover disappears.*

during the acquisition. This justifies "a posteriori" the acquisition procedure. We want to stress here that the exponential increase of the slow relaxation time $\tau_s \sim \tau_0 \exp[-t_w^0/\tau_e]$ reveals the presence of at least two well separated intrinsic timescales (τ_e and τ_s) characterizing the aging dynamics of the system. Nevertheless, though the shear rate is always such that $\dot{\gamma}\tau_e \gg 1$, aging dynamics is only affected by shear when the condition $\dot{\gamma}\tau_s \sim 1$ is reached. In order to highlight this result, in Fig. 5.4 we report the values of $\langle \tau_s(\dot{\gamma}, t_w^0) \rangle$ for constant t_w^0 as a function of $\dot{\gamma}$. The grey region represents the half-plane $\langle \tau_s \rangle < \dot{\gamma}^{-1}$, where slow dynamics takes place on a timescale shorter than $\dot{\gamma}^{-1}$. This region is not affected by the presence of shear: the fluid is Newtonian and, similarly to viscosity, $\langle \tau_s \rangle$ is not dependent on $\dot{\gamma}$. On the other hand, shear plays an important role in the complementary half-plane, where $\langle \tau_s \rangle$ displays a strong sensitivity to $\dot{\gamma}$. The non-Newtonian behavior in the upper half-plane of Fig. 5.4 resembles the same $\dot{\gamma}^{-m}$ power law with $m \sim 1$ (dashed line) observed in some rheological measurements of Laponite viscosity [3] and in some theoretical models on glassy systems (which we described in 2.3.2 and 2.3.3).

The whole scenario depicted above provides a microscopic counterpart of the strong shear-thinning behavior observed in rheological studies of Laponite

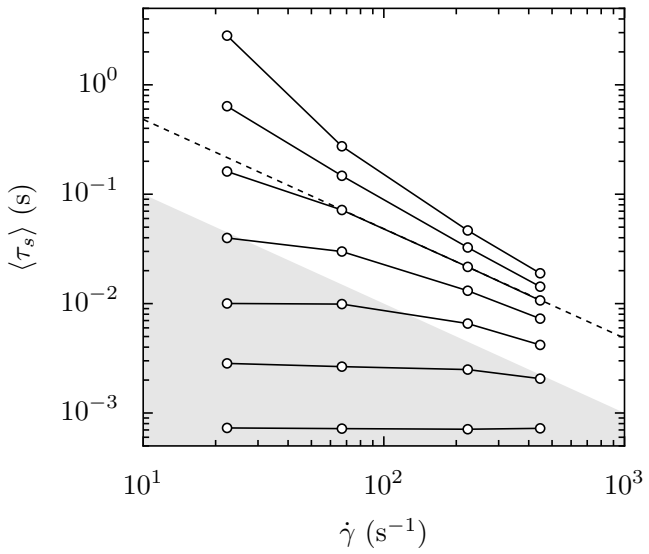

Figure 5.4: *Average slow relaxation time $\langle \tau_s \rangle$ as a function of shear rate $\dot{\gamma}$ for seven evenly spaced waiting times between 0 and 30 hours. Grey area represents the half-plane $\langle \tau_s \rangle < \dot{\gamma}^{-1}$. Dashed line is a fit to a $\dot{\gamma}^{-1}$ power law.*

and of many other soft materials. In the simulated supercooled liquids which we described in 2.3.4 and also in real fluids [1], the viscosity crossover from a Newtonian to a non-Newtonian regime (where a power law dependence on $\dot{\gamma}$ emerges) is usually described by scaling laws such as:

$$\eta(\dot{\gamma}) \simeq \frac{\eta(0)}{1 + \dot{\gamma}\tau_\eta} \tag{5.4}$$

The dynamical analogue of (5.4), suggested by Yamamoto and Onuki in [81], has been reported in equation 2.5, which we rewrite here as:

$$\frac{1}{\tau(\dot{\gamma})} \simeq \frac{1}{\tau(0)} + A\dot{\gamma} \tag{5.5}$$

As can be easily seen in this equation, shear rate provides a parallel relaxation channel to the system which becomes predominant as soon as $1/\tau(0,T) \ll A\dot{\gamma}$. Using the same kind of reasoning, which works remarkably well in the numerical models, one would expect that even in an aging sample, as soon as the unperturbed relaxation time grows large enough, shear rate will fix the

relevant timescale and the system will become stationary even in the non ergodic phases. This is actually what has been observed in the theoretical models described in 2.3 and in the rheological studies on Laponite suspensions (4.1.1).

We are now in the position of testing equation (5.5) by directly investigating the complete time behavior of density dynamics in the presence of a shear flow. At a first glance, one would conclude that Fig. 5.2 is in contradiction with (2.5) and the expectation that shear stops aging. It is indeed evident that relaxation time continues to grow, even if no longer exponentially fast, at least for more than one order of magnitude since it first "feels" the shear field. On the other hand, as shown in Fig. 5.2, when the crossover occurs, the value of the stretching exponent is about 0.5 or less. Assuming a heterogeneous scenario for the distribution of relaxation times, $\langle \tau_s \rangle$ will only represent the average on a broad spectrum of timescales (spanning two decades at least). Therefore, we expect that the shear is effective in interrupting aging only for those timescales growing longer than a fixed, shear dependent, cutoff. In other words we expect that equation (2.5) holds separately for every timescale composing structural relaxation. The above scenario qualitatively accounts for the observations of a slowly growing, though non saturating, structural relaxation time after the crossover. The observed narrowing in the distribution of timescales (larger β) with respect to the unperturbed case is also explained by the model of Yamamoto and Onuki, which predicts an increase of β with $\dot{\gamma}$.

We want to put now the above observations on a more quantitative ground. Assuming that (2.5) holds separately for each timescale, the slow part of the intermediate scattering function (see equation 5.2) can be expressed as

$$g_0^{(1)}(t_w^0, t) = \int_0^\infty G(t_w^0, \tau) \exp[-t/\tau] d\tau \tag{5.6}$$

where G is the unperturbed distribution of timescales. We now expect that shear affects (5.6) as follows

$$\begin{aligned} g_{\dot{\gamma}}^{(1)}(t_w^0, t) &= \int_0^\infty G(t_w^0, \tau) \exp[-t(1/\tau + A\dot{\gamma})] d\tau & (5.7) \\ &= g_0^{(1)}(t_w^0, t) \exp[-A\dot{\gamma} t] & (5.8) \end{aligned}$$

In other words, if we divide the correlation function measured at a given waiting time t_w^0 and shear rate $\dot{\gamma}$ by the corresponding unperturbed ($\dot{\gamma} = 0$)

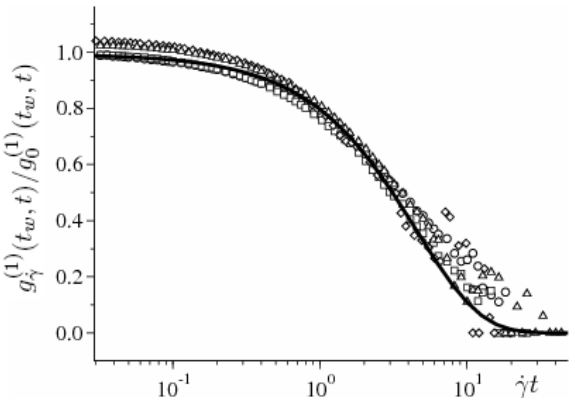

Figure 5.5: *Ratio* $g_{\dot\gamma}^{(1)}(t_w^0,t)/g_0^{(1)}(t_w^0,t)$ *as a function of* $\dot\gamma t$*, where* $g_{\dot\gamma}^{(1)}(t_w^0,t)$ *is the intermediate scattering function measured after a waiting time* t_w^0 *during aging with applied shear rate* $\dot\gamma$*.* $\circ$*:* $\dot\gamma$*=446* s^{-1}*,* t_w^0*=10 h* $\square$*:* $\dot\gamma$*=446* s^{-1}*,* t_w^0*=14 h* $\triangle$*:* $\dot\gamma$*=223* s^{-1}*,* t_w^0*=14 h* $\diamond$*:* $\dot\gamma$*=67* s^{-1}*,* t_w^0*=14 h. Solid line is an exponential fit* $\exp[-A\dot\gamma t]$ *with* $A = 0.22$*.*

correlation measured at the same t_w^0 and plot the result as a function of $\dot\gamma t$, we should obtain the master curve $\exp[-A\dot\gamma t]$. In Fig. 5.5 we report the result of such a procedure obtained for three different values of $\dot\gamma$ and two waiting times. All curves collapse on the same master curve which is well represented by a simple exponential with $A = 0.22$ (solid line). Similarly, we could predict the shape of relaxation for given t_w^0 and $\dot\gamma$ by simply multiplying the unperturbed correlation function for the same t_w^0 by the function $\exp[-A\dot\gamma t]$. If we do this for the $\dot\gamma$ values here investigated and fit the result with a stretched exponential, we obtain a prediction for $\tau_s(t_w^0,\dot\gamma)$ and $\beta(t_w^0,\dot\gamma)$. The results of such a procedure, for those t_w^0 values where $g_0^{(1)}(t_w^0,t)$ is available, are shown in Fig. 5.6 as solid lines. The overall agreement with the directly measured data points (open symbols) is very satisfactory and supports the picture of the slow non-equilibrium dynamics of Laponite as a heterogeneous superposition of relaxing units, each independently coupled to shear through the composition rule for timescales: $1/\tau \to 1/\tau + A\dot\gamma$. We notice that this phenomenological model manages to predict the dynamical behavior of the system through only two parameters: the shear rate and the age of the system. This implies that, at least in the regime here investigated, the dynamics of the Laponite sample is not dependent on the shear history.

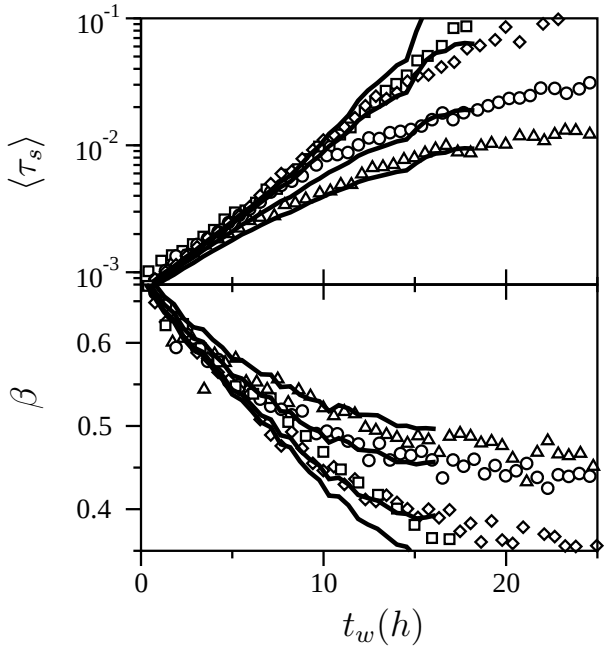

Figure 5.6: *Average relaxation time (top frame) and stretching parameter (bottom frame) as a function of waiting time for different applied shear rates. Symbols are data in Fig. 5.2, solid line is the prediction of the phenomenological model we have proposed.*

5.3 Aging after shear rejuvenation

The shear rejuvenating effect on the dynamics of Laponite suspensions has also been investigated by monitoring the aging evolution which follows the application of a shear flow. Two different aging regimes are observed: one is attained if the sample is rejuvenated before its gelation and one after the rejuvenation of the gelled sample. The standard aging evolution is retraced after shear cessation in the first case, while a completely different regime is attained in the second one, where aging proceeds very fast after shear rejuvenation.

Rejuvenation before gelation

In order to monitor the first regime of aging after shear rejuvenation, we let the sample age until $t_w^0 = 13.4$ h, when the system still has "fluid-like"

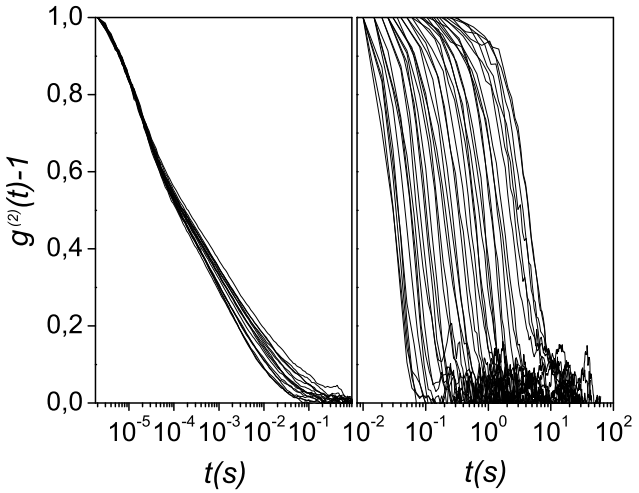

Figure 5.7: *Left: Normalized intensity autocorrelation functions for a Laponite sample rejuvenated before entering the arrested phase. Correlation functions are obtained through classical DLS for 16 equally spaced waiting times t_w^0 between 0.2 and 3 hours (from left to right) since shear cessation. Right: Normalized intensity autocorrelation functions for a gelled Laponite sample for a set of t_w^0 between 0.3 s and 40 s (from left to right). Correlation functions are obtained from the ensemble average procedure described in 4.1.3. The time resolution here is too low to access the fast decay.*

dynamics. Then, we apply a shear rate of 100 s^{-1} for two minutes and finally we follow the dynamics after shear cessation. We define t_w the time elapsed since shear cessation. Aging is monitored through the intensity autocorrelation function $g^{(2)}(t_w, t)$ for a set of t_w between 0.2 and 3 hours, as reported in Fig. 5.7 (left panel). The correlation functions have the same shape observed in the standard aging regime and are still well fitted through the expression of equation 5.1. The stretching parameter β decreases with t_w as shown in the left panel of Fig. 5.8. The evolution of $\langle \tau_s \rangle$ as a function of t_w is plotted in Fig. 5.9 (full circles), where the t_w axis has been shifted by superimposing the first point of the curve on the normal aging curve.

As evidenced in the figure, once a shorter relaxation time is reached by the system after the rejuvenating effect of the shear, the same aging evolution

characteristic of the standard aging is followed. The same behavior can be observed in the evolution of the fast relaxation timescale τ_f, which is plotted in the inset of Fig. 5.9.

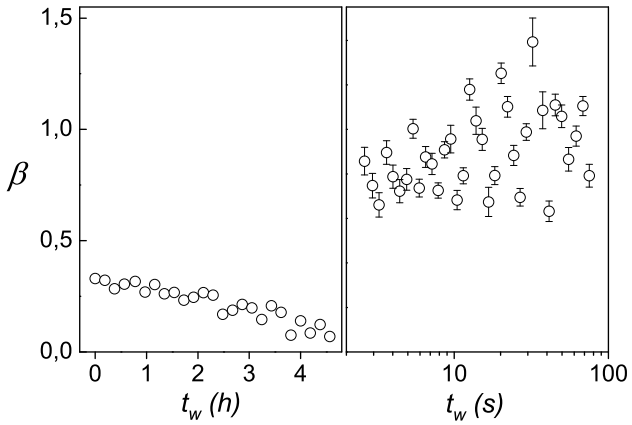

Figure 5.8: *Evolution of the β parameter, deduced from a stretched exponential fit $exp[(-t/\tau_s)^\beta]$ of the intensity autocorrelation function. Left: Aging of a sample rejuvenated before entering the arrested phase. Right: Aging of a rejuvenated gelled sample.*

Rejuvenation after gelation

We now turn to the investigation of the aging evolution after the shear is applied to gelled samples. When a local shear rate $\dot{\gamma}_1$ is applied to the system, the scattered intensity following shear cessation shows the type of evolution reported in Fig. 5.10, where t_w is the time elapsed since flow stop. The fluctuations of the signal display a rapid slowing down within the plot time window. In particular, the fluctuations look stationary if the time is plotted in a logarithmic scale, as shown in the bottom panel of the figure. For such a non-stationary, rapidly evolving dynamics, the intermediate scattering function cannot be measured through classical DLS, where an average over the time origins is performed. Therefore, the dynamics will be monitored by measuring an ensemble averaged correlation function through the method described in 4.1.3.

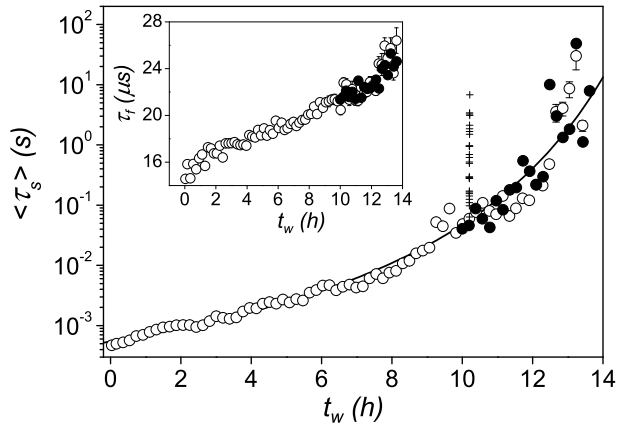

Figure 5.9: *Average slow relaxation time $\langle\tau_s\rangle$ is plotted as a function of waiting time t_w for a sample aging soon after filtration ($\circ$) and for the same sample aging after the application of a shear rate of* 100 s^{-1} *for 2 minutes, 13.4 h after filtration ($\bullet$). t_w is shifted in order to superimpose the first $\langle\tau_s\rangle$ measured after the application of shear with the standard aging curve. Black line is a guide for the eye. The fast aging regime, observed after shear rejuvenation of a gelled sample is also plotted for comparison for the same applied shear rate (+). The curve is shifted in t_w through the above described procedure. Inset: fast relaxation time τ_f as a function of t_w for the two aging evolutions, plotted through the same procedure.*

We first need to point out that gelled samples, when subject to shear, always exhibit wall slip on the static plate (optical window). In particular, when a still, gelled Laponite suspension is put under shear, drastic wall slip takes place and the whole system rotates as a solid body leaving a null shear in the core (measurements of the velocity profile are performed through the heterodyne mode). In order to apply a controlled shear rate, the solid band has to be "broken" through the application of a high shear rate ($\dot{\gamma}_0 >$ 100 s^{-1}). A local shear rate $\dot{\gamma}_1 < \dot{\gamma}_0$ is applied soon after to investigate the aging after-shear dynamics. Another procedure consists in letting the system age under continuous shearing directly at $\dot{\gamma}_1$. Though wall slip is still present at the lower shear rates investigated ($\dot{\gamma}_1 \ll \dot{\gamma}_0$), velocity profiles show a finite local shear rate. We found that, for a given local shear rate, the subsequent aging dynamics is independent on which of the two described protocols is

applied, confirming the independence of the sample dynamics on the shear history. In the following, we will always refer to samples prepared according to the first procedure.

With an initial shear rate $\dot{\gamma}_0 = 200$ s^{-1} of the duration of two minutes, various experiments at different $\dot{\gamma}_1$ are performed. The measuring protocol described in 4.1.3 is followed, with parameters $T_1 = T_0 = 120$ s and $dt = 10^{-2}$ s. The time resolution, which is fixed by dt, has been chosen in order to let us follow the slow dynamics, while limiting the time spent in the computation of the correlation functions (the number of counts for each acquisition is given by the ratio T_0/dt). In order to minimize inertial effects due to flow stop, the shear rate $\dot{\gamma}_1$ is set to zero through a decreasing ramp of the duration of 10 s. The whole measurement lasts about 24 hours. The resulting intensity autocorrelation functions $g^{(2)}(t_w, t)$ for a set of waiting times between 1 and 40 s are reported in Fig. 5.7 (right frame). The time resolution of the correlation functions is too low to reveal the fast dynamics of the system. As evidenced in 5.2, we may expect that the system ages during the experiment, due to the long acquisition time. However, if we calculate the correlation functions by taking only the first or last group of acquired counts, we obtain the same results, showing that aging is negligible.

Compared to standard aging, the new aging regime entered by the rejuvenated gelled sample is characterized by intensity correlation functions of a different form and by a much more rapid evolution of the slow relaxation time with t_w (Fig. 5.7). The corresponding intermediate scattering functions are first fitted by a stretched exponential decay. The stretching parameter β now statistically fluctuates around one and doesn't seem to depend on the waiting time (Fig. 5.8, right panel). For a given t_w, the slow relaxation time is then obtained as the value τ_s satisfying the condition: $g^{(1)}(\tau_s, t_w) = 0.5$. Results are checked to be consistent with other fitting procedures. The obtained curves of τ_s vs t_w for various $\dot{\gamma}_1$ in the range $6 \div 134$ s^{-1} are reported in Fig. 5.11. A plateau is evident at short t_w, while a power law behavior is found at longer t_w: $\tau_s \sim t_w^c$. No significant difference is observed in the aging evolution as the applied shear rate varies in the range here investigated. In particular, the slow relaxation time soon after flow stop can be quantified by the plateau value, which doesn't show any dependence on $\dot{\gamma}_1$. The two regimes of aging investigated are compared by adding, in Fig. 5.9, the plot of the slow relaxation time evolution in this second regime: aging is so fast that the curve seems to diverge instantaneously with the time resolution fixed by the first regime.

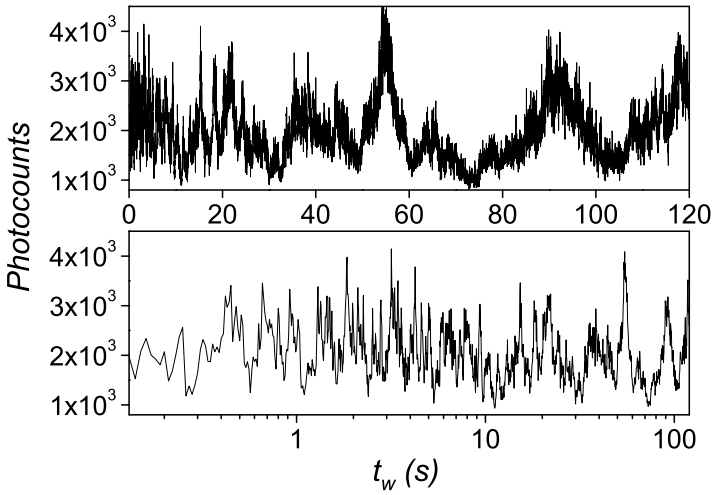

Figure 5.10: *Fast slowing down of the scattered intensity fluctuations with the waiting time for a rejuvenated gelled Laponite sample. Top: the evolution of the counts revealed by the photomultiplier in* 10^{-2} *s soon after shear cessation is plotted,* $t_w = 0$ *corresponds to the shear stop. Bottom: log-linear plot of the counts evolution; a logarithmic binning of* t_w *has been performed and the counts have been averaged in each bin.*

5.3.1 Discussion

Once the shear is applied before gelation of the sample, a reduced relaxation timescale is observed soon after shear stop. This starting value is predictable by the phenomenological model proposed in 5.2. Indeed, the slow relaxation timescale of the system at a given shear rate $\dot{\gamma}$ and waiting time t_w^0 can be determined through the model once we have measured the intermediate scattering function at t_w^0 during the standard aging. In particular, by integrating the slow part of the intermediate scattering function, for a given t_w^0 we obtain (from equation 5.7)

$$\langle \tau_{s\dot{\gamma}} \rangle = \int_0^\infty \exp[-(t/\tau_{s0})^{\beta_0} - A\dot{\gamma}t]\, dt \tag{5.9}$$

where τ_{s0} and β_0 are intended for the standard aging evolution. At $t_w = 13.6$ h, just before the shear rate is applied to the sample, we have $\tau_{s0} \sim 1.5\ 10^{-2}$

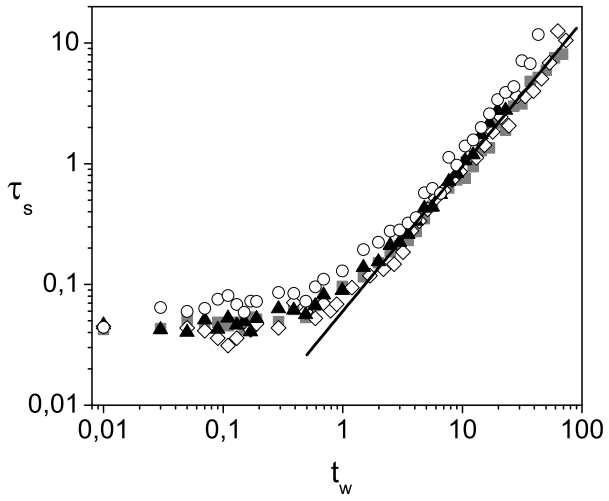

Figure 5.11: *Aging after rejuvenation of a gelled Laponite sample. The evolution with t_w of the slow relaxation time τ_s is plotted for various applied shear rates $\dot{\gamma}_1$: ($\diamond$) 6 s^{-1}, ($\square$) 28 s^{-1}, ($\triangle$) 66 s^{-1}, ($\circ$) 134 s^{-1}. The curves doesn't show significant variations for the different $\dot{\gamma}_1$. Bold line is a fit to a $t_w^{-1.2}$ power law.*

and $\beta_0 \sim 0.15$. From a numerical calculation, the right part of equation 5.9 can be plotted as a function of $\dot{\gamma}$ (Fig. 5.12). The average relaxation time measured after the application of a shear rate $\dot{\gamma} = 100$ s^{-1} is in good agreement with the value predicted by the model. The following evolution of the relaxation times (both fast and slow) is observed to trace the same aging curves exhibited during the standard aging, showing that aging is reversible in this regime and true rejuvenation is achieved through shear flow.

After shear rejuvenation of a sample in the arrested phase the system dynamics is no longer reversible: the aging process that has induced the arrested phase can't be reached again through shear rejuvenation, and a completely different regime is reached. The intensity correlation function characterizing the dynamics in this new regime exhibits a simple exponential decay, differently to what happens in the other regime. The approximate scaling of the slow relaxation time as the inverse shear rate, suggested by the phenomenological model and by the schemes usually applied to glassy systems, is no longer valid. On the contrary, in the range of shear rates here

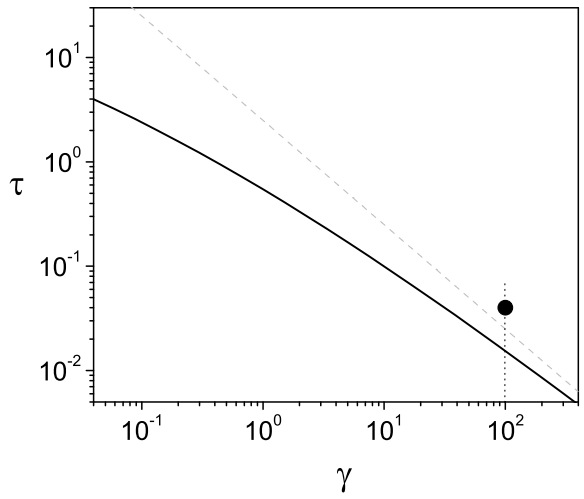

Figure 5.12: *Behavior of the average slow relaxation time at $t_w = 13.6$ h as a function of the applied shear rate, as expected from the proposed phenomenological model. The time $\langle \tau_s \rangle$ measured after the application of a shear rate $\dot{\gamma} = 100$ is also plotted, showing to be compatible with the expected value. Grey line is a fit to a $\dot{\gamma}^{-1}$ power law.*

investigated (spanning more than one decade), the slow relaxation time after flow stop doesn't seem to depend on the applied shear rate. Therefore, at the lower shear rates, the flow exhibits a surprisingly strong rejuvenating effect, with the slow relaxation timescale getting shorter than the inverse shear rate after flow stop. Then, the system quickly ages back to the arrested state. After a plateau region (evident in a logarithmic plot), a power-law dependence of the slow relaxation time with waiting time is observed for long t_w, with exponent $c \sim 1.2$. Such a behavior (with two different regimes for short and long t_w) has already been observed after rejuvenation of other colloidal glasses [6]. In other clay suspensions similar to Laponite, a power law behavior of τ_s *vs* t_w, with exponent close to one, has been observed after shear rejuvenation of aged samples [7, 97]. However, we couldn't find for these systems any information in the literature about normal aging, or aging after rejuvenation of young samples. It would be interesting to find out whether a different, slower aging process is observed in these regimes, as it happens in Laponite suspensions, and if the described phenomenology can be generalized to charged discoidal colloids. Finally, the same power

law behavior has also been observed during the standard aging of Laponite suspensions at very long waiting times [96].

The phenomenology described above for the second regime of aging is not well understood. If the arrested phase at the concentration here investigated corresponds to a glassy phase, the observed behavior of the slow relaxation time as a function of the shear rate would be totally unexpected. Actually, a debate on the arrested phase of Laponite suspensions is still open [89, 90, 94] and it is not clear yet whether a gel phase or glassy phase occur in the system. The unexpected scaling of $\tau_s(t_w \rightarrow 0)$ with $\dot{\gamma}$ and the following rapid aging evolution may thus be interpreted through the formation of a gel, characterized by the existence of a fractal network [89]. In this context, Ref. [115, 116] suggest that the decorrelation of the scattered light wouldn't be due to the dynamics of single scatterers, but to a drift mechanism of aggregates of particles due to micro-collapses of the structure.

CHAPTER 6

Shear localization in a glassy suspension

Over same range of shear rates, a shear localization phenomenon may be observed in soft glassy materials: the flow separates into bands parallel to the flow direction, with a sheared region coexisting with a completely steady region (zero shear rate). As explained in 1.3.3, this behavior is due to the presence of a yield stress, which induces a multivalued flow curve, and may be accompanied by a stick-slip behavior, as observed in a few experiments already described. From a theoretical point of view, these behaviors are predicted by the phenomenological Maxwell model (2.3.3) and by the numerical model for glassy systems presented in 2.3.4, where a different dynamics is observed in the two bands: in the unsheared band the system is arrested, while in the sheared region a liquid-like behavior is exhibited. At the experimental level, due to the difficulty in investigating the system dynamics under shear, this difference in the dynamics hasn't been evidenced yet.

In our experiments, we apply a low global shear rate $\dot{\Gamma}$ (in the range $0.5 \div 5\ \mathrm{s}^{-1}$) on a Laponite suspension and we observe the occurrence of shear localization through the heterodyne correlation scheme. To begin with, the evolution of the flow velocity profile have been monitored under a constant applied shear rate (6.1).Periodic oscillations of the velocity profile are observed in very old samples: this stick-slip phenomenology is described in 6.2.

Some preliminary results in monitoring the dynamics in the two bands are also presented (6.3).

6.1 Velocity profile evolution

For glassy colloids, as soon as the system ages under shear, we expect the flow curve to evolve with t_w, as exemplified by the rheological measurements on Laponite suspension reported in Fig. 6.1. As suggested by equation 5.4, the curves are well fitted through the form $\sigma = \eta_0\dot{\gamma}/(1+(\tau_\eta\dot{\gamma})^\alpha)$. The fit parameters are plotted in 6.2. We also expect that aging proceeds unperturbed in the unsheared region and thus the yield stress increases with t_w [17]. As a consequence, the regime of shear localization will extend to higher applied shear rates $\dot{\Gamma}$ (see Fig. 2.5). At the same time, a slower aging takes place in the sheared band and will induce an evolution of the fluid velocity profile with t_w in the range of $\dot{\Gamma}$ where shear localization occurs. At a fixed t_w, the

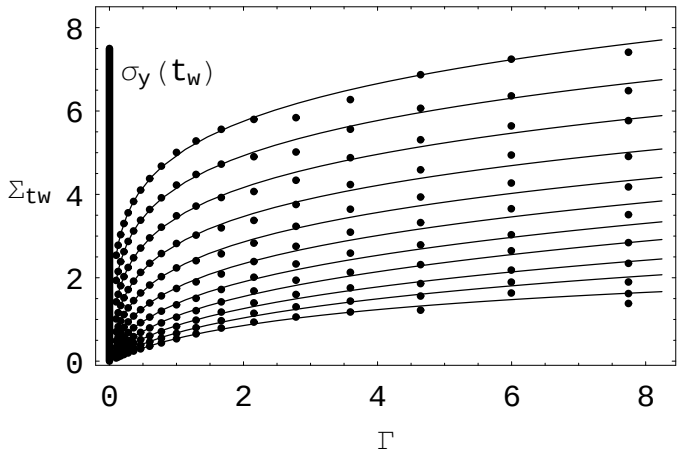

Figure 6.1: *Qualitative behavior of the flow curves for a Laponite suspension. The sample here has a higher concentration than the one used in the other experiments and aging is faster. The curves are equally spaced in time in the range of waiting times* $400 \div 530$ *s after sample filtration [117]. The curves are fitted through the form* $\sigma = \eta_0\dot{\gamma}/(1+(\tau_\eta\dot{\gamma})^\alpha)$. *The presence of a yield stress is expected, with an increasing behavior with* t_w *[118]. Its qualitative behavior is marked to show that the flow curve is expected to be multivalued.*

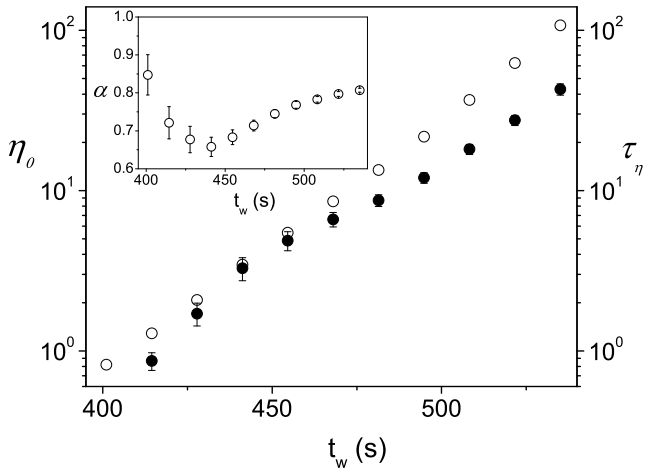

Figure 6.2: *Fit parameters of the curves plotted in Fig. 6.1 as a function of the waiting time t_w. •: τ_η, ○: η_0.*

problem of determining the flow behavior reduces to the determination of the following variables: the shear stress σ, which is constant across the gap in a plane Couette flow (as in the plate-plate or cone-plate geometry used in our experiments) and the local shear rate in the liquid band $\dot{\gamma}_{loc}$. In our experiments, we can access $\dot{\gamma}_{loc}$ through the direct measurement of velocity profile. We made an attempt to access the stress σ by measuring the tension dissipated by the motor that induces the cone rotation. However, we didn't manage to obtain a high enough resolution and neither a qualitative behavior of the stress could be accessed.

The three variables determining the flow behavior are related through the following equations:

$$d/h = \dot{\Gamma}/\dot{\gamma}_{loc} \tag{6.1}$$

$$\sigma = \eta_{\dot{\gamma}\neq 0}\dot{\gamma}_{loc} \tag{6.2}$$

where $\eta_{\dot{\gamma}\neq 0}$ is the fluid phase viscosity. Knowing the flow curve $\Sigma = \Sigma(\dot{\Gamma})$ (for the global variables), there will still be one equation missing to solve the system and predict the flow behavior. This problem has been faced from

a theoretical point of view in Ref. [119]. The authors first try to provide a constraint by the equality of some thermodynamic variable for the two phases, generalized for the out of equilibrium condition of the fluid band. However, they found that there exists no physically reasonable definition for such a variable and conclude that the coexistence of two phases cannot be accounted for by invoking thermodynamic arguments. On the contrary, the underlying principle governing this non-equilibrium coexistence is found in the balance between the growth of the unsheared phase and the surface erosion by the shearing liquid.

The qualitative evolution expected for the flow velocity profiles is observed when we monitor a Laponite suspension aging under a low applied shear rate ($\dot{\Gamma} = 0.65\ s^{-1}$). In both the plate-plate or cone-plate geometry, the flow velocity profile evolves as reported in Fig. 6.3. A solid band thus nucleates on the stationary wall (due to the interaction with the cell wall, the solid band is expected to form at the boundary), but the local shear rate is observed to vary continuously across the gap and there is not a sharp distinction among the solid and the fluid bands.

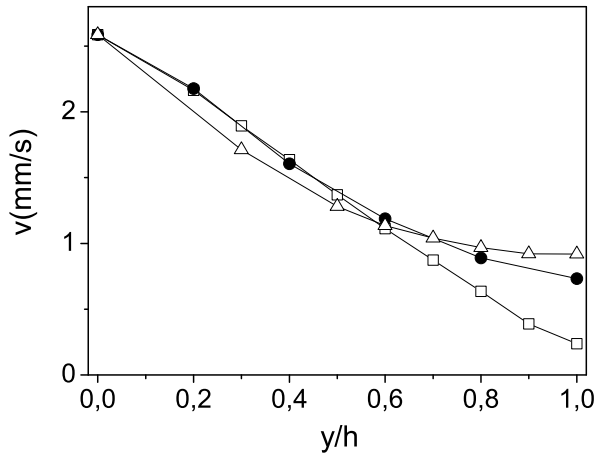

Figure 6.3: *Evolution of the velocity profile in a cone-plate geometry (with non metal walls). A global shear rate $\dot{\gamma} = 0.65\ s^{-1}$ is applied since sample filtration and the profiles are collected at the following t_w: 24 h (□), 46 h (•) and 70 h (△). As the cone velocity fluctuates during the experiment, the three profiles are normalized at $z/y = 0$ to be better compared.*

6.1.1 The wall effect

On a practical ground, the shear localization phenomenon may also be enhanced, or completely induced by the inhomogeneity of the sample due to its interactions with the walls [51] of the measuring device. This problem, though apparently very specific, is often encountered in the experiments and has also inspired a theoretical work by Ajdari [120].

Some of our experiments in the cone-plate geometry were performed with a metal cone in the shearing cell (a thin insulating layer covers instead the metal cone in all the experiments reported in the other sections). In order to investigate the effect of the metal wall on the shear localization phenomenon, we have monitored the evolution of the velocity profiles (through the heterodyne correlation scheme) for various protocols of the applied shear rate. When a low shear rate ($\dot{\gamma} = 0.56$ s^{-1}) is applied to the sample soon after filtration, shear localization is already observed after a few minutes have passed. The unsheared band then enlarges until wall slip at the static plate appears and another unsheared band forms on the static plate (Fig. 6.4). Contrarily to the evolution of the velocity profile observed when the interaction between the wall and the sample is negligible (Fig. 6.3), here the band forms next to the cone and enlarges very rapidly due to the interaction between the metal wall and the sample. Another protocol we have used consists in monitoring the evolution of the velocity profile while varying the applied shear rate. Once a shear banding profile similar to the one reported in Fig. 6.3 for $t_w = 162$ min is reached (at an applied shear rate $\dot{\gamma} = 0.90$ s^{-1}), we increase the applied shear rate and obtain the profiles reported in Fig. 6.5. As it is evident from the inset, the width of the unsheared band doesn't vary with the applied shear rate.

These results suggest that a heterogeneity is induced in the system along the gap by the metal wall of the cell, with the dynamics slowing down as the cone is approached (as confirmed by a scan of the intermediate scattering function along the gap). At contact with the aqueous suspension, the metal wall may indeed release ions in solution, inducing a high ionic strength in the vicinity of the cone and thus accelerating the aging dynamics [93]. As a consequence, the evolution of the flow curve (as sketched in Fig. 6.1) will proceed more rapidly near the cone than near the static plate and, in particular, the growth of the yield stress with t_w will be very fast in the vicinity of the cone. Therefore, at long t_w, the flow curve will present a multivalued region extending to very high shear stresses (see Fig. 2.5). Among the

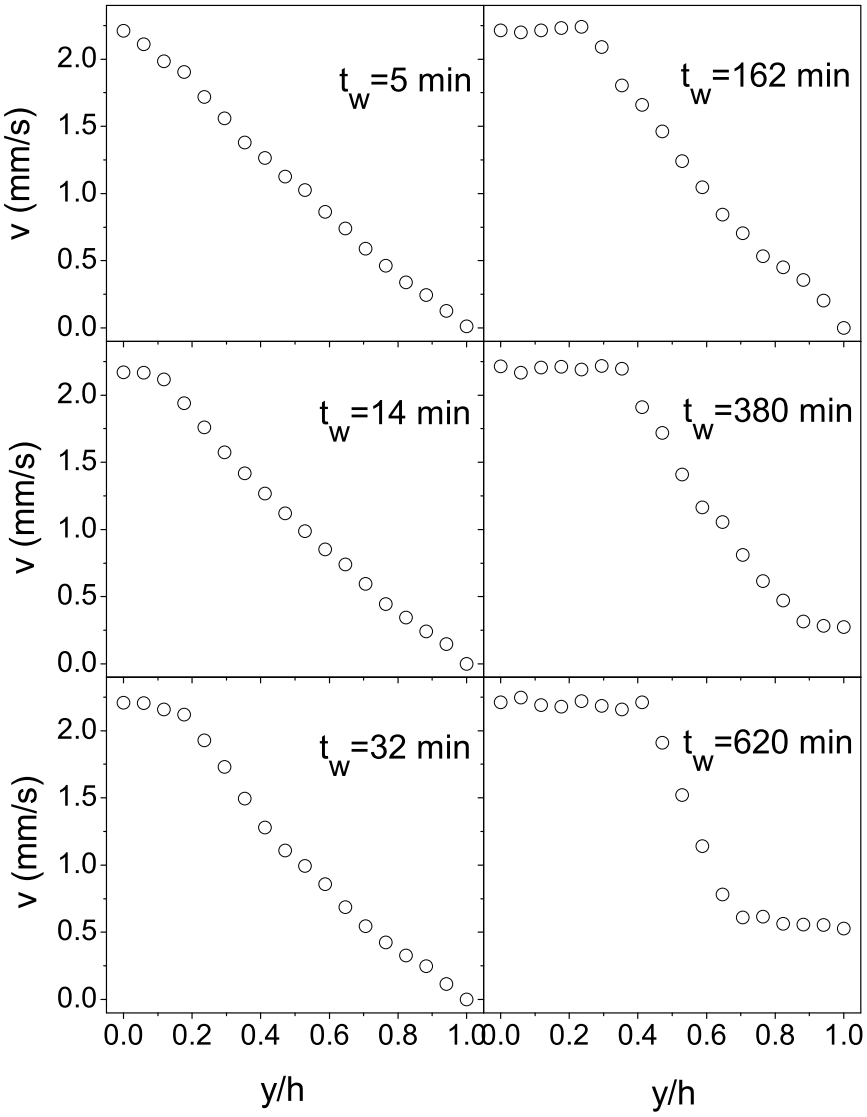

Figure 6.4: *Evolution of the velocity profile in a cone-plate geometry with metal walls. A global shear rate* $\dot{\gamma} = 0.56\ s^{-1}$ *is applied since sample filtration.*

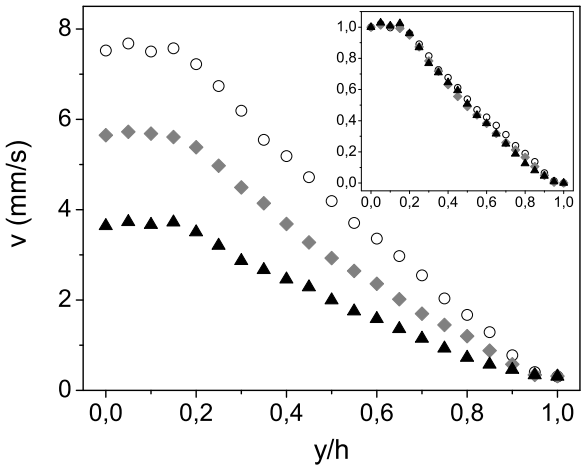

Figure 6.5: *Velocity profiles at various global applied shear rates in a cone-plate geometry with metal walls:* $\dot{\gamma} = 0.9\ s^{-1}$ *(▲),* $\dot{\gamma} = 1.4\ s^{-1}$ *(◇),* $\dot{\gamma} = 1.9\ s^{-1}$ *(○). In the inset, the profiles are normalized at* $z/y = 0$.

variables describing the flow behavior of the system, we can experimentally access the local shear rate $\dot{\gamma}_{loc}$ and the width d of the liquid band. On the contrary, we can't access the stress value σ in our experiments. However, we can qualitatively interpret the observed evolution of the velocity profiles by looking at the evolution of the flow curves sketched in Fig. 6.1. The evolution of the velocity profiles at a constant global shear rate (Fig. 6.4) reflects the aging dynamics of the system: as the viscosity of the system increases with t_w, the stress also increases but keeps smaller than the yield stress. The observed widening of the unsheared band with t_w may be interpreted within this scenario. At a fixed t_w, if we knew the particular behavior of the flow curve, the stress of the system would be obtained from the intersection of the measured $\dot{\gamma}_{loc}$ of the fluid band with the flow curve. From the qualitative evolution of the flow curve and from the observed increase of $\dot{\gamma}_{loc}$ with t_w, we can infer that the points in the Σ-$\dot{\Gamma}$ plot describing the state of the system in the fluid band evolves as sketched in Fig. 6.6. The independence of the band width on the applied shear rate (Fig. 6.5) may instead be due to the shape of the flow curve: as it is visible in Fig. 6.1, at long enough shear rates, a large increase of the shear rate induces only a slight increase of the

stress. The independence of the shape of the velocity profile on the applied shear rate may be due to the fact that the measurements take place in such regime of the flow curve.

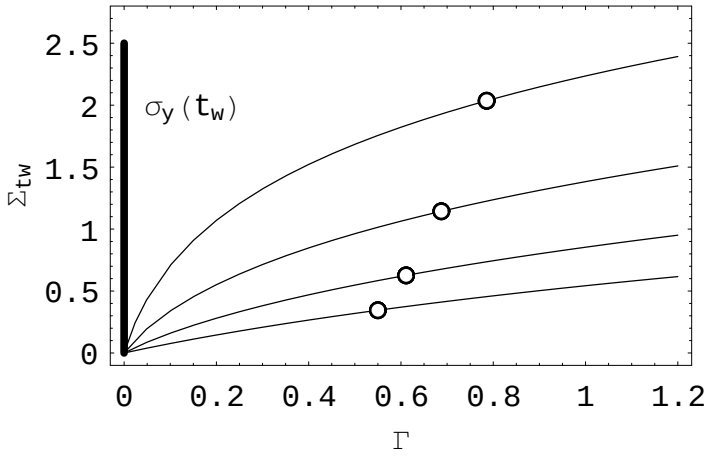

Figure 6.6: *Schematic representation of the state of the system in the fluid band (open circles) as the waiting time evolves in the geometry with metal walls.*

6.2 Oscillations of the shear banding profile

One of the few experiments where shear localization and stick-slip behavior are observed in a glassy system was performed on Laponite suspensions in a cone-plate geometry, with a visualization technique [19]. In such experiment, the applied shear rate is very small ($\dot{\Gamma} \sim 10^{-4}$) and the stick-slip behavior is observed at the interface of two solid bands in the bulk of the cell, with a time period that is much smaller than the rotation period of the cone. We want to investigate deeper this phenomenology in a higher range of shear rates and with the advantage of using heterodyne dynamic light scattering, which allows much more accurate measurements of the fluid velocity profile with respect to the rough visualization technique used in [19].

When a shear rate in the range $0.5 \div 5$ s^{-1} is applied to old Laponite samples in a cone-plate or plate-plate geometry, a stick-slip behavior is often observed. The results that we are going to present not only confirm the prediction of some phenomenological and numerical models on glassy systems

(presented in 2.3.3 and 2.3.4), but also show a more complex behavior of the oscillations in the flow velocity profiles. As this part of the work is purely phenomenological, we will simply describe the observed behavior by reporting the plots of the oscillating flow velocity with some brief comments.

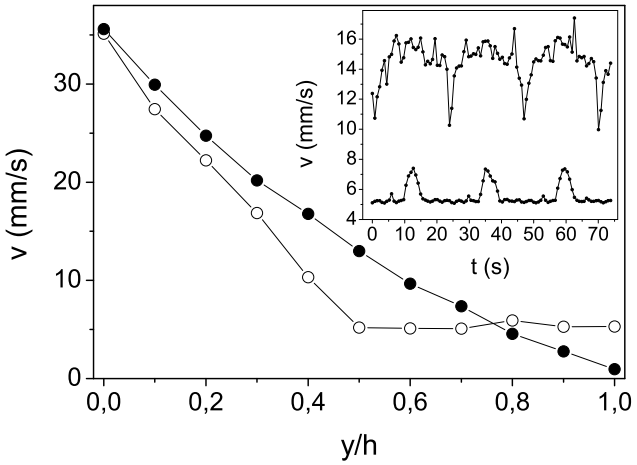

Figure 6.7: *The velocity profile oscillates between the two extreme profiles plotted in the figure with a time period $T \simeq 23$ s. In the inset, the oscillations of the particle velocity when the scattering volume is at $z/H = 0.4$ (top) and $z/H = 0.7$ (bottom) are plotted. These periodic oscillations of the particle velocity are only observed far from the cone ($y/h > 0.2$). The small and fast oscillations visible in the bottom curve of the inset have the same period of the cone rotation $T_{rot} \simeq 4$ s. They are due to a slight misalignment of the rotational axis (with respect to the orthogonal to the window plate), which induces a small oscillation of the gap width ($\sim 8\%$).*

In a plate-plate geometry (where the gap width is $h = 8$ mm), periodic oscillations of the velocity profile was observed when a shear rate $\dot{\Gamma} = 4.5\ \mathrm{s}^{-1}$ was applied to a old Laponite sample. The oscillation period is larger than the cone rotation period and remains constant on the timescale of the hours. By looking at the particle velocity oscillations in different positions along the gap, it is evident that the velocity profile oscillates among a configuration where the shear is localized on the rotating plate side and a configuration with a linear profile (Fig. 6.7). Most of the time, the system lies in an

intermediate profile between the two. When the linear profile is reached, the system will have a liquid-like behavior: it sticks on the wall and has a low yield stress (the flow curve won't be multivalued at the applied shear rate $\dot{\Gamma}$). On the contrary, in the instants when shear localization occurs, we expect that an arrested phase characterizes the solid band, which will have a high yield stress and slips on the wall.

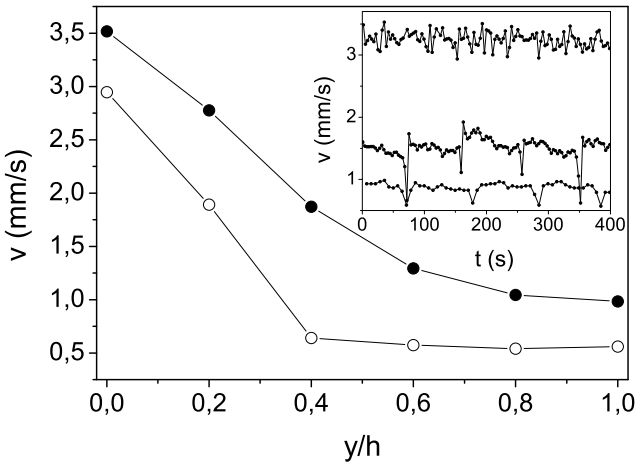

Figure 6.8: *The velocity profile oscillates between the two extreme profiles plotted in the figure. Most of the time, it coincides with the upper profile, as it is visible in the inset, which shows the oscillations of the particle velocity at $z/H = 0.4$ (central curve) and $z/H = 1$ (bottom curve). The period of the oscillation slightly varies among the two curves as the data are acquired at a time distance of 3 h. The top curve of the inset represents the evolution of the cone velocity. The periodic oscillations of the particle velocity are only observed far from the cone ($y/h > 0.2$).*

In a cone-plate geometry, periodic oscillations of the velocity profile was observed when a shear rate $\dot{\gamma} = 0.8\ \mathrm{s}^{-1}$ was applied to a old Laponite sample. In this regime, the cone rotation velocity is found to fluctuate very much ($\sim$ 15%). Now the flow doesn't oscillate between a linear and a shear localization profile (Fig. 6.8). However, in this configuration, we investigated the particle velocity oscillations at fast timescales and a very interesting phenomenology is observed. By reducing the acquisition time to $4\ 10^{-2}$, we monitor the evolution of the cone velocity and particles velocity in the vicinity of the

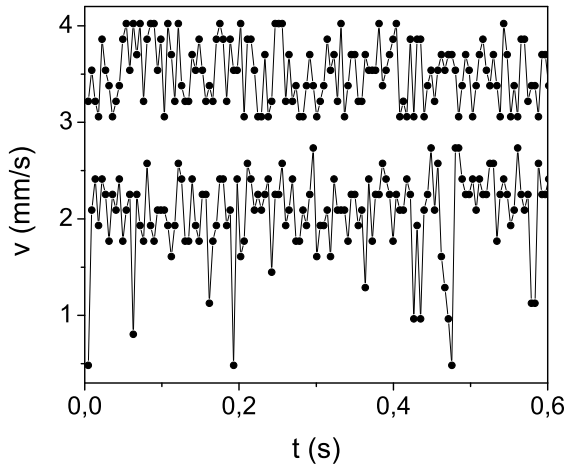

Figure 6.9: *Very fast fluctuations of the cone velocity (top curve) and of the particle velocity at $z/h = 0.2$ (bottom curve). The minimum value reached by these fluctuations corresponds to the plateau value of the minimum velocity profile plotted in Fig. 6.8.*

cone (Fig. 6.9). The latter fluctuates much more than the cone velocity and is observed to reach the plateau value of the minimum velocity profile plotted in Fig. 6.8, as if a unique solid band forms across the whole gap and rapidly fractures. Another interesting observation shows up when an intermediate acquisition time is chosen ($\sim 2\ 10^{-1}$): far from the cone, periodic oscillations of the particle velocity shows up (Fig. 6.10). These oscillations have about the same amplitude of the ones observed in Fig. 6.8, but now the period is more than one order of magnitude smaller (is now smaller than the cone rotation period) and strongly fluctuates.

6.3 Measuring the dynamics

We will now present some preliminary results on the detection of the dynamics underlying the two phases observed in the shear localization regime. The dynamics is monitored soon after shear cessation through the ensemble average procedure described in 4.1.3. As observed in the experiment described

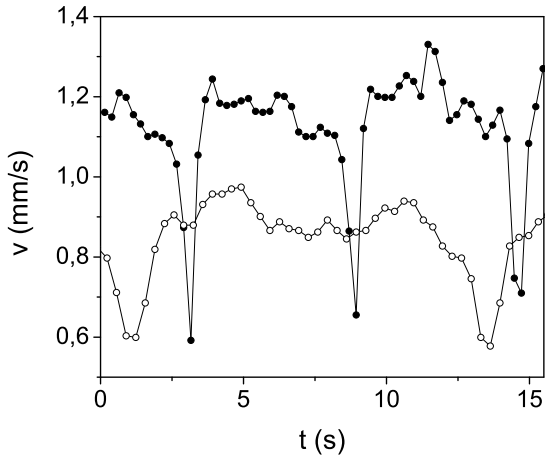

Figure 6.10: *Fast oscillations of the particle velocity at $z/h = 0.6$ (•) and $z/h = 1$ (○). Again, these oscillations are only observed far from the cone ($y/h > 0.2$), but their period fluctuates enormously with time.*

in 5.3, the aging evolution soon after shear cessation is slightly dependent on the applied shear rate for old Laponite samples. However, we expect that the rejuvenating effect of the flow disappears in the unsheared band, where the shear rate is zero. If we thus measure the aging dynamics after flow cessation in the two bands, we expect a different evolution of the slow relaxation time. As even a low shear rate may instantaneously rejuvenate the system in the solid phase, great accuracy have to be spent to keep the shear rate continuously null in the arrested phase. During the measuring protocol, it is thus necessary to set the applied shear rate to zero through a decreasing ramp. This allows to avoid that transient shear rates rise during flow stop due to inertia of the flowing sample while the rotor is stopped.

In a cone-plate geometry, we first follow the evolution of the slow relaxation time after shear cessation when the whole system rotates as a solid body (such condition is easily obtained when a shear rate is applied to a gelled sample). Compared to the results obtained in 5.3 when the system flows at a finite local shear rate, the slow relaxation is about two orders of magnitude larger 6.11. Though an unexpected rejuvenating effect of the flow emerges, this result shows that a much slower dynamics characterizes the system. Now, we would like to obtain the same result in the shear localization regime. Once the velocity profile reported in Fig. 6.11 (right panel, squares)

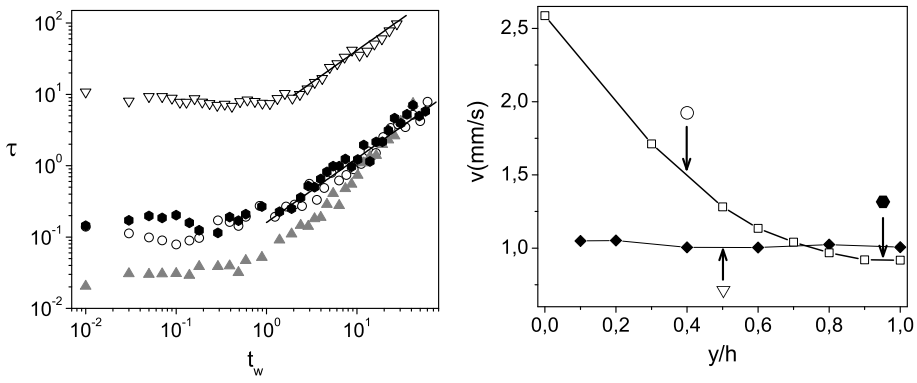

Figure 6.11: *Evolution of the slow relaxation time τ soon after shear cessation, measured through the procedure described in 4.1.3 for various local shear rates and velocity profiles. The velocity profile and the position of the scattering volume during the various measurements are represented in the right plot. For comparison, we added the evolution of τ ($\triangle$) for a much higher shear rate ($\dot{\gamma} = 134\ s^{-1}$), for which the velocity profile was linear.*

is reached, we monitor the dynamics in the solid phase ($y/h = 0.95$) and in the fluid phase ($y/h = 0.40$). Actually, no significant difference is observed in the aging evolution after shear cessation. This may be due to the fact that the unsheared band is too thin and some component of the velocity field vector may induce a finite shear rate in this region. Repeating the measurement in a different configuration, characterized by a larger unsheared band, may be a possible solution.

CHAPTER 7

Relaxation of aggregates in a shear thickening system

In concentrated colloidal suspensions, the shear thickening regime is believed to be induced by the formation of aggregates of particles, as we evidenced in 2.5. However, investigation of the particle microstructure during the flow displays many difficulties at the experimental level and the scenario depicted by the experimental works proposed in the literature (see 1.3.2) is still not exhaustive. In particular, investigation on the dynamics of these shear induced aggregates is still lacking. Through speckle visibility spectroscopy, we monitored the dynamics of a concentrated suspension of silica particles in the jamming regime (see 4.2) and we follow the relaxation of the shear induced aggregates after shear cessation as a function of the applied shear stress.

7.1 SVS measurements on the jamming silica sample

While the suspension is continuously illuminated by the laser beam, we apply a high shear stress (in the jamming regime) to the silica suspension and, after a given time, stop the stress application. We observe that the dynamics of the particles during the jamming regime may even be slower than the dynamics

at rest. In Fig. 7.1, we report the evolution of the contrast when a shear stress $\sigma = 255$ Pa is applied for 30 s. As soon as the stress is applied, the contrast value drops; after a while, the suspension jams and huge contrast fluctuations occur. Soon after shear cessation, we observe an overshoot of the contrast, which then slowly decreases to a constant value, that is not necessarily the same value it had before the shear. During the flow, the signal fluctuations lead to contrast values higher than the value at rest before or after the stress application. At these instants, the particle drift velocity must be very slow, due the huge fluctuations of the shear rate. Thus, the timescale dominating the dynamics is not due to the drag motion and another dynamical timescale can be revealed. The peaks observed in the contrast during the flow show that the dynamics characterized by this sometimes emerging timescale is slower than the dynamics of the system at rest. The particles thus organized themselves under flow in such a way that their motion is slower than their free motion at rest.

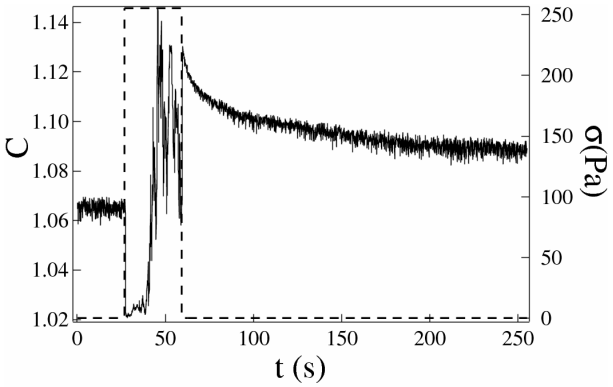

Figure 7.1: *Contrast behavior before, during and after the application of a stress $\sigma = 255$ Pa during 30 s. The stress history is plotted in dashed line. During the stress application, strong contrast fluctuations are observed. After the shear cessation, the contrast exhibits an overshoot and then relaxes to a constant value.*

When the same measurement is repeated under the same conditions, the relaxation curve of the contrast after shear cessation exhibits scarce reproducibility (Fig. 7.2): its amplitude, its noise, the final value and the characteristic relaxation time vary with the measure; while sometimes the overshoot cannot be observed either, as one of the three curves in the figure shows. In

particular, the contrast plateau value after the relaxation varies at each measurement. As the ensemble of measurements presented in Fig. 7.2 are taken with the same sample under the same conditions, it can be considered as a sampling in which a different region of the system after shear cessation is observed during each measurement. The presence of spatial heterogeneities in the system (consisting in slower and faster regions), due to the very high concentration of the suspension, may be responsible for this lack of reproducibility. Indeed, if the length-scale of this heterogeneity is of the order of the illuminated volume size, the non reproducibility of the contrast value at rest may be easily explained: after contrast relaxation, the illuminated region in the various experiments would be characterized by a different local concentration and thus a different dynamical timescale, which induces distinct contrast values.

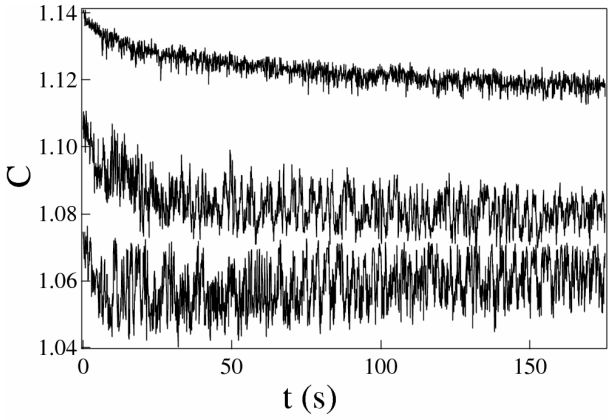

Figure 7.2: *Contrast relaxation, soon after the application of a stress* $\sigma = 180$ *Pa during* 30 *s, for three different measurements performed under the same conditions. The measurements are highly non-reproducible. The overshoot of the contrast is not always observed, as exemplified by the bottom curve. The two other curves exhibit an overshoot, but its amplitude, its characteristic decorrelation time, the value of the baseline and the noise of the contrast signal vary with the measurement.*

Due to the decorrelation effect of the particle drag velocity on the scattered intensity, quantitative results cannot be achieved during the flow. The scarce reproducibility of the contrast relaxation after flow stop and the high

noise of the signal (Fig. 7.2) also prevents us from making systematic measurements after flow stop with an easy quantitative analysis of the results. However, the qualitative evolution of the contrast after shear cessation can be studied as a function of the applied stress. For three different stresses in the jamming regime $\sigma \in \{100, 180, 255\}$, a set of 8 measurements (as the one shown in Fig. 7.1) has been performed under the same conditions. The curves which were not showing an overshoot have been dropped. We used the following criterium : we selected only the curves whose noise was smaller than the half-amplitude of the contrast decrease. The noise is measured as the standard deviation of the contrast when it reaches the final plateau value. For the larger stress value, $\sigma = 255$ Pa, none of the 8 curves had to be dropped, for $\sigma = 180$ Pa, 2 of the set were dropped and 4 for $\sigma = 100$ Pa. In order to compare the relaxation times after the application of different stresses, we averaged the set of the remaining contrast data for each stress value. As the contrast relaxation has an exponential behavior, we applied a logarithmic binning procedure to each averaged curve, in order to reduce noise at long time: firstly, the points of the curve have been averaged in groups of ten, then they are further averaged in order to obtain a curve with 25 points logarithmically spaced on the x-axis. The resulting curves for the contrast relaxation, at the stress value investigated, are plotted in Fig. 7.3. To be better compared, the curves have been normalized between 0 and 1. In order to quantify the relaxation time of these averaged curves, we have chosen a stretched exponential function $C(t) = \exp(-t/\tau)^{\beta}$, which gives a good fit. The value of the τ parameter varies between 4 s for the smaller stress and 29 s for the larger stress. As the value of the β parameter does not remain constant, but varies between 0.5 and 0.7, the average relaxation time $\langle\tau\rangle$ (defined in equation 5.3) is calculated. The values of $\langle\tau\rangle$ are plotted as a function of the stress in the *inset* of Fig. 7.3. For the shear stress here investigated, a higher applied stress thus induces a slower relaxation of the contrast after shear cessation.

7.2 Discussion

We will now attempt an interpretation of the presented results in the light of the reversible cluster formation phenomena (see 2.5), which is believed to be responsible for the shear thickening behavior observed through the mechanical measurements.

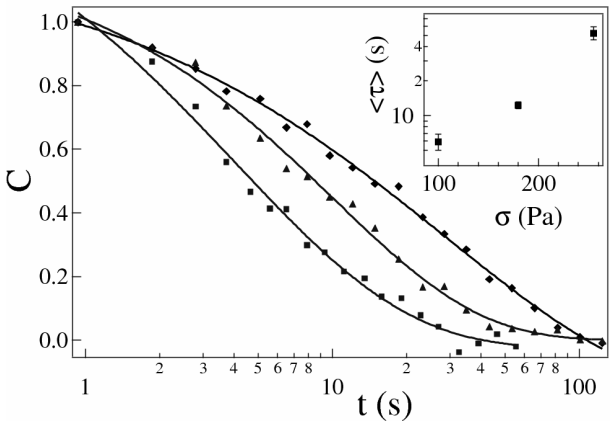

Figure 7.3: *Normalized and averaged contrast relaxation curves after the application of a constant stress σ. Three values of the applied stress are studied: $\sigma = 100$ Pa (■), $\sigma = 180$ Pa (▲) and $\sigma = 255$ Pa (♦). Each curve is fitted with a stretched exponential form. Inset : average relaxation time $\langle\tau\rangle$ as a function of the applied stress.*

A confirmation of cluster formation during the shear is given by the observation of the peaks in the contrast overcoming the contrast value at rest (Fig. 7.1). We interpret these peaks as the presence of groups of particles, passing through the illuminated region, that move slower than in the system at rest. The contrast relaxation after the shear stop proves the reversibility of these forming clusters. As reported in 2.5.2, Ball and Melrose observed in their numerical model that, as the stress increases, percolating clusters of ever decreasing spacing form. As suggested by this result, we may suppose that the slower dynamics revealed during the shear is due to a reduced spacing among the clusters of particles. After the shear stop, the pair distribution function of the particles at rest is restored and the dynamics gets faster, so the contrast relaxes to a smaller value.

The non reproducibility of the relaxing contrast curve for repeated acquisitions (Fig. 7.2) may give us some qualitative information about the cluster size. We want to stress here that, while the relaxation of the contrast after flow stop evidences the formation of shear induced aggregates, the non reproducibility of the contrast value after this relaxation shows that some spatial heterogeneities still remain when the system is at rest, as previously

discussed. The amplitude of the relaxing contrast should dependent on the relative size of the aggregates in the volume of the illuminated region. In some numerical simulations [71], the presence of clusters spanning the all system is said to characterize the jamming regime. The varying amplitude of the relaxing contrast for different acquisitions suggests that the cluster size is comparable to the illuminated region. Unfortunately, a study of the cluster size distribution is not possible, due to the fact that the illuminated region, representing a fraction of the entire cell gap, may contain less than one cluster. Moreover, as sometimes the contrast doesn't show any overshoot after flow cessation, there must be some regions, at least as big as the illuminated volume, without any of the macroscopic clusters responsible for the jamming. This gives us an idea of the average distance among the clusters, which should be of the order of the illuminated region maximum linear size ($\simeq$ 6 mm). Finally, the variation of the characteristic relaxing time of the contrast for different measurements at the same applied stress suggests a varying spacing between the particles of the aggregates that happened to rest in the illuminated volume. From the work of Ball and Melrose indeed, not only clusters of different size, but also clusters with different spacing among the particles are expected to coexist in the system.

From the study of the contrast relaxation at different stresses, we found that for a bigger applied stress, on average, the relaxation time of the aggregates is longer. As also suggested by the work of Ball and Melrose, a bigger stress may thus induce a closer packing between the particles in the cluster, so that it takes longer to restore the normal spacing between them. Finally, the smaller is the stress, the more frequently the contrast overshoot doesn't shows up. This suggests that the density of macroscopic clusters in the system increases with the applied stress. In fact, not only a decrease of the inter-colloidal distance inside aggregates, but also an increase of the aggregate size may be responsible for the observed behavior as the applied stress is increased. Further experiments and direct observation of the colloids organization under shear should allow to choose among these interpretations.

Conclusions

Light scattering techniques have thus allowed us to investigate, from a dynamical point of view, the microscopic behavior characterizing the complex rheology of colloidal systems. For three different phenomenologies, the colloidal particle dynamics have been monitored: shear thinning and shear localization in a glassy suspension and shear thickening in a concentrated suspension of charged particles.

In the shear thinning experiment, shear influenced dynamics have been investigated in an aging Laponite suspension, which represents a model system for glassy colloids. Through dynamic light scattering, we directly probe the particle density correlation function, which is the relevant variable used in the theoretical models for glassy systems. The rejuvenating effect of a steady shear flow on the aging dynamics has been monitored through different protocols. While the system ages under shear, the presence of the flow is observed to strongly affect dynamics as soon as structural relaxation enters the timescale $\dot{\gamma}^{-1}$. In this shear dominated region, the shear rate dependence of the average slow relaxation time $\langle \tau_s \rangle$ is well approximated by the power law $\dot{\gamma}^{-\alpha}$ with $\alpha \sim 1$, which is the typical shear thinning behavior predicted by the theoretical models and observed macroscopically in the viscosity. The effect of shear on the detailed shape of the intermediate scattering function can be well described assuming that the slow relaxation process arises from the heterogeneous superposition of many relaxing units, each one independently coupled to shear rate with a parallel composition rule for timescales: $1/\tau \rightarrow 1/\tau + A\dot{\gamma}$. We than investigated the effect of the flow on the aging dynamics following shear application. If the experiment is performed before the dynamical arrest of the system, full rejuvenation is observed and the phenomenological model previously proposed is consistent with the observed behavior. Once the system has reached the dynamical arrest, a shear flow drives it to a completely different regime, with the system which rapidly ages

back to the arrested phase soon after flow stop.

The shear localization phenomenon have been investigated, through dynamic light scattering, on the same system when low shear rates are applied. An oscillating behavior of the velocity profile has been observed during the shear localization regime, as predicted by some theoretical models. Shear localization induced by the inhomogeneity of the system due to the interaction with metal walls of the cell is also investigated. For a steady profile exhibiting shear localization, the detection of the dynamics in the two bands, during the same experiment, have presented various difficulties and only preliminary results have been reached. We managed to observe an arrested dynamics only when the entire fluid rotates as a solid body and further experiments are needed to detect this behavior in the shear localization regime.

Finally, we investigated through speckle visibility spectroscopy the flow-induced structures forming in a concentrated silica suspension in the jamming regime. The presence of particles moving slower than at rest is evidenced during the flow and the relaxation of the particle dynamics is monitored after flow cessation for various shear stresses. The relaxation time of the shear induced heterogeneities is observed to increase when a higher stress is applied. The results are coherent with the behavior expected in some numerical models, but direct observation of the colloids under shear should allow to better understand the particle organization induced by the flow.

All the quantitative results have been obtained from measurements performed after shear cessation, due to the experimental difficulties in the investigation of the slow dynamics under flow. An effort to overcome these problems may open new perspectives in the investigation of the particle dynamic in the complex rheology of colloidal suspensions. Finally, we want to remark that the whole work have focused on the dynamical aspect of the problem. The particle structure induced by the flow is poorly investigated at the experimental level and may contribute to a more exhaustive comprehension of the microscopic behavior of these systems.

Bibliography

[1] R. G. Larson, *The structure and rheology of complex fluids*, Oxford University Press, New York, (1999).

[2] H. M. Laun, Angew. Makromol. Chem., **123**, 335 (1984).

[3] D. Bonn, S. Tanase, B. Abou, H. Tanaka, and J. Meunier, Phys. Rev. Lett., **89**, 015701 (2002).

[4] G. Petekidis, A. Moussaïd, and P. N. Pusey, Phys. Rev. E **66**, 051402 (2002).

[5] S. Kaloun, M. Skouri, A. Knaebel, J.-P. Münch, P. Hébraud, Phys. Rev. E **72**, 011401 (2005).

[6] V. Viasnoff and F. Lequeux, Phys. Rev. Lett. **89**, 065701 (2002).

[7] F. Ozon, T. Narita, A. Knaebel, G. Debrégeas, P. Hébraud, J.-P. Munch, Phys. Rev. E, **68**, 032401 (2003).

[8] B. Berne and R. Pecora, Dynamic Light Scattering, Wiley, New York (1976).

[9] B.J. Maranzano, N.J. Wagner, J. Rheol. **45**, 1205 (2001); B.J. Maranzano, N.J. Wagner, J. Chem. Phys. **114**, 10514 (2001).

[10] D. Lootens, H. Van Damme, P. Hébraud, Phys. Rev. Lett. **90**, 178301 (2003).

[11] H.M.Laun, R. Bung, S. Hess, W. Loose, O. Hesse, K. Hahn, E. Hadicke, R. Hingmann, F. Schmidt, P. Lindner, J. Rheol. **36**, 743 (1992).

[12] H. Watanabe, M-L. Yao, K. Osaki, T. Shikata, H. Niwa, Y. Morishima, N. P. Balsara, H. Wang, Rheol. Acta **37**, 1 (1998).

[13] V.G. Kolli, E.J. Pollauf, F. Gadala-Maria, J. Rheol. **46**, 321 (2002).

[14] M.D. Haw, Phys. Rev. Lett. **92**, 185506 (2004).

[15] P. Varadan, M.J. Solomon, J. Rheol. **47**, 943 (2003).

[16] D. Lootens, H. van Damme, Y. Hémar, P. Hébraud, Phys. Rev. Lett., **95** 268302 (2005).

[17] P. Coussot, Q. D. Nguyen, H. T. Huynh and D. Bonn, J. Rheol. **46**, 573 (2002); P. Coussot, Q. D. Nguyen, H. T. Huynh and D. Bonn, Phys. Rev. Lett. **88**, 175501 (2002).

[18] P. Coussot, J. S. Raynaud, F. Bertrand, P. Moucheront, J. P. Guilbaud, H. T. Huynh, S. Jarny and D. Lesueur, Phys. Rev. Lett. **88**, 218301 (2002).

[19] F. Pignon, A. Magnin and J.-M. Piau, J. Rheol. **40**, 573 (1996).

[20] D. Bonn, P. Coussot, H. T. Huynh, F. Bertrand, and G. Debrégeas, Europhys. Lett., **59**, 786 (2002); D. Abou, D. Bonn, J. Meunier, J. Rheol. **47**, 979 (2003).

[21] W. M. Holmes, P. T. Callaghan, D. Vlassopoulos and J. Roovers, J. Rheol. **48**, 1085 (2004).

[22] H. L. Hamaker, Physica, **4**, 1058 (1937).

[23] B. Derjaguin and L. Landau, Acta Phys. Chim. URSS, **14**, 633 (1941).

[24] E. J. W. Verwey and J. T. G. Overbeek, Theory of the stability of Lyotropic colloids. Elsevir, Amsterdam (1948).

[25] A. J. Liu and S. R. Nagel, Nature, **396**, 21 (1998).

[26] V. Trappe, V. Prasad, L. Cipelletti, P. N. Segre and D. A. Weitz, Nature **411**, 772 (2001).

[27] P. Sollich, F. Lequeux, P.Hébraud and M. Cates, Phys. Rev. Lett. **78**, 2020 (1997).

[28] P. Sollich, Phys. Rev. E **58**, 738 (1998).

[29] P. Hébraud and F. Lequeux, Phys. Rev. Lett. **81**, 2934 (1998).

[30] J. Kurchan, cond-mat/0011110 (2000).

[31] B. Derrida, Phys. Rev. Lett. 45, **79** (1980).

[32] J.-P. Bouchaud, J. Phys. France I **2**, 1705 (1992).

[33] D. A. Head, A. Ajdari and M. E. Cates, Phys. Rev. E **64**, 061509 (2001).

[34] D. A. Head, A. Ajdari and M. E. Cates, Europhys. Lett. **57**, 120 (2002).

[35] W.Götze, in *Liquids, freezing and the glass transition*; J.-P.Hansen, D.Levesque, J.Zinn-Justin, NATO-ASI, Les-Houches Series; W.Götze, J. Phys. Condensed Matter **11**, A1 (1999).

[36] M. Fuchs and M. E. Cates, Faraday Discuss., **123**, 267(2003).

[37] J. Bergenholtz, Curr. Opin. Colloids Interface Sci. **6**, 484 (2001).

[38] L. Berthier, J.-L. Barrat, J. Kurchan, Phys. Rev. E **61**, 5464 (2000).

[39] L. Berthier J. Phys.: Condens. Matter **15**, 933 (2003).

[40] M. Fuchs, M. E. Cates, Phys. Rev. Lett. **89**, 24 (2002).

[41] K. Miyazaki, D. R. Reichman, Phys. Rev. E **66**, 050501 (2002).

[42] A. Onuki, K. Kawasaki, Ann. Phys. (N. Y.) **121**, 456 (1979).

[43] L. F. Cugliandolo, J. Kurchan, Phys. Rev. Lett. **71**, 173 (1993).

[44] E. Bertrand, J. Bibette and V. Schmitt, Phys. Rev. E **66**, 60401 (2002).

[45] C. B. Holmes, M. Fuchs and M. E. Cates, Europhys. Lett. **63**, 240 (2003).

[46] J.-P. Hansen, I. R. McDonald, *Theory of simple liquids*, Academic Press (1990).

[47] C. Derec, A. Ajdari and F. Lequeux, Eur. Phys. J. E **4**, 355 (2001).

[48] A. Ajdari, seminar for the School in Les Houches, printed by EDP Science, Springer-Verlag (1999).

[49] M. E. Cates, seminar for the School in Les Houches, printed by EDP Science, Springer-Verlag (2003).

[50] G. Picard, A. Ajdari, L. Bocquet and F. Lequeux, Phys. Rev. E **66**, 051501 (2002).

[51] L. Bocquet and J.-L. Barrat, Phys. Rev. E **49**, 3079 (1994).

[52] R. Yamamoto, A. Onuki, Phys. Rev. E **58**, 3515 (1998).

[53] J.-L. Barrat, L. Berthier, Phys. Rev. E **63**, 012503 (2000).

[54] L. Berthier, J.-L. Barrat, Phys. Rev. Lett. **89**, 095702 (2002).

[55] L. Berthier, J.-L. Barrat, J. Chem. Phys. **116**, 6228 (2002).

[56] F. Varnik, L. Bocquet, J.-L. Barrat and L. Berthier, Phys. Rev. Lett. **90**, 095702 (2003).

[57] F. Varnik, L. Bocquet and J.-L. Barrat, J. Chem. Phys. **120**, 2788 (2004).

[58] G. Porte, J.-F. Berret and J. L. Harden, J. Phys. II France **7**, 459 (1997).

[59] N. A. Spenley, X. F. Yuan and M. E. Cates, J. Phys. II France **6**, 551 (1996).

[60] P. D. Olmsted, C.-Y. D. Lu, Phys. Rev. E **56**, 55 (1997).

[61] C.-Y. D. Lu, P. D. Olmsted and R. C. Ball, Phys. Rev. Lett. **84**, 642 (2000).

[62] J. K. G. Dhont, Phys. Rev. E **60**, 4534 (1999).

[63] R. L. Hoffman, Trans. Soc. Rheol. **16**, 155 (1972), R. L. Hoffman, J. Colloid Interface Sci. **46**, 491 (1974).

[64] R. L. Hoffman, J. Rheol. **42**, 111 (1998).

[65] G. Berthier and J. F. Brady, J. Chem. Phys. **91**, 1866 (1989).

[66] D. R. Foss and J. F. Brady, J. Fluid Mech. **407**, 167 (2000).

[67] J. Bergenholtz, J. F. Brady and M. Vivic, J. Fluid Mech. **456**, 239 (2002).

[68] J. F. Brady and J. F. Morris, J. Fluid Mech. **348**, 103 (1997).

[69] R.C. Ball, J.R. Melrose, Adv. Colloid Interface Sci. **59**, 19 (1995).

[70] M. E. Cates, J. P. Wittmer, J.-P. Bouchaud and P. Claudin, Phys. Rev. Lett. **81**, 1841 (1998).

[71] O.J. O'Loan, M.R. Evans, M.E. Cates, Physica A **258**, 109 (1998).

[72] R. S. Farr, J. R. Melrose, R.C. Ball, Phys. Rev. E **55**, 7203 (1997).

[73] J. Bender, N. J. Wagner, J. Rheol. **40**, 899 (1996).

[74] J. R. Melrose, J. H. van Vliet and R.C. Ball, Phys. Rev. Lett. **77**, 4660 (1996).

[75] Contribution by P. N. Pusey in *Scattering Methods Applied to Soft Condensed Matter*, edited by P. Lindner, Th. Zemb, North Holland (2002).

[76] C. S. Johnson, Jr. and Don A. Gabriel, *Laser Light Scattering*, Dover (1994).

[77] X.L. Wu, D.L. Pine, P.M. Chaikin, J.S. Huang, D.A. Weitz, J. Opt. Soc. Am. B **7**, 15 (1990).

[78] J. Ricka, Applied Optics 32, 2860 (1993)

[79] J.-B. Salmon, S. Manneville, A. Colin, and B. Pouligny, Eur. Phys. J. AP **22**, 143 (2003).

[80] R. Di Leonardo, F. Ianni, G. Ruocco, J. Fluid Mech. **525**, 27 (2005).

[81] A. Onuki, K. Kawasaki, Ann. Phys. **121**, 456 (1979).

[82] B. J. Ackerson, N. A. Clark, J. Phys. **42**, 929 (1981).

[83] R. Perkins, R. Brace, and E. Matijević, J. Colloid Interface Sci. **74**, 509 (1974).

[84] E. Balnois, S. Durand-Vidal, and P. Levitz, Langmuir **19**, 6633 (2003).

[85] J.P. Hansen, and H. Löwen, Annu. Rev. Phys. Chem. **51**, 209 (2000).

[86] Web site *www.lapotite.com*

[87] M. Dijkstra, J.-P. Hansen, P. A. Madden, Phys. Rev. Lett. **75**, 2236 (1995); M.Dijkstra, J.-P. Hansen, P.A.Madden, Phys. Rev. E **55**, 3044 (1997).

[88] S. Mossa, C. De Michele, F. Sciortino, cond-mat/0607516 (2006).

[89] A. Mourchid and P. Levitz, Phys. Rev. E, **57**, 4887 (1998).

[90] T. Nicolai, S. Cocard, Langmuir, **16**, 8189 (2000).

[91] M. Kroon, G. H. Wegdam, and R. Sprik, Phys. Rev. E, **54**, 6541 (1996).

[92] B. Abou, D. Bonn, and J. Meunier, Phys. Rev. E, **64**, 021510 (2001).

[93] B. Ruzicka, L. Zulian, G. Ruocco, Phys. Rev. Lett., **93**, 258301 (2004); B. Ruzicka, L. Zulian, G. Ruocco, Langmuir, **22**, 1106 (2006).

[94] D. Bonn, H. Kellay, H. Tanaka, G. Wegdam, J. Meunier, Langmuir, **15**, 7534 (1999).

[95] D. Bonn, H. Tanaka, G. Wegdam, H. Kellay, J. Meunier, J. Europhys. Lett., **45**, 52 (1999).

[96] M. Bellour, A. Knaebel, J. L. Harden, F. Lequeux, J.-P. Münch, Phys. Rev. E, **67**, 031405 (2003).

[97] S. Kaloun, R. Skouri, M. Skouri, J.-P. Münch, F. Schosseler, Phys. Rev. E **72**, 011403 (2005).

[98] F. Zamponi, degree thesis, Università La Sapienza di Roma (2001).

[99] The PhotonLab package is available for download at: http://glass.phys.uniroma1.it/dileonardo/photonlab.html.

[100] F. Ianni, degree thesis, Università La Sapienza di Roma (2003).

[101] J. Ricka, Applied Optics **32**, 2860 (1993).

[102] B. E. A. Saleh, M.C. Teich, *Fundamentals of Photonics*, Wiley Interscience (1991).

[103] M. E. Fagan, C. F. Zukoski, J. Rheol. **41**, 373 (1997).

[104] D. Lootens, H. Van Damme, P. Hebraud, Phys. Rev. Lett. **90**, 178301 (2003).

[105] W. Stöber and A. Fink, J. Colloid Interface Science. **26**, 62 (1968).

[106] D. Lootens, PhD thesis, Université Paris VI (2004).

[107] R.K. Iler, The Chemistry of Silica, John Wiley (1979).

[108] D. Lasne, DEA Stage, Ecole Supériore de Physique et Chimie Industrielles (2004).

[109] L. Cipelletti, H. Bissig, V. Trappe, P. Ballesta, S. Mazoyer, J. Phys.: Condens. Matter **15**, S257 (2003).

[110] P.K. Dixon, D.J. Durian, Phys. Rev. Lett. **90**, 184302 (2003).

[111] R. Bandyopadhyay, A.S. Gittings, S.S. Suh, P.K. Dixon, D.J. Durian, Rev. Sci. Instrum **76**, 093110 (2005).

[112] L. Zulian, B. Ruzicka, G. Ruocco, S. Capaccioli, J. non-Cryst. Solids, to be published.

[113] K. L. Ngai, Adv. Colloid Interface Sci. **64**, 1 (1996).

[114] R. Richert, J. Phys.: Condens. Matter **14**, R703 (2002).

[115] L. Cipelletti, S. Manley, R. C. Ball and D. A. Weitz, Phys. Rev. Lett. **84**, 2275 (2000).

[116] J.-P. Bouchaud and E. Pitard, Eur. Phys. J. E. **6**, 231 (2001).

[117] We thank Luca De Lorenzo, who has performed these rheological measurements.

[118] F. Pignon, A. Magnin, J.-M. Piau, B. Cabane, P. Lindner, and O. Diat Phys. Rev. E **56**, 3281 (1997).

[119] S. Butler and P. Harrowell, Nature **415**, 1008 (2002).

[120] A. Ajdari, Phys. Rev. E **58**, 6294 (1998).

List of publications

Francesca Ianni, Roberto Di Leonardo, Silvia Gentilini, Giancarlo Ruocco. *Aging after shear rejuvenation in a soft glassy colloidal suspension: evidence for two different regimes.* Phys. Rev. E **75**, 011408 (2007).

Francesca Ianni, David Lasne, Régis Sarcia, Pascal Hébraud. *Relaxation of jammed colloidal suspensions after shear cessation.* Phys. Rev. E **74**, 011401 (2006).

Roberto Di Leonardo, Francesca Ianni, Giancarlo Ruocco. *Aging under shear: Structural relaxation of a non-Newtonian fluid.* Phys. Rev. E **71**, 011505 (2005).

Roberto Di Leonardo, Silvia Gentilini, Francesca Ianni, Giancarlo Ruocco. *Aging and Flow in a Complex Fluid.* Proceeding from the 5th International Discussion Meeting on Relaxations in Complex Systems, to be published in J. Non-Cryst. Sol.

Summary

The aim of this experimental work is to characterize, through light scattering techniques, the dynamics of some colloidal systems exhibiting a complex rheological behaviour. The thesis is developed around two topics: rejuvenation and shear banding in a glassy colloidal system, and the jamming phenomenon in a concentrated suspension of charged particles. In a Laponite suspension -a model system for glassy colloidal systems- the competition between shear rejuvenation and aging have been investigated during the flow, while two regimes of aging have been evidenced after flow cessation. Shear localization have been observed at low shear rates by monitoring the velocity profiles and a stick-slip behaviour has been evidenced by the oscillations of the banded velocity profile. In a concentrated suspension of silica particles in the jamming regime, we have investigated the dynamics of flow-induced structures. The presence of particles moving slower than at rest has been evidenced during the flow and the relaxation of the particle dynamics has been studied after flow cessation as a function of the applied shear stress.

Resumé

Ce travail expérimental cherche à mieux caractériser, au moyen des techniques de diffusion de la lumière, la dynamique de certains systèmes colloïdaux qui montrent un comportement rhéologique complexe. Il s'articule autour de deux points: le rajeunissement et la formation des bandes de cisaillement dans un système colloïdal vitreux, et le phenomène du jamming dans une suspension concentrée de particules chargées. Dans une suspension de Laponite -système modèle pour les colloïdes vitreux- la compétition entre le rajeunissement dû au cisaillement et le vieillissement a été étudié pendant l'écoulement, alors qu'aprés l'arret de l'écoulement deux régimes de vieillissement ont été observés. La localisation du cisaillement a été mis en evidence à des taux faibles de cisaillement global, en mesurant les profils de vitesse du fluide, mesure qui en outre, par ses oscillations, a révélé un comportement de stick-slip. D'autre part dans une suspension concentrée de particules de silice dans le régime de jamming, nous nous sommes interessés à la dynamique des structures induites par l'écoulement et avons mis en évidence la présence de particules plus lentes pendant le cisaillement, puis avons étudiés la relaxation de la dynamique des particules après l'arret de l'écoulement en fonction des contraintes appliquées.